

Air Force Institute of Technology

AFIT Scholar

Theses and Dissertations

Student Graduate Works

3-2020

Validation of HTS Optical Turbulence Profiling via Sonic Anemometry

Alexander S. Boeckenstedt

Follow this and additional works at: <https://scholar.afit.edu/etd>



Part of the [Optics Commons](#)

Recommended Citation

Boeckenstedt, Alexander S., "Validation of HTS Optical Turbulence Profiling via Sonic Anemometry" (2020). *Theses and Dissertations*. 3886.
<https://scholar.afit.edu/etd/3886>

This Thesis is brought to you for free and open access by the Student Graduate Works at AFIT Scholar. It has been accepted for inclusion in Theses and Dissertations by an authorized administrator of AFIT Scholar. For more information, please contact AFIT.ENWL.Repository@us.af.mil.



**Validation of HTS Optical Turbulence Profiling
via Sonic Anemometry**

THESIS

Alexander S. Boeckstedt, 2d Lt, USAF
AFIT-ENP-MS-20-M-082

**DEPARTMENT OF THE AIR FORCE
AIR UNIVERSITY**

AIR FORCE INSTITUTE OF TECHNOLOGY

Wright-Patterson Air Force Base, Ohio

DISTRIBUTION STATEMENT A
APPROVED FOR PUBLIC RELEASE; DISTRIBUTION UNLIMITED.

The views expressed in this document are those of the author and do not reflect the official policy or position of the United States Air Force, the United States Department of Defense or the United States Government. This material is declared a work of the U.S. Government and is not subject to copyright protection in the United States.

AFIT-ENP-MS-20-M-082

VALIDATION OF HTS OPTICAL TURBULENCE PROFILING VIA SONIC
ANEMOMETRY

THESIS

Presented to the Faculty
Department of Engineering Physics
Graduate School of Engineering and Management
Air Force Institute of Technology
Air University
Air Education and Training Command
in Partial Fulfillment of the Requirements for the
Degree of Master of Science in Applied Physics

Alexander S. Boeckensdt, B.S. Physics
2d Lt, USAF

26 March 2020

DISTRIBUTION STATEMENT A
APPROVED FOR PUBLIC RELEASE; DISTRIBUTION UNLIMITED.

AFIT-ENP-MS-20-M-082

VALIDATION OF HTS OPTICAL TURBULENCE PROFILING VIA SONIC
ANEMOMETRY

THESIS

Alexander S. Boeckenedt, B.S. Physics
2d Lt, USAF

Committee Membership:

Dr. J. E. McCrae
Chairman

Dr. S. R. Bose-Pillai
Member

Dr. S. T. Fiorino
Member

Abstract

Previous turbulence measurements along a near-ground, 500 m, horizontal path using two helium-neon laser beacons and a Hartmann Turbulence Sensor (HTS) yielded profiles of C_n^2 by estimating turbulence parameters such as Fried’s coherence length, inner scale, and Greenwood frequency by measuring local aberrated wavefront tilts. The HTS C_n^2 estimates were consistent with integrated turbulence values collected along the same path by a BLS900 scintillometer. Further validation of the HTS profiling method is necessary to produce accurate optical turbulence profiles for wavefront correction and to eventually gain an improved understanding of turbulence in the lower atmosphere and its variation as a function of altitude. In order to add confidence to the HTS dual-beacon profiling method, a collection of sonic anemometers was added along the path to collect point measurements of C_T^2 , which were used to derive values of C_n^2 . Comparison of the independently measured data sets helps legitimize the HTS turbulence profiling method. Propagation over a non-homogeneous path (i.e. part grass and part concrete) ensured the turbulence profile along the path is more varied. C_n^2 profiles in this work derived from HTS data captured on 25 and 26 July 2019 agreed strongly with the collocated anemometer and BLS measurements.

Acknowledgements

I would like to thank my advisor, Dr. McCrae, for his guidance over the course of this thesis and for his time spent on the runway helping collect data, along with setting up and tearing down equipment.

Thank you to Dr. Bose-Pillai for her assistance during the data collection and processing of this work and for contributing numerous resources as well as hours of helpful discussion. I would also like to thank both Dr. McCrae and Dr. Bose-Pillai for laying the foundations that made this work possible.

Thank you to Dr. Rice for his help when setting up the trailers and anemometers on the runway and for supplying us with much-needed equipment over the course of the experiment.

Thank you to Dr. Keefer for providing multiple scripts and resources for anemometer operation and for giving additional weather data.

Many thanks to Ben Wilson for his hard work and expertise on the anemometers, along with the countless hours of labor when setting up and maintaining the experiment and assisting with data collection.

Lastly, thank you to my wife for her support and motivation.

Alexander S. Boeckenstedt

Table of Contents

	Page
Abstract	iv
Acknowledgements	v
List of Figures	vii
List of Tables	ix
I. Introduction	1
1.1 Motivation	1
1.2 Objective	2
1.3 Organizational Structure	3
II. Background	4
2.1 Electromagnetic Wave Propagation	4
2.2 Atmospheric Turbulence	7
2.3 Statistical Model of the Atmosphere	13
2.4 Kolmogorov Theory	15
2.5 Methods of Turbulence Profiling	18
2.6 Adaptive Optics	23
2.7 Multi-Conjugate Adaptive Optics	26
III. Experiment	29
3.1 Theory	29
Weighting Functions	29
Constrained Nonlinear Optimization	40
3.2 Equipment	40
Hartmann Turbulence Sensor (HTS)	40
Sonic Anemometers	45
Boundary Layer Scintillometer (BLS)	48
3.3 Methodology	53
IV. Results	59
4.1 Profiles Affected by Cloud Coverage	72
4.2 Fried Parameter Estimates	74
V. Conclusion	76
Appendix A. Anemometer Structure Function Averaging Issues	96
Bibliography	98

List of Figures

Figure		Page
1	Kolmogorov energy cascade theory of turbulence	9
2	Planar wavefront distortion due to the atmosphere	10
3	SLODAR geometry	22
4	Adaptive optics imaging system diagram	24
5	Multi-conjugate adaptive optics system	28
6	SLODAR subaperture pair and source pair geometry	30
7	Plot of crossing path weighting functions over the 511 m range	35
8	Non-crossing weighting function source and aperture geometry	36
9	Plot of non-crossing weighting functions	37
10	Influence function with pseudoinverse threshold of 11	39
11	Influence function with pseudoinverse threshold of 31	39
12	Shack-Hartmann wavefront sensor diagram	41
13	Altered subaperture mask	42
14	Local wavefront tilt's effect on centroid location	43
15	Layout of HTS optics	43
16	SATI/3A ultrasonic anemometer design	45
17	Anemometer-measured C_n^2 plots for 25 and 26 July	47
18	Net radiometer cloud coverage plots for 25/26 July	49
19	BLS center-weighted path weighting function	50
20	BLS C_n^2 readings from 25/26 July	52
21	Overhead map of experiment path	53

Figure		Page
22	HTS raw data compared to processed data	56
23	Final combination of weighting functions for data processing	58
24	25 July 2200 C_n^2 profile	60
25	25 July 2218 C_n^2 profile	61
26	25 July 2232 C_n^2 profile	62
27	25 July 2247 C_n^2 profile	63
28	25 July 2305 C_n^2 profile	64
29	25 July 2320 C_n^2 profile	65
30	25 July 2348 C_n^2 profile	66
31	25 July 0024 C_n^2 profile	67
32	25 July 0047 C_n^2 profile	68
33	25 July 0133 C_n^2 profile	69
34	26 July 2049 C_n^2 profile	70
35	26 July 2134 C_n^2 profile	71
36	26 July 2120 C_n^2 profile	72
37	26 July 2128 C_n^2 profile	73

List of Tables

Table		Page
1	HTS optics bench specifications.....	44
2	Estimated vertical and horizontal components of r_0	74

VALIDATION OF HTS OPTICAL TURBULENCE PROFILING VIA SONIC ANEMOMETRY

I. Introduction

Any field relying on atmospheric propagation, whether it be long-range imaging or laser operation, must take into account the detrimental effects of optical turbulence. Knowledge of key turbulence parameters, such as the Fried coherence length, r_0 , the refractive index structure parameter, C_n^2 , and the Greenwood frequency, f_G is necessary to model the turbulence along a path. The Hartmann Turbulence Sensor (HTS) was designed by the Optical Science Company (tOSC) as a tool to provide time efficient and reliable estimates of these statistical parameters [1]. A novel method of turbulence profiling using an HTS system is discussed in this thesis.

1.1 Motivation

For decades, researchers have attempted to produce models of optical turbulence in the surface layer of the atmosphere (<100 m), where its effects on wavefront propagation are most prominent [2]. Negative impacts of atmospheric turbulence include laser wavefront degradation and an increase in transmission bit error rates in communication systems. The task of modeling and profiling turbulence has proven difficult due to the chaotic nature of turbulence and lack of proper measurements. Methods using scintillometry are effective to estimate statistical parameters of the turbulence along a path. However, scintillometers are easily saturable over long paths and therefore have limited operational range [3]. Adaptive optics (AO) systems have demonstrated their effectiveness in compensating for the optical turbulence through use of

a deformable mirror, but under highly anisoplanatic conditions, compensation with a single mirror is inadequate and additional information on the turbulence profile must be gathered for effective compensation. If the full turbulence profile is known, multiple deformable mirrors can be operated to correct the phase distortions [4]. In the past, these profiles have been found using techniques like Scintillation Detection and Ranging (SCIDAR), which suffers from similar saturation problems as scintillometers, and Slope Detection and Ranging (SLODAR) [5, 6, 7, 8, 9]. These techniques are restricted by their need for large apertures and data processing requirements. The present technique of HTS operation uses SLODAR-like measurements. However, the methodology to derive the profiles is much different. The HTS uses a phase-based technique rather than irradiance-based and hence does not suffer from saturation issues. HTS operation also benefits from a very high-speed camera that is capable of collecting extensive sample sizes in short periods of time for reliable estimation of turbulence parameters. This makes the HTS an ideal candidate to feed information into AO systems, which require accurate real-time knowledge of turbulent parameters in order for their closed-loop feedback mechanisms to function properly. A new method of HTS operation developed at the Air Force Institute of Technology (AFIT) Center for Directed Energy (CDE) is outlined and presented as a potential solution to the problems outlined above.

1.2 Objective

Previous work [2] has proven that HTS operation with two source beacons is an effective method of profiling turbulence by comparison with a commercial scintillometer along the same horizontal path. The scintillometer provides single, center-weighted, integrated C_n^2 values. Therefore, the comparison was made to the center-path measurements of the HTS profile. The purpose of this thesis is to further validate this

two-beacon profiling method by comparison with a scintillometer and with sonic anemometers collocated along the path. This work will eventually help in obtaining a greater understanding of surface-layer optical turbulence. The final product from this work will be C_n^2 profiles and r_0 estimates under varying turbulent conditions including time of day, cloud coverage, and wind velocity. The C_n^2 profiles will be optimized and compared with the C_n^2 estimates produced by a boundary-layer scintillometer and with the C_n^2 point measurements derived from anemometer data. The wavefront tilts found from HTS measurements could later be passed through an AO system to correct for the turbulence-induced phase distortions in real time. The inhomogeneous profiling path chosen for this work includes sections of grass and sections of concrete, which will provide more information on how these parameters affect local turbulence strength.

1.3 Organizational Structure

Chapter 2 of this thesis provides a literature review of the past work in the field of optical turbulence and the methods of estimating turbulence parameters as well as the applications of this work. It lays the theoretical foundation supporting this work. Chapter 3 is a summary of the operating equipment, the experimental methodology, and the theory used to generate and optimize the profiles. Chapter 4 presents the results and their significance. Lastly, chapter 5 discusses the results in terms of the goal of this thesis and provides possible routes for future work on the subject.

II. Background

The purpose of this chapter is to provide the foundational level of knowledge needed to reproduce this thesis by summarizing the literature. Electromagnetic wave propagation is discussed along with its connection to first principles. Then, optical turbulence in the atmosphere and the Kolmogorov theory are summarized along with any underlying assumptions. Previous methods of measuring turbulence parameters such as slope detection and ranging (SLODAR) and scintillation detection and ranging (SCIDAR) are also outlined as well as their connection with this work and the goal of this thesis. Finally, adaptive optics is introduced as an applicable method of correcting for turbulence distortion.

2.1 Electromagnetic Wave Propagation

In order to understand how light propagates through a turbulent atmosphere, one must understand how light propagates through a still atmosphere. Under the standard assumptions that the atmosphere is a linear, inhomogeneous, isotropic medium, Maxwell's equations, which describe the electric and magnetic fields, \mathbf{E} and \mathbf{H} respectively, of an electromagnetic wave are written

$$-\nabla \times \mathbf{E} = \frac{\partial}{\partial t}(\mu\mathbf{H}) \quad (1)$$

$$\nabla \times \mathbf{H} - \sigma\mathbf{E} = \frac{\partial}{\partial t}(\epsilon\mathbf{E}) \quad (2)$$

$$\nabla \cdot (\epsilon\mathbf{E}) = \rho \quad (3)$$

$$\nabla \cdot (\mu\mathbf{H}) = 0. \quad (4)$$

The permittivity ϵ , the permeability μ , the charge density ρ , and the conductivity σ are all electromagnetic properties of the medium [10]. ϵ_0 and μ_0 denote the permittivity and permeability in free space. In the atmosphere, each of these properties fluctuate temporally and spatially and hence the fields \mathbf{E} and \mathbf{H} can be written as

$$\mathbf{E}(\mathbf{r}, t) = e^{-i\omega t} \mathbf{E}(\mathbf{r}) \quad (5)$$

$$\mathbf{H}(\mathbf{r}, t) = e^{-i\omega t} \mathbf{H}(\mathbf{r}), \quad (6)$$

where $\omega = 2\pi\nu$ is the angular frequency and $i = \sqrt{-1}$ is the imaginary number. Substituting (2) and the curl of (1) into the vector identity

$$\nabla \times (\nabla \times \mathbf{A}) = \nabla(\nabla \cdot \mathbf{A}) - \nabla^2 \mathbf{A} \quad (7)$$

along with some further simplifications and assumptions outlined in detail by Mahalov et al. [10], results in the vector Helmholtz equation

$$\nabla^2 \mathbf{E}(\mathbf{r}) + k_0^2 n^2(\mathbf{r}) \mathbf{E}(\mathbf{r}) = 0. \quad (8)$$

$k_0^2 = \omega^2 \mu_0 \epsilon_0$ is the wavenumber and n is the refractive index, which physically represents how fast light will travel through the medium at location \mathbf{r} . ∇^2 is the Laplacian operator defined by

$$\nabla^2 \equiv \frac{\partial^2}{\partial x^2} + \frac{\partial^2}{\partial y^2} + \frac{\partial^2}{\partial z^2}. \quad (9)$$

The solutions to (8) satisfy the scalar form of the Helmholtz equation

$$\nabla^2 u + k_0^2 n^2(\mathbf{r}) u = 0, \quad (10)$$

which itself has solutions of the form

$$u(\mathbf{r}) = A(\mathbf{r})e^{ik_0\phi(\mathbf{r})}, \quad (11)$$

where A is the amplitude at location \mathbf{r} and ϕ is the phase at \mathbf{r} .

The Helmholtz equation results from a derivation of the wave equation when looking specifically at the complex component of the wave and is therefore useful in more elaborate situations [11]. In a more general sense, propagating waves are solutions to the three-dimensional differential wave equation

$$\nabla^2 u = \frac{1}{v^2} \frac{\partial^2 u}{\partial t^2}, \quad (12)$$

where $v = \omega/k$ is the wave's propagation velocity. Light waves emerging from a point source are described as spherical because of their rounded wavefronts. Spherical waves are described mathematically by

$$u(\mathbf{r}, t) = \frac{A}{r} e^{i(kr \mp \omega t)}, \quad (13)$$

where A is known as the source strength, or the wave's amplitude at the source, r is the propagation distance and $k = 2\pi/\lambda$ is the wavenumber. A/r is the wave's amplitude, which degrades as the wave propagates and spreads. After propagation over long distances, such as the case when observing distant stars, the curvature of the wavefront becomes negligible and they can be estimated as planar, or flat, as represented by

$$u(\mathbf{r}, t) = A e^{i(\mathbf{k} \cdot \mathbf{r} \mp \omega t)}, \quad (14)$$

Where A is now a constant amplitude that doesn't change as a function of propagation distance. Each of these equations are solutions to the wave equation [11].

Once effects such as diffraction are introduced, it becomes difficult to describe mathematically how light will react. Huygens' principle, which is a direct result from the differential wave equation, attempts to simplify this complexity by assuming each point across a wavefront is itself a source of a spherical wavelet that exhibits the same velocity and frequency as its predecessor [11]. Huygens' principle is a greatly simplified theory of wave propagation that does not account for interference effects. More complicated phenomena such as propagation through turbulence must be described using different methods.

2.2 Atmospheric Turbulence

The collection of molecules in the atmosphere move as a mostly inviscid fluid with two evident states of motion: laminar flow and turbulent flow. Laminar flow is smooth and uniform such that mixing within the velocity field does not occur, whereas turbulent flow is random, chaotic, and leads to a nonuniform velocity field, which diffracts propagating light waves unevenly across their wavefronts [12]. To categorize the fluid motion, Osborne Reynolds [13] introduced a dimensionless quantity

$$Re = \frac{Vl}{\nu} \quad (15)$$

known as the Reynold's number, where V is a characteristic velocity, l is a characteristic length, and ν is the kinematic viscosity ($\frac{m^2}{s}$). The similarity principle for incompressible flow states that for a given set of boundaries, the Reynold's number is the only control parameter [14]. The transition from laminar to turbulent flow occurs at a point known as the critical Reynold's number [12]. The kinematic viscosity of air is $\nu = 1.5 \times 10^{-5} \frac{m^2}{s}$. If a scale size of $l = 10$ m and a velocity of $V = 1 \frac{m}{s}$ are assumed, a Reynold's number of $Re = 6.7 \times 10^5$ is obtained [15]. This value is greater

than the critical Reynold's number and is therefore high enough to ensure the air flow in the atmospheric is almost always turbulent. Once in the turbulence regime, the turbulent motion is dominated by inertial forces, which produce flow instabilities and chaotic eddies. However, at very high Reynold's numbers, statistical symmetries seem to reappear. Turbulence under these conditions is known as fully developed turbulence.

By nature, the fluid motion of the atmosphere is turbulent. Temperature, pressure, and humidity fluctuations lead to pockets of unstable air currents known as optical turbules, or more colloquially, eddies. The effects of pressure and humidity are often considered negligible and therefore turbulence is seen as a function of only temperature fluctuations [16]. Temperature variations on the scale of less than 1°C produce small fluctuations in atmospheric density, and subsequently, in the index of refraction. The slight variations in refractive index can accumulate on a light beam and lead to major inhomogeneities, which in turn cause detrimental effects like beam wander, scintillation, and beam spreading [4]. Eddies form at the macroscale when energy sources such as wind shear and convection increase the wind velocity, which in turn increases the Reynold's number of the turbulent flow until it passes the critical Reynold's number. Kolmogorov's energy cascade theory of turbulence adopted from Richardson [17] shown in Figure 1 states that large scale eddies transfer their energy to the continuum of smaller scale eddies. The outer scale of eddy size, denoted by L_0 , is the upper bound below which the turbulent flow of eddies is independent of the parent flow. The inner scale, l_0 , is the lower bound below which the energy cascade ceases and the energy contained by the eddies is instead dissipated in the form of heat. The inner scale is related to the dissipation rate of turbulent kinetic energy, ϵ ,

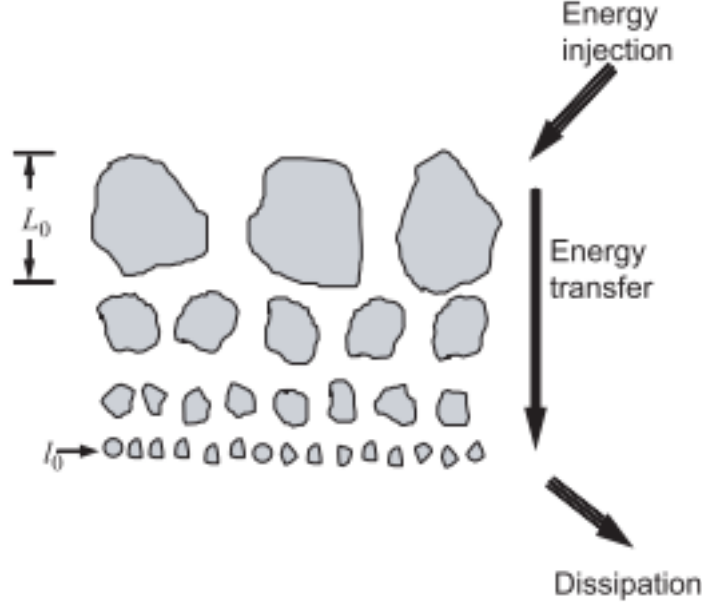


Figure 1. Kolmogorov energy cascade theory of turbulence, where eddies at the outer scale, L_0 , transfer kinetic energy to the continuum of eddies towards the inner scale, l_0 . Eddies smaller than the inner scale dissipate their energy as heat [12].

and the kinematic viscosity, ν , by [4]

$$l_0 = 7.4 \left(\frac{\nu^3}{\epsilon} \right)^{1/4}. \quad (16)$$

Eddies larger than l_0 and smaller than L_0 form the inertial subrange. From ground level to approximately 100 m above ground, the outer scale is assumed to grow linearly as a function of height [12].

The atmospheric index of refraction is particularly sensitive to temperature fluctuations and turbulent mixing. The effect on refractive index is powerful enough that it becomes spatially and temporally random. These variations in refractive index, which perform as lenses in beam propagation, are the driving factor behind optical turbulence [7]. A light beam passing through a turbulent medium experiences inhomogeneous phase distortion across its wavefront because patches across the wavefront propagate at a slightly different velocity based on the varying refractive indices they

encounter. With longer exposures (i.e. longer propagation distances), more phase distortion is accumulated on the wavefront. This phenomenon causes optical turbulence to behave as a low-pass spatial filter, which softens sharp edges and causes point sources to appear as blurs [18]. The effects of optical turbulence on an incident planar wavefront are shown in Figure 2.

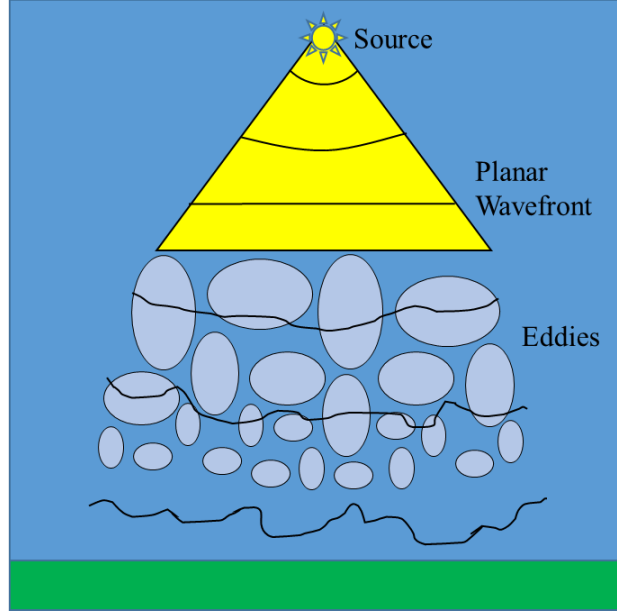


Figure 2. Atmospheric distortion of a planar wavefront due to optical turbulence. As the wavefront contacts eddies, points across the wavefront propagate at varying velocities based on the indices of refraction they pass through, which in turn distorts the wavefront.

One of the most significant parameters of optical turbulence strength, known as the Fried coherence length denoted by r_0 , was introduced by David Fried in 1967 [19]. The Fried parameter physically represents the diameter of a circular patch of wavefront over which the root-mean-square aberration due to turbulence is equal to 1 radian. For telescopes without AO and with apertures larger than r_0 , imaging resolution will be limited by turbulence and thus diffraction-limited performance is not achievable. In adaptive optics design, r_0 is used to determine the spacing of deformable mirror actuators [20]. The Fried coherence length is described mathemat-

ically for a plane wave as

$$r_0 = \left[0.423k^2 \sec(\beta) \int_{Path} C_n^2(z) dz \right]^{-3/5}, \quad (17)$$

where k is the wavenumber, z is the height from ground [12], and β is the zenith angle (i.e. the angle of observation relative to surface normal) [21]. For the purpose of this work, which assumes spherical waves from the HeNe point sources, r_0 is given by

$$r_0 = \left[0.423k^2 \int_{Path} C_n^2(z) \left(1 - \frac{z}{L}\right)^{5/3} dz \right]^{-3/5}, \quad (18)$$

where $L = 511$ m is the path length, β is assumed to be 0, and z is now position along a horizontal path ($z = 0$ at the aperture plane). This integral can be discretized as

$$r_0^{-5/3} = 0.423k^2 \sum_{i=0}^L C_{ni}^2 \left(1 - \frac{z_i}{L}\right)^{5/3} \Delta z, \quad (19)$$

where Δz is the step size, which has been chosen in this experiment to be 0.5 m. For a telescope looking near zenith, r_0 can be as large as a few meters under good seeing conditions at infrared wavelengths. During poor seeing conditions at visible wavelengths, r_0 may be only a few centimeters [21].

High spatial frequencies correspond to fine image detail, therefore optical systems that permit these high frequencies are considered superior. The spatial frequency bandwidth of an optical system is closely related to the system's modulation transfer function (MTF). The MTF of an incident plane wave through turbulence as a function of spatial frequency ν is given by

$$MTF_{turb}(\nu) = \exp \left[-3.44 \left(\frac{\lambda f \nu}{r_0} \right)^{5/3} \right], \quad \frac{1}{L_0} \ll \nu \ll \frac{1}{l_0}, \quad (20)$$

where λ is the wavelength and f is the focal length of the telescope. Equation 20

displays how low spatial frequencies transmit more easily through turbulence and high spatial frequencies are largely filtered out [12]. This effect significantly degrades the resolution of images propagated through the atmosphere. When an optical imaging system is introduced, the resolution of the system becomes a function of the MTF of the turbulence and the receiver optics by

$$\begin{aligned} R &= \int_0^{2\pi} \int_0^{\frac{D}{\lambda f}} MTF_O(\nu) MTF_{turb}(\nu) \nu d\nu d\theta \\ &= \frac{4D^2}{\lambda^2 f^2} \int_0^1 u \left(\cos^{-1} u - u\sqrt{1-u^2} \right) \exp \left[-3.44 \left(\frac{Du}{r_0} \right)^{5/3} \right] du, \end{aligned} \quad (21)$$

where D is the diameter of the telescope aperture. Equation 21 limits the resolution of the system under turbulent conditions to

$$R_{max} = \frac{\pi r_o^2}{4\lambda^2 f^2}. \quad (22)$$

The ratio of the system resolution to the maximum resolution can then be closely approximated as a function of the aperture diameter and Fried's parameter as

$$\frac{R}{R_{max}} \approx \frac{\left(\frac{D}{r_0} \right)^2}{\left(1 + \left(\frac{D}{r_0} \right)^{5/3} \right)^{6/5}}. \quad (23)$$

By Equation 23, the ratio is approximately 1 when $D \gg r_0$ and approximately $(D/r_0)^2$ when $D \ll r_0$. Therefore, optical performance of the system is heavily dependent on the aperture size and Fried's parameter, which imposes a strict limit to the telescope's aperture size.

At its core, turbulence is a non-linear process in a viscous medium with motion

described by the incompressible Navier-Stokes equation

$$\partial_t \mathbf{v} + \mathbf{v} \cdot \nabla \mathbf{v} = -\nabla p + \nu \nabla^2 \mathbf{v} \quad (24)$$

$$\nabla \cdot \mathbf{v} = 0, \quad (25)$$

where ∂_t is a partial time derivative, \mathbf{v} is the flow velocity vector, p is the pressure, and ν is the kinematic viscosity [14]. Theoretically, one should be able to predict the movement of all turbulent flow using the Navier-Stokes equations. However, three-dimensional closed-form solutions to the Navier-Stokes equations have not yet been proven to exist for all systems due to the sheer amount of random parameters that must be considered. Therefore, it is currently only possible to describe turbulence in a statistical sense and through use of approximations.

2.3 Statistical Model of the Atmosphere

Many cases of random processes can be described accurately using stationary random functions. This is not the case for the main atmospheric parameters: wind velocity fluctuations, temperature fluctuations, and refractive index fluctuations. Each of these fields vary spatially and temporally with mean values that are only constant over short periods of time. Therefore the fields may only be considered stationary over short increments. In order to describe processes of this nature, a function must account for the shifting mean [12]. This is the purpose of the structure function. A random process $x(t)$ can be described by

$$x(t) = m(t) + x_1(t), \quad (26)$$

where $m(t)$ is the mean of x and $x_1(t)$ satisfies $\langle x_1(t) \rangle = 0$ to account for the time-varying average, which is a zero-mean fluctuation. The structure function of this

process is then

$$\begin{aligned} D_x(t_1, t_2) &= \langle [x(t_1) - x(t_2)]^2 \rangle \\ &= [m(t_1) - m(t_2)]^2 + \langle [x_1(t_1) - x_1(t_2)]^2 \rangle. \end{aligned} \quad (27)$$

If the mean of $x(t)$ varies slowly, the first term in Equation 27 becomes negligible [12].

In the time domain, a stationary random process $x(t)$ can be described by the correlation function

$$R_x(\tau) = \langle x(t)x^*(t + \tau) \rangle, \quad (28)$$

where τ is the stationary increment in time. Similarly, the covariance function is

$$B_x(\tau) = R_x(\tau) - |m|^2. \quad (29)$$

Clearly, if the mean value of $x(t)$ is zero, its correlation and covariance functions are equal. When the time step is zero ($\tau = 0$), $B_x(0)$ is simply the variance of the variable x . For a zero-mean random process and by the Riemann-Stieltjes integral

$$x(t) = \int_{-\infty}^{\infty} e^{i\omega t} d\nu(\omega), \quad (30)$$

the covariance/correlation function can be written

$$B_x(\tau) = \int \int_{-\infty}^{\infty} e^{i(\omega_1 t_1 - \omega_2 t_2)} \langle d\nu(\omega_1) d\nu^*(\omega_2) \rangle. \quad (31)$$

The Wiener-Khintchine theorem states the covariance function is related to the power spectral density (PSD) function as a Fourier transform pair. The PSD function describes the distribution of power amongst the frequency components of the signal.

The relation between the two is

$$B_x(\tau) = \int_{-\infty}^{\infty} e^{i\omega\tau} S_x(\omega) d\omega \quad (32)$$

$$S_x(\omega) = \int_{-\infty}^{\infty} e^{-i\omega\tau} B_x(\tau) d\tau, \quad (33)$$

where S_x represents the PSD.

A random process is considered stationary if its statistical properties don't vary in time. Equivalently, the probability density function (PDF) of a stationary random process is dependent solely on time increments τ [12]. In turn, this means the random field in question must be statistically homogeneous and isotropic. Atmospheric turbulence can be treated as a process that is stationary only in increments. Therefore, the covariance function is not applicable to most cases of turbulence. For this reason, the structure function is generally used instead to describe the random turbulent processes even though it contains less information.

The functions described in this section are only approximations that estimate the stochastic field as locally homogeneous. Kolmogorov[22] worked based on these approximations in order to develop his theory of turbulence and thus did not derive his work from first principles.

2.4 Kolmogorov Theory

In the earliest days turbulence research, it was regarded as a purely stochastic, or random, process. Andrei Kolmogorov in 1941 was the first to begin viewing turbulence using statistics, which allowed it to be theoretically modeled [12]. Kolmogorov adopted Richardson's energy cascade theory of turbulence. In the Kolmogorov theory, eddies smaller than the outer scale are assumed to be statistically homogeneous and isotropic (no preferential direction), while eddies larger or equal to the outer scale are

assumed to be anisotropic with ill-defined structure [12]. Therefore, Kolmogorov's statistical approach to turbulence only applies to eddies within the inertial subrange.

The spatial and temporal fluctuations of refractive index are described by the structure function

$$D_n(\mathbf{r}) = \langle (\partial n)^2 \rangle = \langle [n(\mathbf{x}, t) - n(\mathbf{x} + \mathbf{r}, t)]^2 \rangle, \quad (34)$$

where $\langle \rangle$ represents ensemble averaging, n is the refractive index, \mathbf{r} is the separation vector, t is time, and \mathbf{x} is the position vector. Under Kolmogorov's assumptions for large Reynold's numbers and at scales below L_0 , the structure function becomes

$$D_n(r) = \begin{cases} C_n^2 l_0^{-4/3} r^2, & 0 \leq r \ll l_0 \\ C_n^2 r^{2/3}, & l_0 \ll r \ll L_0 \end{cases} \quad (35)$$

where C_n^2 is the refractive index structure parameter (units $\text{m}^{-2/3}$) and r is now the magnitude of the separation vector [7]. The spatial variations in refractive index have been empirically related to the temperature and pressure at the same point by

$$\begin{aligned} n(\mathbf{r}) &= 1 + 77.6 \times 10^{-6} \left(1 + \frac{7.52 \times 10^{-3}}{\lambda^2} \right) \frac{P(\mathbf{r})}{T(\mathbf{r})^2} \\ &\approx 1 + 79.2 \times 10^{-6} \frac{P(\mathbf{r})}{T(\mathbf{r})^2}, \end{aligned} \quad (36)$$

where λ is the optical wavelength on the order of $0.5 \mu\text{m}$ [12]. As shown in Equation 36, the index of refraction at \mathbf{r} is inversely proportional to the temperature at \mathbf{r} . This gives rise to a relation between C_n^2 and the temperature structure parameter C_T^2 [23] by

$$C_n^2 = \left(79.2 \times 10^{-6} \frac{P(\mathbf{r})}{T(\mathbf{r})^2} \right)^2 C_T^2. \quad (37)$$

Physically, C_n^2 describes the strength of the refractive index fluctuations in space and time, which indicates the extent of the distortion a wavefront will experience when passing through that region at that instance. C_n^2 generally ranges from 10^{-17} to $10^{-12} \text{ m}^{-2/3}$, with larger values indicating “stronger” turbulence. C_n^2 values tend to be largest at the Earth’s surface due to mechanical mixing and greater convective flow effects and decrease as a function of height above the surface [12]. The structure parameters for temperature and humidity, C_T^2 and C_q^2 , are defined similarly for their respective structure functions [7]. Kolmogorov showed by dimensional analysis that each of these structure functions follows a universal 2/3 power law within the inertial subrange. The 2/3 power law states generally that for a turbulent flow at large Reynold’s numbers, the mean squared increments of velocity, temperature, and refractive index between two points behave as the 2/3 power of their separation distance [14].

If the refractive index of the atmosphere is assumed to behave as a random process of fluctuating index about a mean value (Equation 26), the covariance of the refractive index field is then

$$B_n = \langle n_1(\mathbf{r} + \mathbf{r}_1)n_1(\mathbf{r}_1) \rangle, \quad (38)$$

where $\langle \rangle$ represents an ensemble average. The three-dimensional power spectrum of phase fluctuations, also known as the power spectral density (PSD), is the Fourier transform of this covariance

$$\Phi_n(\kappa) = \frac{1}{(2\pi)^3} \int d^3r B_n(r) e^{-i\kappa r}, \quad (39)$$

where κ is the three dimensional spatial wavenumber (units $\frac{\text{rad}}{\text{m}}$). Within the inertial subrange, by changing to spherical coordinates and calculating the ensemble average,

the PSD becomes

$$\Phi_n(\kappa) = \frac{5}{18\pi} C_n^2 \kappa^{-3} \int_{l_0}^{L_0} \sin(\kappa r) r^{-1/3} dr. \quad (40)$$

If the integral limits are allowed to diverge, $l_0 \rightarrow 0$ and $L_0 \rightarrow \infty$, the PSD follows a -11/3 power law known as the Kolmogorov spectrum [4, 6] according to

$$\Phi_n(\kappa) = 0.033 C_n^2 \kappa^{-11/3}, \quad \frac{1}{L_0} \ll \kappa \ll \frac{1}{l_0}. \quad (41)$$

The one-dimensional analog to Equation 41 follows a -5/3 power law. C_v^2 and C_T^2 follow the same power law. Outside of the inertial subrange, both the 2/3 and the -11/3 power laws begin to break down. Each of Kolmogorov's theorems have been consistent across a number of experiments [24], yet there is still no solution that begins with the Navier-Stokes equations to derive these laws. Experimental methods of measuring turbulence using Kolmogorov's theories have been in use for decades and have proven their credibility.

2.5 Methods of Turbulence Profiling

SLODAR and SCIDAR are both triangulation-based remote sensing methods for determining the distribution of atmospheric optical turbulence that have proven effective in the past. Both methods are used by astronomers to produce vertical profiles of C_n^2 . They can also be used to record temporal and spatial characteristics of turbulence at different altitudes as the overall structure is shifted by the wind.

The classical SCIDAR technique as described in the literature [5, 8] uses detection of scintillation, or fluctuations in intensity, in the pupil plane of a telescope to generate the C_n^2 profile. A generalized SCIDAR technique first suggested by Fuchs [25] extracts spatial information from the scintillation images of double star targets (binary star systems) to produce vertical C_n^2 profiles of the total atmosphere. Wave-

fronts emerging from a star can be considered planar by the time they reach the Earth. When these wavefronts pass through layers of turbulence at height h , they form scintillation diffraction patterns relative to the C_n^2 structure they pass through. The second star in the binary pair, separated by θ (typically a few arcseconds), will produce wavefronts that are distorted in a slightly different manner because of the differences in propagation path through the turbulent layers. The cross-correlation function of the two scintillation patterns shows a peak at the distance θh with amplitude proportional to C_n^2 [9]. If multiple layers of turbulence are observed rather than just one, they each impose independent intensity perturbations. The cross-correlation function represents the sum of the contributions from each layer. If the two spatial autocorrelation functions in the parallel and perpendicular directions to the star separation are represented by C_{\parallel} and C_{\perp} respectively, then their difference (as given by Avila et al. [9]) is

$$\begin{aligned} B(x) &= C_{\parallel} - C_{\perp} \\ &= \int_0^{\infty} dh K(x, h) C_n^2(h) + N(x), \end{aligned} \quad (42)$$

where $B(x)$ is the difference of the two autocorrelation functions measured at the pupil plane of the telescope by a charge-coupled device (CCD). $K(x, h)$ is known as a kernel and is the theoretical autocorrelation function generated by a single layer of turbulence at height h . $N(x)$ is the estimated noise over the system. $K(x, h)$ is a diagonal matrix and can therefore be inverted to obtain the $C_n^2(h)$ profile along the path.

The SCIDAR technique is ideal for astronomical imaging because of the long path distances. Scintillation occurs because of the atmosphere's diffractive effects. Therefore, there must be ample propagation distance from the source to the telescope for the effects to be impactful. As shown by Roddier [26], variance in scintillation is

proportional to $h^{5/6}$. For this reason, SCIDAR is restricted in measuring turbulence near the telescope.

SLODAR is a method similar to SCIDAR, with the main distinction being SLODAR uses phase aberrations on the wavefront rather than scintillation patterns. SLODAR is of particular interest to this thesis because the HTS uses SLODAR-type measurements to estimate the turbulence profile along a horizontal path. SLODAR relies on the measurements of local wavefront tilts (the first derivative of the wavefront) found by the Shack-Hartmann Wavefront Sensor (SHWFS) when observing a binary star system through turbulence. The $n \times n$ SHWFS lenslet array samples the wavefront and focuses a subimage of the wavefront patch onto a subaperture array, which measures the 2-dimensional spot motions (also called Zernike tilts or Z-tilts) of the subimage within each subaperture.

Wilson[27] outlines the following steps used in the SLODAR method to determine the turbulence profile:

1. Subimages from the SHWFS are recorded simultaneously for each star in the binary pair for short exposures such that the turbulence is invariant during image capture.
2. The centroid locations within each subaperture are measured to calculate local wavefront tilts in both the tip and tilt direction. The mean slope is subtracted from the stars' individual slopes to eliminate telescope tracking error.
3. The cross-correlation of the collected slopes is measured. From the slope, $s_{i,j}(t)$, of subaperture (i,j) at time t and the concurrent slope from the second star at a neighboring subaperture, $s'_{i+\delta i, j+\delta j}(t)$, where δi and δj are the separations,

the cross-correlation is

$$C(\delta i, \delta j) = \left\langle \sum_{i,j} \frac{s_{i,j}(t) s'_{i+\delta i, j+\delta j}(t)}{O(\delta i, \delta j)} \right\rangle. \quad (43)$$

The angled brackets indicate ensemble averaging over many individual frames and $O(\delta i, \delta j)$ is the number of overlapping subapertures for the given separation.

4. Similarly, the autocorrelation of a single star at a pair of subapertures is

$$A(\delta i, \delta j) = \left\langle \sum_{i,j} \frac{s_{i,j}(t) s_{i+\delta i, j+\delta j}(t)}{O(\delta i, \delta j)} \right\rangle. \quad (44)$$

The autocorrelation provides an estimate of the system's impulse response due to a single layer of turbulence. $A(\delta i, \delta j)$ can be deconvolved with $C(\delta i, \delta j)$ to recover the turbulence profile. If the axis of source separation is aligned with the SHWFS axes, only the one-dimensional cross-correlation along δi or δj must be calculated to recover the profile.

5. Given the normalized turbulence profile from Step 4, the full integrated turbulence strength along with r_0 estimates are found by tracking centroid motion with algorithms such as the differential image motion method (DIMM)[\[28\]](#).

The cross-covariance of two stochastic processes X and Y (e.g. two independent paths through turbulence) is a measure of the similarity between the two outcomes as a function of relative time between the two. The cross-covariance of X at time t_1 and Y at time t_2 is defined as

$$C_{XY}(t_1, t_2) = \langle (X_{t_1} - \langle X_{t_1} \rangle) (Y_{t_2} - \langle Y_{t_2} \rangle) \rangle, \quad (45)$$

where $\langle \rangle$ represents the expectation value operator. The cross-covariance function

introduces an anisoplanatic term, which causes the impulse response, or the shape of a turbulent layer's covariance at a set altitude, to fluctuate at points along the path. The impulse response of SLODAR relative to altitude and the power spectral density of turbulent phase fluctuations is then determined with a fractional error. Ignoring the previously introduced anisoplanatic effects and under Kolmogorov turbulence assumptions, the fractional error of C_n^2 calculation takes values anywhere from 0% at the telescope to 20% at the source [29].

The locations of discrete points along the path where C_n^2 is estimated are determined by the path crossings of the two stars, which are themselves determined by the lenslet array geometry and the angular separation of the star system as shown in Figure 3. If the number of subapertures is represented by n , the heights of each

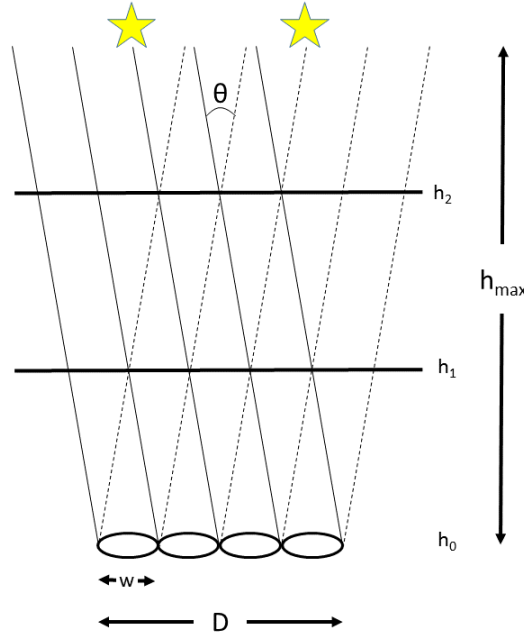


Figure 3. SLODAR geometry for a binary star system and $n = 4$ subaperture array. The crossings are determined by the angular separation between the stars, θ , and the diameter of the subapertures, w . D represents the diameter of the telescope pupil. Adapted from Goodwin [6].

subsequent crossing are given by $h_m = m \cdot \delta h$, where m ranges from 0 to $n-1$ and $\delta h = \frac{w}{\theta}$. The distance from the stars to the subaperture array is then $h_{\max} = \frac{D}{\theta}$. Star

pairs having a larger angular separation will lead to higher resolution data of ground layer turbulence (at the wavefront sensor) and lower resolution at the source end.

These methods, along with many others (differential imaging [3, 5], MASS [5], etc.) all attempt to estimate the turbulence profile along a path. Once the tilts along the path are known to a degree, the information can be fed into an adaptive optics imaging system, which can correct for the turbulence-induced distortion and allow for near aberration-free propagation through the turbulence.

2.6 Adaptive Optics

When left uncompensated, the effects of atmospheric turbulence on a wavefront include significant degradation like distortion and blur. This negative effect lead to the creation of adaptive optics (AO), which is used to improve the performance of optical systems that require propagation through the atmosphere. The overall purpose of AO is to compensate for wavefront distortion in real time using a closed loop by sensing the phase distortion of a known reference source and applying the conjugate phase to the outgoing beam (or incoming image) to correct the distortion. The main components of an AO imaging system are a deformable mirror to induce a controlled distortion to the wavefront, a wavefront sensor to measure turbulence degraded wavefronts, which determine how the mirror will be shaped, and an actuator command computer to shape the mirror properly [12]. The schematics of a typical AO system are shown in Figure 4.

AO systems attempt to constantly correct for the rapidly changing effects of the atmospheric distortion. Ideally, this allows for undistorted images to be received, which is of great interest to astronomers [30]. It also allows for laser wavefronts to be propagated such that they have little to no distortion upon contact with their target, which dramatically increases their lethality. However, the task of correcting for the

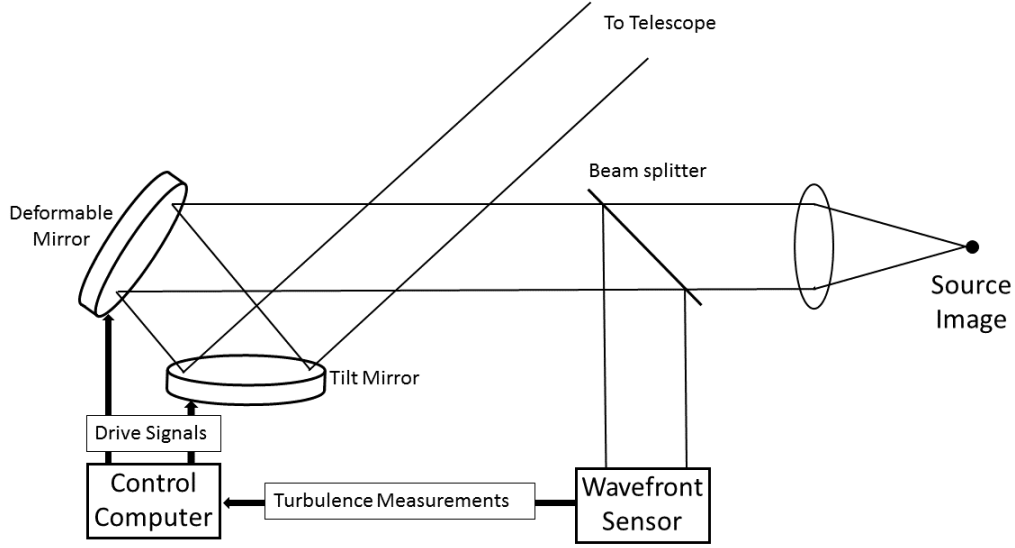


Figure 4. Schematics of an adaptive optics imaging system. The distorted source image is divided by a beam splitter and passed to a wavefront sensor. The wavefront sensor passes information about the wavefront distortion to a control computer, which in turn alters the shape of the deformable mirror to induce a conjugate phase on the corrected outgoing wavefront. Figure adapted from Tyson [4].

randomly shifting distortion imposed by atmospheric turbulence is non-trivial. The AO loop must be fed rapid and accurate information about the atmospheric conditions in order to function properly. In practice, AO systems are limited by the finite amount of incident light received by the wavefront sensor and the difference in the turbulence profile that may occur between the path of the known source and the outgoing signal. The latter effect is quantified with a variable known as the isoplanatic angle, θ_0 , which determines the field of view over which spatial invariance may be assumed [31]. Anisoplanatic tilt error in the optical system may lead to the deformable mirror not being shaped to the proper turbulence profile, leading to a non-ideal outgoing wavefront. If the path difference between the reference and the outgoing beam is greater than θ_0 , proper correction for the atmospheric distortion is not possible. Just like r_0 , the isoplanatic angle is closely related to the MTF of the optical system. θ_0

represents the $1/e$ point of the MTF assuming a spherical wave by

$$MTF_{\theta}(\theta) = \exp \left[- \left(\frac{\theta}{\theta_0} \right)^{5/3} \right]. \quad (46)$$

The isoplanatic angle in Equation 46 can be written

$$\theta_0 = \left[2.91 k^2 \int_0^L C_n^2(z) z^{5/3} dz \right]^{-3/5}. \quad (47)$$

Greenwood [32] studied formulas for the bandwidth of AO systems and in doing so, proposed a term to quantify the characteristic atmospheric frequency, which is now known as the Greenwood frequency, f_G . He defined the characteristic frequency as

$$f_G = \left[0.0196 \left(\frac{k}{\sigma_r} \right)^2 \int_0^L C_n^2(z) v^{5/3}(z) dz \right]^{3/5}, \quad (48)$$

where σ_r is the total uncorrected power and $v(z)$ is the wind speed transverse to the propagation path. Greenwood proposed two specific cases and how the characteristic frequency is defined for each: ground-based operations along near-horizontal paths and astronomical observations [32]. The case of interest for this thesis is the near-horizontal path, which Greenwood defined as

$$f_G = \left\{ 7.34 \times 10^{-3} \left(\frac{k}{\sigma_r} \right)^2 C_n^2 \frac{v^{8/3}}{\omega} \left[\left(1 + \frac{\omega L}{v} \right)^{8/3} - 1 \right] \right\}^{3/5}, \quad (49)$$

where C_n^2 is assumed to be constant along the path and the transverse wind speed is composed of a constant v and a pseudowind ωz in terms of an angular slew rate ω . The reciprocal of the Greenwood frequency is known as the Greenwood time constant, τ_0 , which gives the time interval over which the turbulent conditions remain essentially constant. For constant transverse wind speed v_{\perp} , the characteristic time constant is

directly related to the Fried parameter by

$$\tau_0 = \frac{0.32r_0}{v_\perp}, \quad (50)$$

which is typically on the order of ms [32].

The performance of AO systems is measured in many ways. One method of classification is known as the Strehl ratio (SR), which is defined as the ratio of the maximum mean irradiance in the focal plane through turbulence vs. free-space propagation. Under weak turbulence conditions, the SR can also be written in terms of the ratio of the point spread functions (PSF) of turbulent conditions to free-space conditions by

$$SR = \frac{PSF(0)}{PSF_0(0)} = \frac{1}{1 + (D/r_0)^{5/3}} \quad D/r_0 \ll 1, \quad (51)$$

where D is the aperture diameter. The PSF, or impulse response, of an incoherent imaging system represents the system's irradiance in the output plane in response to a point source.

2.7 Multi-Conjugate Adaptive Optics

Adaptive optics methods are a very promising solution to correcting the phase distortions induced by optical turbulence. However, use of a single deformable mirror (DM) in wavefront correction has limitations over extended regions of interest. A single mirror is only capable of improving wavefront/image quality over a small angular field of view [33]. AO telescopes are only effective over a field area that is approximately the size of the isoplanatic patch. For this reason, AO systems can produce high-resolution images of binary stars, but are incapable of correcting images of planets and galaxies. One method proposed to increase the corrected field of view of AO telescopes is to apply a three-dimensional phase correction by a series of DM's placed

in the optical train of the telescope [34]. It is widely accepted that a greater number of deformable mirrors operated in series could provide full phase correction even during highly anisoplanatic situations [4]. This method is known as multi-conjugate adaptive optics (MCAO). Despite the agreement on its potential, technical hurdles and cost considerations have limited the use of MCAO systems [33]. In order for a MCAO system to apply the proper conjugate phase for each atmospheric layer, the profile of the turbulence must be known.

It has been shown[35] that atmospheric turbulence is often concentrated within vertical layers rather than being uniformly distributed. MCAO systems attempt to correct for each “layer” separately by assigning a deformable mirror to each section, effectively increasing the isoplanatic patch [4]. Even in the absence of measurement noise, angular anisoplanatism serves as the limit to AO telescope performance [34]. The schematic difference between a single DM AO system and a two-mirror MCAO system are shown in Figure 5.

It can be assumed that the atmosphere is composed of discrete thin layers of turbulence at varying heights. In the near-field approximation, the resulting phase $\Phi(\mathbf{r}, \boldsymbol{\alpha})$ at the telescope pupil from zenith angle $\boldsymbol{\alpha}$ is the sum of the contributions from each layer

$$\Phi(\mathbf{r}, \boldsymbol{\alpha}) = \sum_{j=1}^{N_t} \Phi_j(\mathbf{r} + h_j \boldsymbol{\alpha}), \quad (52)$$

where \mathbf{r} is the pupil coordinate, Φ_j are the phase distortions by the j^{th} turbulence layer at altitude h_j , and N_t is the total number of layers [36]. Each phase is corrected by a different DM at the image of the respective turbulence layer.

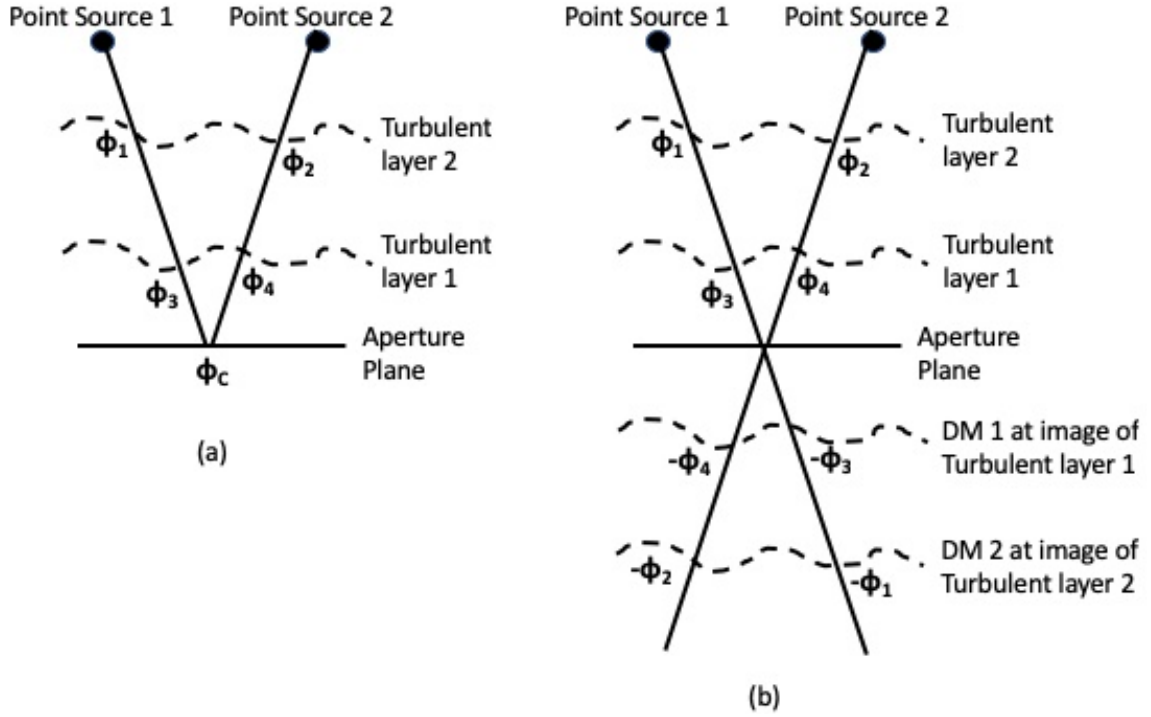


Figure 5. Schematic comparison of a single mirror AO system (a) and a two-mirror MCAO system (b) when observing two individual layers of turbulence (e.g. surface layer and tropopause). Φ_i at each crossing represents the phase distortion from that location. Φ_c is the corrective phase. Adapted from Johnston et al. [34].

III. Experiment

This chapter serves to connect the ideas discussed in Chapter 2 with the work done in this thesis. The theory applied to the work, in particular the weighting functions, is derived. The constrained nonlinear optimizer used to enhance the C_n^2 profiles is detailed. An outline of the equipment used for the experiment and the specifications of each device is presented. Lastly, the methodology of the experiment is laid out in full detail.

3.1 Theory

Weighting Functions.

The weighting functions used to generate C_n^2 profiles from the HTS data have been derived thoroughly by Fried [19] and Bose-Pillai [2] and will be derived again here. Consider the geometry of a pair of point sources and a pair of subapertures as shown in Figure 6.

Differential angle of arrival (i.e. first derivative of the phase difference) measurement using two sources reduces common mode noise in the measurements (e.g. platform vibrations and angular tracking error). By the geometric weighting function method used in this work, it would not be possible to profile with a single beacon. With one source, the beacon to aperture geometry would produce weighting functions that are too similar to one another to accurately profile the turbulence. Fried [37] relates the mean-square differential angle of arrival between two subapertures, $\langle(\alpha_1 - \alpha_2)^2\rangle$, to the coherence length, r_0 , by

$$\langle(\alpha_1 - \alpha_2)^2\rangle = \langle\alpha^2\rangle I(S, \Psi), \quad (53)$$

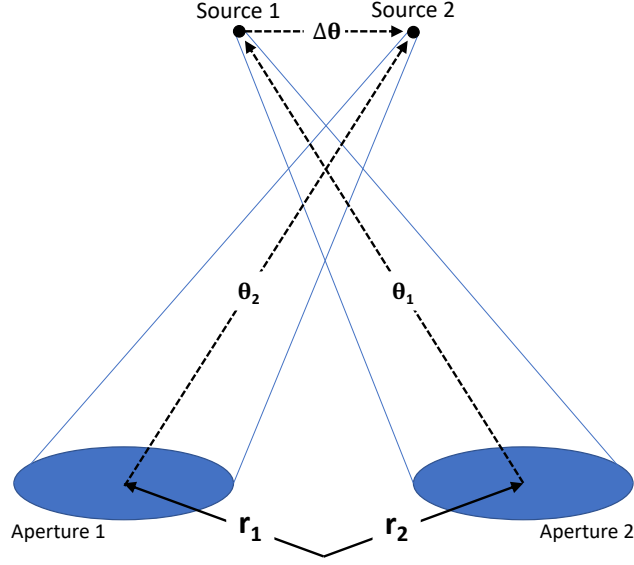


Figure 6. Geometry of a subaperture pair with two sources used to derive the crossing weighting functions.

where $\langle \alpha^2 \rangle$ is the two-axis mean-square tilt defined by

$$\langle \alpha^2 \rangle = \langle (\alpha_x)^2 + (\alpha_y)^2 \rangle \quad (54)$$

$$= 1.027 \left(\frac{3.44}{\pi^2} \right) \left(\frac{\lambda}{D} \right)^{1/3} \left(\frac{\lambda}{r_0} \right)^{5/3} \quad (55)$$

and $I(S, \Psi)$ can be written as

$$\begin{aligned} I(S, \Psi) = & \left(\frac{16}{\pi} \right)^2 \int_0^2 \pi d\theta \int_0^1 du \\ & u \left\{ \frac{1}{8} \cos^{-1}(u) + \sqrt{1-u^2} \left[\left(\frac{u^3}{12} - \frac{5u}{24} \right) + \left(\frac{u^3}{3} - \frac{u}{3} \right) \cos^2(\theta) \right] \right\} \\ & \cdot \left\{ [S^2 + 2S u \cos(\theta + \Psi) + u^2]^{5/6} + [S^2 - 2S u \cos(\theta + \Psi) + u^2]^{5/6} - 2u^{5/3} \right\}, \end{aligned} \quad (56)$$

where $S = \frac{\bar{S}}{D}$. Equation 56 can be evaluated numerically for various subaperture separations/diameters and the angle of tilt direction relative to the separation vector of the two subapertures ($\Psi = 0$ for parallel and $\Psi = \pi/2$ for perpendicular). The

geometry of the sensing path and aperture separation vector between one source and two subapertures will always form a triangle with no path crossings. This ultimately results in multiple scaled versions of the same weighting function, making it impossible to correctly profile the turbulence due to lack of variability between weighting functions. The clearest solution to these issues is to introduce a second beacon for profiling. Calculating the mean-square difference in angle of arrival measurements between the two sources eliminates the tracking error, which is equivalent for both sources and therefore drops out of the difference. A second source also allows for the generation of multiple weighting functions with greater variability over the path, thus making profiling possible.

The subapertures in Figure 6, each with diameter D , are located at positions \mathbf{r}_1 and \mathbf{r}_2 with centers separated by $\mathbf{s} = \mathbf{r}_2 - \mathbf{r}_1$. The Z-tilt of the 2^{nd} source image at the 1^{st} aperture in the direction $\boldsymbol{\theta}_2$ is given by

$$\boldsymbol{\alpha}_1(\boldsymbol{\theta}_2) = \frac{32\lambda}{\pi^2 D^4} \int W(\mathbf{r} - \mathbf{r}_1) \phi(\mathbf{r}, \boldsymbol{\theta}_2) d\mathbf{r}(\mathbf{r} - \mathbf{r}_1), \quad (57)$$

where λ is the wavelength, $\phi(\mathbf{r}, \boldsymbol{\theta}_2)$ is the wavefront distortion experienced by the 2^{nd} source following propagation through turbulence to coordinate \mathbf{r} , and bold font indicates a vector quantity. $W(\mathbf{r} - \mathbf{r}_1)$ is called the circular aperture function, which serves to limit the region of integration, which would otherwise be infinite over the aperture plane, by

$$W(\mathbf{r} - \mathbf{r}_1) = \begin{cases} 1, & \mathbf{r} - \mathbf{r}_1 \leq \frac{D}{2} \\ 0, & \mathbf{r} - \mathbf{r}_1 > \frac{D}{2} \end{cases} \quad (58)$$

The Z-tilt across the 2^{nd} aperture by the 1^{st} source in direction θ_1 is given similarly by

$$\boldsymbol{\alpha}_2(\boldsymbol{\theta}_1) = \frac{32\lambda}{\pi^2 D^4} \int W(\mathbf{r} - \mathbf{r}_2) \phi(\mathbf{r}, \boldsymbol{\theta}_1) d\mathbf{r}(\mathbf{r} - \mathbf{r}_2). \quad (59)$$

The Z-tilts are zero-mean random processes, which allows for the differential tilt variance to be expressed as

$$\begin{aligned}
\left\langle \left[\alpha_1(\theta_2) - \alpha_2(\theta_1) \right]^2 \right\rangle &= \left\langle \left[\alpha_1(\theta_2) - \alpha_2(\theta_1) \right] \cdot \left[\alpha_1(\theta_2) - \alpha_2(\theta_1) \right] \right\rangle \\
&= \left(\frac{32\lambda}{\pi^2 D^4} \right)^2 \left\langle \int \int d\mathbf{r} d\mathbf{r}' \left[(\mathbf{r} - \mathbf{r}_1) W(\mathbf{r} - \mathbf{r}_1) \phi(\mathbf{r}, \theta_2) - (\mathbf{r} - \mathbf{r}_2) W(\mathbf{r} - \mathbf{r}_2) \phi(\mathbf{r}, \theta_1) \right] \right. \\
&\quad \cdot \left. \left[(\mathbf{r}' - \mathbf{r}_1) W(\mathbf{r}' - \mathbf{r}_1) \phi(\mathbf{r}', \theta_2) - (\mathbf{r}' - \mathbf{r}_2) W(\mathbf{r}' - \mathbf{r}_2) \phi(\mathbf{r}', \theta_1) \right] \right\rangle,
\end{aligned} \tag{60}$$

where $\langle \rangle$ represents ensemble averaging. By changing the order of the integration and ensemble averaging and multiplying the individual pieces, Equation 60 can be written equivalently as

$$\begin{aligned}
\left\langle \left[\alpha_1(\theta_2) - \alpha_2(\theta_1) \right]^2 \right\rangle &= \left(\frac{32\lambda}{\pi^2 D^4} \right)^2 \cdot \\
&\quad \left[\iint d\mathbf{r} d\mathbf{r}' (\mathbf{r} - \mathbf{r}_1) \cdot (\mathbf{r}' - \mathbf{r}_1) W(\mathbf{r} - \mathbf{r}_1) W(\mathbf{r}' - \mathbf{r}_1) \langle \phi(\mathbf{r}, \theta_2) \phi(\mathbf{r}', \theta_2) \rangle \right. \\
&\quad - \iint d\mathbf{r} d\mathbf{r}' (\mathbf{r} - \mathbf{r}_2) \cdot (\mathbf{r}' - \mathbf{r}_1) W(\mathbf{r} - \mathbf{r}_2) W(\mathbf{r}' - \mathbf{r}_1) \langle \phi(\mathbf{r}, \theta_1) \phi(\mathbf{r}', \theta_2) \rangle \\
&\quad - \iint d\mathbf{r} d\mathbf{r}' (\mathbf{r} - \mathbf{r}_1) \cdot (\mathbf{r}' - \mathbf{r}_2) W(\mathbf{r} - \mathbf{r}_1) W(\mathbf{r}' - \mathbf{r}_2) \langle \phi(\mathbf{r}, \theta_2) \phi(\mathbf{r}', \theta_1) \rangle \\
&\quad \left. + \iint d\mathbf{r} d\mathbf{r}' (\mathbf{r} - \mathbf{r}_2) \cdot (\mathbf{r}' - \mathbf{r}_2) W(\mathbf{r} - \mathbf{r}_2) W(\mathbf{r}' - \mathbf{r}_2) \langle \phi(\mathbf{r}, \theta_1) \phi(\mathbf{r}', \theta_1) \rangle \right].
\end{aligned} \tag{61}$$

Alternatively, this is written as

$$\begin{aligned}
\left\langle \left[\alpha_1(\theta_2) - \alpha_2(\theta_1) \right]^2 \right\rangle &= \left(\frac{32\lambda}{\pi^2 D^4} \right)^2 \cdot \\
&\left[\iint d\mathbf{r} d\mathbf{r}' (\mathbf{r} \cdot \mathbf{r}') W(\mathbf{r}) W(\mathbf{r}') \langle \phi(\mathbf{r} + \mathbf{r}_1, \theta_2) \phi(\mathbf{r}' + \mathbf{r}_1, \theta_2) \rangle \right. \\
&- \iint d\mathbf{r} d\mathbf{r}' (\mathbf{r} \cdot \mathbf{r}') W(\mathbf{r}) W(\mathbf{r}') \langle \phi(\mathbf{r} + \mathbf{r}_2, \theta_1) \phi(\mathbf{r}' + \mathbf{r}_1, \theta_2) \rangle \\
&- \iint d\mathbf{r} d\mathbf{r}' (\mathbf{r} \cdot \mathbf{r}') W(\mathbf{r}) W(\mathbf{r}') \langle \phi(\mathbf{r} + \mathbf{r}_1, \theta_2) \phi(\mathbf{r}' + \mathbf{r}_2, \theta_1) \rangle \\
&\left. + \iint d\mathbf{r} d\mathbf{r}' (\mathbf{r} \cdot \mathbf{r}') W(\mathbf{r}) W(\mathbf{r}') \langle \phi(\mathbf{r} + \mathbf{r}_2, \theta_1) \phi(\mathbf{r}' + \mathbf{r}_2, \theta_1) \rangle \right]. \tag{62}
\end{aligned}$$

Because $\iint d\mathbf{r} d\mathbf{r}' (\mathbf{r} \cdot \mathbf{r}') W(\mathbf{r}) W(\mathbf{r}') = 0$, terms that are functions of exclusively \mathbf{r} or \mathbf{r}' can be added to Equation 62 without changing the result. Therefore, Equation 62 can be written

$$\begin{aligned}
\left\langle \left[\alpha_1(\theta_2) - \alpha_2(\theta_1) \right]^2 \right\rangle &= - \left(\frac{32\lambda}{\pi^2 D^4} \right)^2 \cdot \left[\iint d\mathbf{r} d\mathbf{r}' (\mathbf{r} \cdot \mathbf{r}') W(\mathbf{r}) W(\mathbf{r}') \cdot \right. \\
&\left. \left[D_\phi(\mathbf{r} - \mathbf{r}') - \frac{1}{2} \{ D_\phi(\mathbf{r} - \mathbf{r}', \theta_1 - \theta_2, s) + D_\phi(\mathbf{r} - \mathbf{r}', \theta_2 - \theta_1, s) \} \right] \right], \tag{63}
\end{aligned}$$

where

$$\begin{aligned}
D_\phi(\mathbf{r} - \mathbf{r}') &= \left\langle [\phi(\mathbf{r} + \mathbf{r}_1, \theta_2) - \phi(\mathbf{r}' + \mathbf{r}_1, \theta_2)]^2 \right\rangle \\
&= \left\langle [\phi(\mathbf{r} + \mathbf{r}_2, \theta_1) - \phi(\mathbf{r}' + \mathbf{r}_2, \theta_1)]^2 \right\rangle, \tag{64}
\end{aligned}$$

and

$$D_\phi(\mathbf{r} - \mathbf{r}', \theta_1 - \theta_2, s) = \left\langle [\phi(\mathbf{r} + \mathbf{r}_2, \theta_1) - \phi(\mathbf{r}' + \mathbf{r}_1, \theta_2)]^2 \right\rangle, \tag{65}$$

$$D_\phi(\mathbf{r} - \mathbf{r}', \theta_2 - \theta_1, s) = \left\langle [\phi(\mathbf{r} + \mathbf{r}_1, \theta_2) - \phi(\mathbf{r}' + \mathbf{r}_2, \theta_1)]^2 \right\rangle \tag{66}$$

are the set of phase structure functions [2]. For the case of spherical wavefronts

propagating from each source through Kolmogorov turbulence defined with the power spectrum in Equation 41, Equation 63 can be written as

$$\begin{aligned} \left\langle \left[\alpha_1(\theta_2) - \alpha_2(\theta_1) \right]^2 \right\rangle &= -2.91k^2 \left(\frac{32\lambda}{\pi^2 D^4} \right)^2 \int_0^L dz C_n^2(z) \\ &\cdot \iint d\mathbf{r} d\mathbf{r}' (\mathbf{r} \cdot \mathbf{r}') W(\mathbf{r}) W(\mathbf{r}') \cdot \left[\left| (\mathbf{r} - \mathbf{r}') \left(1 - \frac{z}{L} \right) \right|^{5/3} \right. \\ &\left. - \frac{1}{2} \left\{ \left| (\mathbf{r} - \mathbf{r}') \left(1 - \frac{z}{L} \right) + \mathbf{s} - \Delta\theta \mathbf{z} \right|^{5/3} + \left| (\mathbf{r} - \mathbf{r}') \left(1 - \frac{z}{L} \right) - \mathbf{s} + \Delta\theta \mathbf{z} \right|^{5/3} \right\} \right], \end{aligned} \quad (67)$$

where $\Delta\theta = \theta_2 - \theta_1$ represents the angular distance between the sources, k is the wavenumber, and L is the path length. The HTS aperture plane is at $z = 0$ m and the helium-neon laser sources are at $z = L$. Equation 67 also assumes the wave structure function, which is the summation of the log-amplitude structure function and the phase structure function, is approximately equal to the phase structure function [2].

Fried[38] and Winick et al.[31] describe the technique to integrate over \mathbf{r} and \mathbf{r}' by a change of variables where $u = \frac{1}{D}(\mathbf{r} - \mathbf{r}')$ and $v = \frac{1}{2D}(\mathbf{r} + \mathbf{r}')$. These techniques reduce Equation 67 to

$$\left\langle \left[\alpha_1(\theta_2) - \alpha_2(\theta_1) \right]^2 \right\rangle = \int_0^L dz C_n^2(z) f_{dc}(z), \quad (68)$$

where $f_{dc}(z)$ is the crossing path weighting function defined by

$$\begin{aligned} f_{dc}(z) &= -2.91 \left(\frac{16}{\pi} \right)^2 D^{-1/3} \int_0^{2\pi} d\theta \int_0^1 du \\ &\left[(u \cos^{-1} u) - u^2 (3 - 2u^2) \sqrt{1 - u^2} \right] \cdot \left\{ \left| u \left(1 - \frac{z}{L} \right) \right|^{5/3} \right. \\ &- \frac{1}{2} \left[u^2 \left(1 - \frac{z}{L} \right)^2 + \left(\frac{|s - z\Delta\theta|}{D} \right)^2 + 2u \left(1 - \frac{z}{L} \right) \left(\frac{|s - z\Delta\theta|}{D} \right) \cos\theta \right]^{5/6} \\ &\left. - \frac{1}{2} \left[u^2 \left(1 - \frac{z}{L} \right)^2 + \left(\frac{|s - z\Delta\theta|}{D} \right)^2 - 2u \left(1 - \frac{z}{L} \right) \left(\frac{|s - z\Delta\theta|}{D} \right) \cos\theta \right]^{5/6} \right\}. \end{aligned} \quad (69)$$

Equation 69 can not be simplified any further and thus requires numerical evaluation from this point. Crossing path weighting functions are generated for every aperture

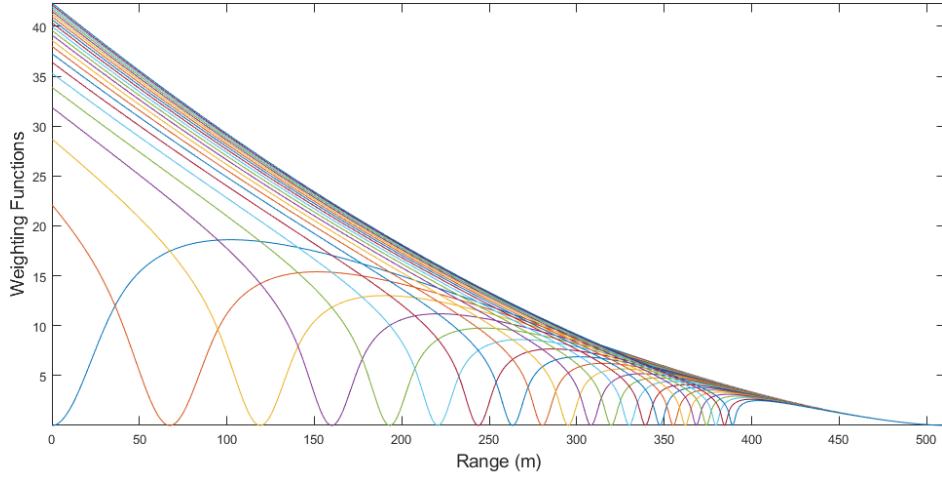


Figure 7. Path weighting functions over the 511 m range for 22 different subaperture separations. The HTS subaperture plane is located at $z = 0$ m and the HeNe sources are at $z = 511$ m. The weighting function with notch at 0 m is the self weighting function. Increasing the aperture separation moves the notch closer to the source end.

separation from 0 to 35.09 cm (increments of 1.67 cm), with the $s = 0$ cm separation weighting function known as the “self” weighting function because only one aperture is considered. The 22 weighting functions are plotted in Figure 7. Each weighting function drops to zero at the source end, implying that turbulence near the sources has almost no effect on the wavefront tilts observed by the HTS [2]. Each weighting function dips to zero at a singular point along the path. This location is where the two sensing paths from the sources and apertures cross as was shown in Figure 6. At the location of the crossing, the turbulence experienced by each sensing path is exactly the same, therefore the contribution to the differential tilts at that location has no effect on the signal.

The non-crossing weighting functions do not cross along the path, but rather behind the subapertures or sources as shown in Figure 8. As observed in Figure 8, $\frac{s}{d_{\perp}} = \frac{h}{h+z}$. Therefore, $d_{\perp} = \frac{s(h+z)}{h} = s + \frac{sz}{h}$. From the same geometry, $s = h\Delta\theta$. Hence, $d_{\perp} = s + z\Delta\theta$ for the non-crossing weighting functions, which differs from the crossing weighting functions where $d_{\perp} = s - z\Delta\theta$. From this, the non-crossing

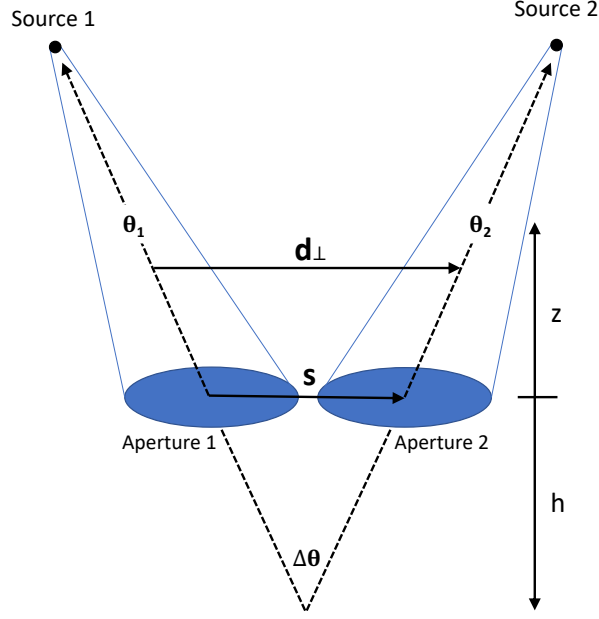


Figure 8. Source and aperture geometry of non-crossing weighting functions. The absence of path crossings produces weighting functions with no locations of zero influence.

weighting functions are then

$$\begin{aligned}
 f_{dc}(z) = & -2.91 \left(\frac{16}{\pi} \right)^2 D^{-1/3} \int_0^{2\pi} d\theta \int_0^1 du \\
 & \left[(u \cos^{-1} u) - u^2(3 - 2u^2)\sqrt{1 - u^2} \right] \cdot \left\{ \left| u \left(1 - \frac{z}{L} \right) \right|^{5/3} \right. \\
 & - \frac{1}{2} \left[u^2 \left(1 - \frac{z}{L} \right)^2 + \left(\frac{|s + z\Delta\theta|}{D} \right)^2 + 2u \left(1 - \frac{z}{L} \right) \left(\frac{|s + z\Delta\theta|}{D} \right) \cos\theta \right]^{5/6} \\
 & \left. - \frac{1}{2} \left[u^2 \left(1 - \frac{z}{L} \right)^2 + \left(\frac{|s + z\Delta\theta|}{D} \right)^2 - 2u \left(1 - \frac{z}{L} \right) \left(\frac{|s + z\Delta\theta|}{D} \right) \cos\theta \right]^{5/6} \right\}. \tag{70}
 \end{aligned}$$

Non-crossing weighting functions are calculated for every separation from 1.67 cm to 35.09 cm in increments of 1.67 cm. However, the functions produced for each separation end up very similar. For this reason, only the five closest separations and the largest separation non-crossing weighting functions were considered for this thesis. Through trial and error, it was determined this combination produced the optimal measurement noise cancellation and acted as DC values for the differenced crossing

weighting functions, which lose information about magnitude once differenced. The six utilized non-crossing weighting functions are shown in Figure 9. The non-crossing weighting function for the smallest subaperture separation has the smallest amplitude at $z = 0$ and the functions representing subsequent separations are ordered with increasingly larger values at the same location.

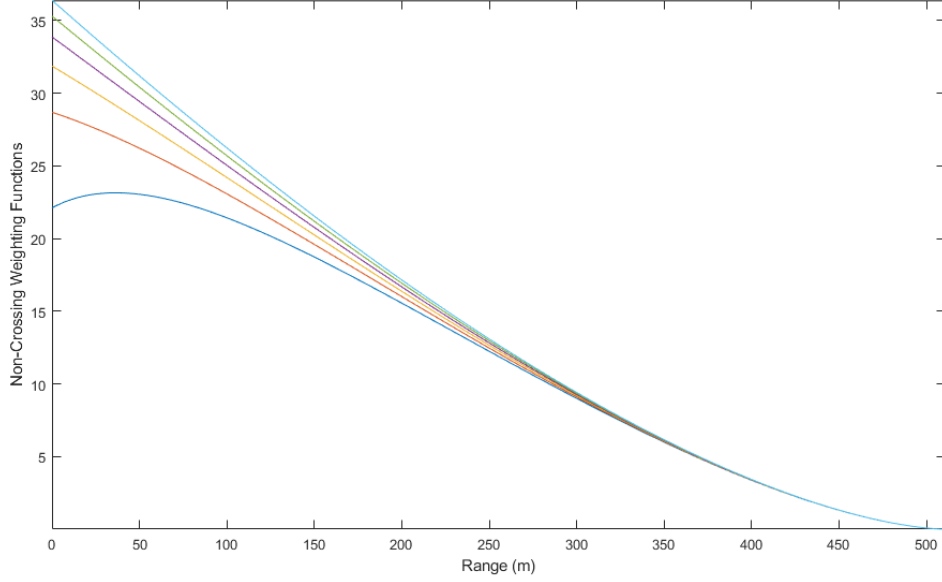


Figure 9. Non-crossing weighting functions for the five closest and largest aperture separations.

Once the 28 different crossing and non-crossing weighting functions are generated, they are combined into a 28×1023 matrix, \mathbf{M} , where each row corresponds to an individual weighting function and the columns are where the functions are sampled along the path (every 0.5 m for 511 m). Given this matrix, the estimated C_n^2 along the path is simply

$$C_{n,est}^2 = \mathbf{M}^+ \mathbf{V}, \quad (71)$$

where \mathbf{M}^+ is the Moore-Penrose pseudo-inverse of \mathbf{M} and \mathbf{V} is the set of differential tilt variances calculated for the same aperture separations as the weighting functions. The pseudo-inverse is calculated with respect to a given threshold, which ensures all

singular values of \mathbf{M} below the threshold are not inverted. In the absence of noise, the estimated C_n^2 values are related to the true values by

$$C_{n,est}^2 = \mathbf{M}^+ \mathbf{M} C_n^2, \quad (72)$$

where $\mathbf{M}^+ \mathbf{M}$ can be viewed as the influence function, or impulse response matrix, which describes how the estimated C_n^2 at a given position is affected by turbulence elsewhere.

The technique outlined above is prone to noise and sometimes leads to negative C_n^2 estimates, which are seen as gaps in the C_n^2 profile. This is especially common for lower pseudoinverse thresholds when the estimates can hit the noise floor. For this reason, larger thresholds are typically chosen to reduce noise. The trade-off for using larger thresholds is that weighting functions with singular values (from the singular value decomposition) lower than the threshold are set to zero during pseudoinverse calculation. Fewer weighting functions factor into estimates at larger thresholds, therefore higher thresholds lead to a smaller credible range and an influence function that “breaks” earlier along the path as shown in Figures 10 and 11. In practice, the smallest threshold that produces minimum C_n^2 dropouts was chosen for any one data set.

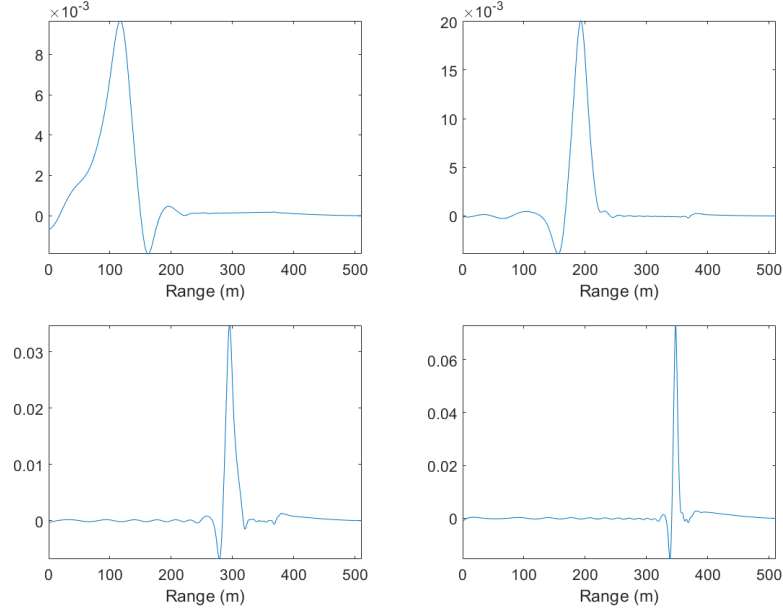


Figure 10. The influence function for a threshold of 11 at 100, 200, 300, and 350 m. The function breaks immediately past 350 m. 5 weighting functions have singular values below 11.

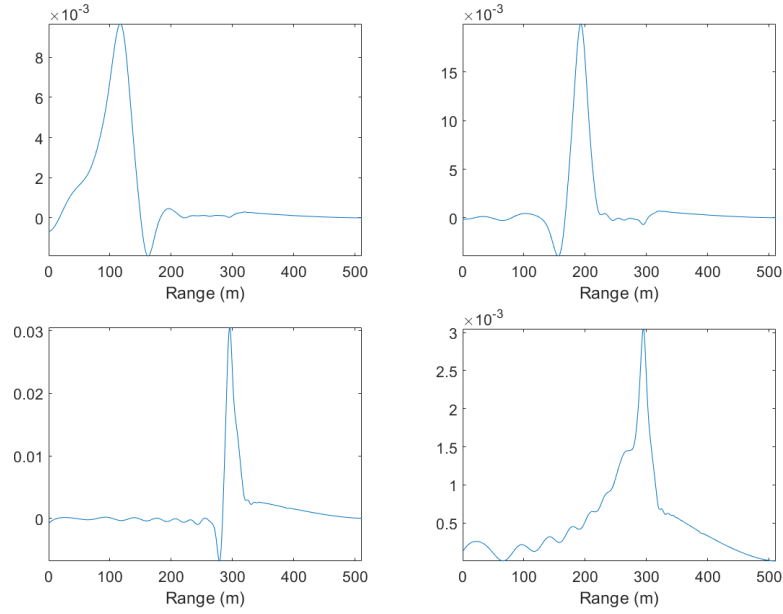


Figure 11. The influence function for a threshold of 31 at 100, 200, 300, and 350 m. The function now breaks near 300 m. 12 weighting functions have singular values below 31.

Constrained Nonlinear Optimization.

For data sets with particularly strong turbulence, an additional effort to reduce the measurement noise of the data must be applied. A constrained nonlinear optimizer function, which attempts to minimize an objective function, was chosen to improve the profiles. The objective function to beat measurement noise is

$$(\Delta x \mathbf{M} \mathbf{X} - \mathbf{V})^2, \quad (73)$$

where $\Delta x = \frac{1}{2}$ comes from the discretization of step sizes into half-meter increments, \mathbf{M} is the matrix of weighting functions at each discrete location, \mathbf{X} is the minimizer of the function in place of C_n^2 , and \mathbf{V} is the vector of tilt variances corresponding to each weighting function. The original profile with the thresholded pseudoinverse is passed to the optimizer as the initial guess. The negative C_n^2 values for each profile are set to a specified floor value, which is changed depending on the initial profile estimate. The lower and upper bounds of operation are also set based on the initial profile. A constraint on r_0 estimation for each data set was also used in the optimization.

3.2 Equipment

Hartmann Turbulence Sensor (HTS).

The HTS was designed to be the ideal tool for measuring local wavefront tilts due to optical turbulence. Brennan et al.[20] outlines 5 requirements for an ideal turbulence sensor:

1. A large telescope aperture to collect the maximum amount of light
2. A large collection of subapertures for statistical averaging

3. Small subapertures for inner scale estimation with $l_0 > 0.3d$ where d is the subaperture diameter
4. A high frame rate camera for estimation of high Greenwood frequencies and for differencing adjacent frames for noise estimation
5. A large dynamic range within each subaperture to measure large tilts during strong turbulence

Each of these specifications were taken into account when designing the HTS, a Shack-Hartmann wavefront sensor based on a 16" Meade LX200 coma-free telescope [1]. The Shack-Hartmann sensor takes pupil plane measurements of local wavefront tilts through use of a Thor Labs MLA150-5C lenslet array represented in Figure 12 [39].

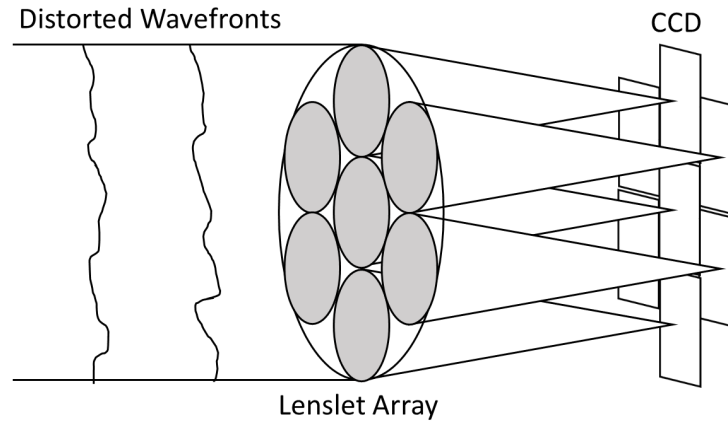


Figure 12. Schematic of the Shack-Hartmann wavefront sensor. Collimated wavefronts incident on the lenslet array are focused to different points on the focal plane array based on their local slopes [4].

The entire HTS system is mounted within a trailer on a floating suspension system, which protects the system during transportation. The custom optics bench within the HTS consists of a lenslet array, a Vision Research Phantom v7.3 high speed camera (captures up to 8,639 frames/sec [1]), and relay optics to collimate and invert the

image. Two 2.2 mW helium-neon (HeNe) laser beacons at 632.8 nm are incident on the telescope. The 632.8 nm wavelength corresponds to a peak in the Phantom camera's quantum efficiency [1]. Each laser was fitted with a beam expander to entirely illuminate the HTS telescope aperture. The center of the aperture is blocked by a central obscuration, which houses the secondary mirror. The telescope's pupil plane is imaged onto a 32×32 array of lenslets, which sample the wavefront and focus subimages onto the Phantom camera's CCD. On the CCD, an 18×18 pixel region is designated for each subaperture.

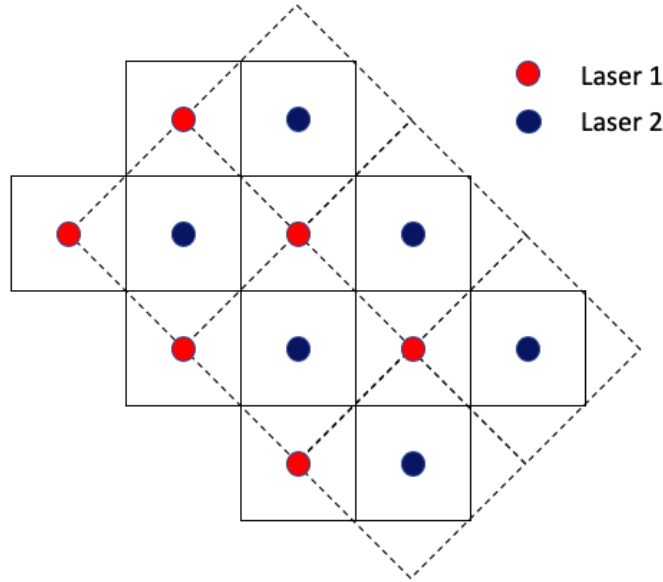


Figure 13. Original 18×18 pixel grid (dashed) compared to modified 12.7×12.7 pixel grid (solid). Telescope magnification is altered slightly to get 13×13 pixel regions for each spot.

The lenslet array directs the incident wavefronts onto the Phantom camera's CCD, where their point of focus is determined by local tilts as shown in Figure 14.

For this experiment, the subaperture mask was rotated by 45 degrees to provide more separation between the focused spots from the two lasers. This resulted in a 12.7×12.7 pixel region for the subimage from each laser. To avoid the complexity of fractional pixel computation, the telescope magnification was slightly altered such

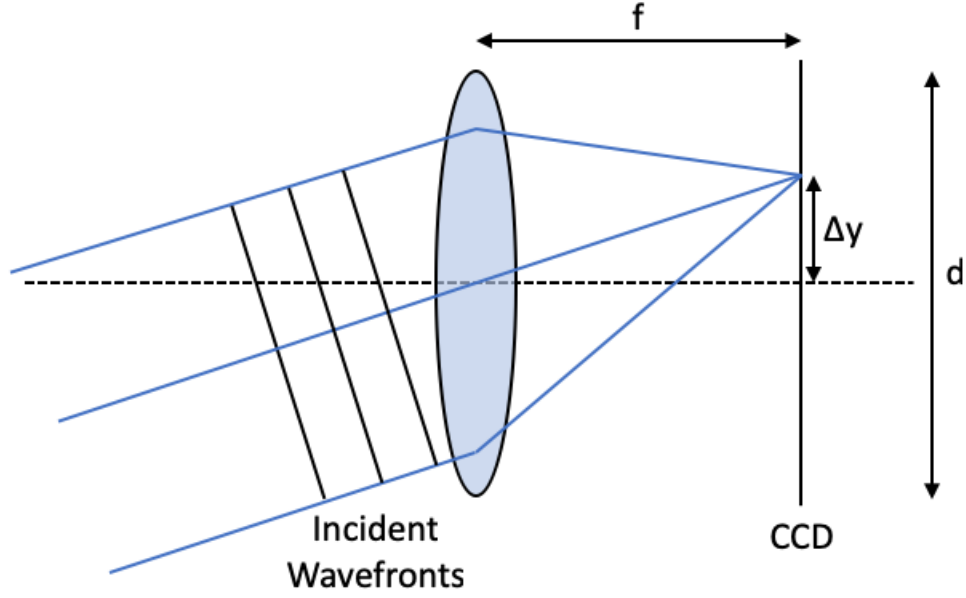


Figure 14. Depiction of how a microlens' focus point is affected by the local wavefront tilt. Here, f is the lens' focal length, Δy is the displacement of the focus from the optical axis, and d is the lens diameter.

that the mean focus position lie at the center of 13×13 pixel boxes [2]. The resulting subaperture mask is shown in Figure 13. The circular lenslets, each with focal length 5.2 mm, are $146 \mu\text{m}$ in diameter and arranged in a square grid spaced $150 \mu\text{m}$ apart with the areas between lenses masked with chrome to prevent light from passing through [1].

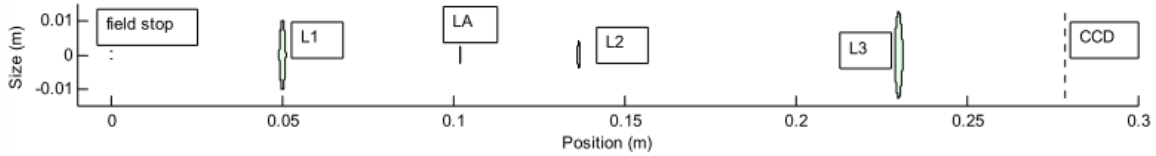


Figure 15. Approximate locations of the optics on the HTS optical bench. The focal plane of the telescope is at 0 m. L1 collimates the telescope beam through the lenslet array (LA). L2 and L3 invert the image vertically and recollimate the beam onto the CCD[1].

The optical setup of the HTS is depicted in Figure 15. The alignment procedure is outlined thoroughly in the HTS manual [1]. The system must be aligned using an alignment source, which ideally fully illuminates the telescope aperture with a

Optic	Label	Focal Length (mm)	Diameter (mm)	Location (mm)
Melles Griot 01LAL413/078	L1	50	20	46.339
Thor Labs MLA150-5C	LA	5.2	0.146	105.07
Melles Griot 01LAO018/078	L2	25	8	138.31
Melles Griot 01LAO018/078	L3	65	25	230.41
Vision Research Phantom V7.3	CCD	n/a	n/a	283.24

Table 1. Specifications of the HTS optical bench outlined in Figure 15.

perfectly collimated or spherical wave. The Hartmann sensor has a minimum focal distance of around 50 m, which limits the acceptable curvature of incident light entering the telescope. Any misalignment in the optical bench will produce aberrated subimages on the CCD and be detrimental to estimation of turbulence parameters. Table 1 (adapted from Mann et al. [1]) outlines the HTS optics in further detail in reference to Figure 15.

The inner HTS optics ensure the cells behind each subaperture are large enough to prevent light from neighboring points to overflow but small enough to keep the computation time of the centroiding algorithm to a minimum [39]. A mask is applied to the subapertures that receive little to no light either due to the telescope aperture or its 4.8" diameter central obscuration [1, 40]. This reduces the total active regions from 1,936 to 1,258. Additional subapertures may also be removed for individual data sets if they are distorted or not focused correctly. The large number of subapertures in use allows for quick and accurate estimates of turbulence parameters, making it an ideal wavefront sensor for an AO system.

Sonic Anemometers.

Four Applied Technologies SATI/3A ultrasonic anemometers were used for point measurements of C_n^2 at 100 m increments along the path. This model was chosen for its three non-orthogonal axes of wind velocity (U, V, and W) measurement. The design is optimal for measuring high speed wind and attempts to minimize the flow distortion by the transducers [41]. The arms holding the anemometers were also pointed due west (the direction of prevailing wind) to minimize flow distortion from the arm. A pair of transducers are mounted in each axis separated by 15 cm [42]. The design of the anemometer is shown in Figure 16.

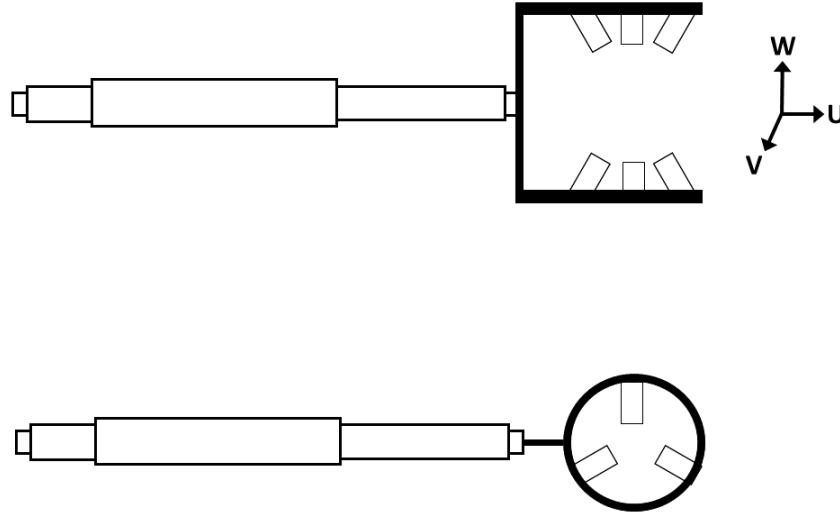


Figure 16. SATI/3A ultrasonic anemometer non-orthogonal design with 120° separation between transducers. The U,V,W axes refer to the upper orientation of the anemometer.

A sonic pulse is emitted by one of the transducers and captured by its opposing transducer and vice versa [41]. The transit time of the signal between the transducers is then calculated by

$$t = D \frac{\sqrt{c^2 - v_n^2} \pm v_d}{c^2 + v^2}, \quad (74)$$

where D is the path length, c is the velocity of sound in still air, v is the absolute velocity, and v_n and v_d are the normal and parallel components of velocity, respectively [42]. The parallel component is found by

$$v_d = \frac{D}{2} \left(\frac{1}{t_1} - \frac{1}{t_2} \right), \quad (75)$$

where t_1 and t_2 are the transit times of the two opposing pulse directions [42].

From the sound velocity measurements, the anemometers can be used to obtain sonic temperature information. The temperature structure parameter, C_T^2 , is obtained from the temperature measurements using

$$C_T^2 = \langle [T'(t + \Delta t) - T'(t)]^2 \rangle (\langle V \rangle \Delta t)^{-2/3}. \quad (76)$$

T' is the temperature flux that comes directly from anemometer measurements of temperature, where $T' = T - \langle T \rangle$ [43]. $\langle \rangle$ represents ensemble averaging, V is the magnitude of the mean wind velocity vector, and Δt is the time between measurements. The anemometers were operated at a 10 Hz collection rate ($\Delta t = 0.1$ s) and over a 1 minute collection period. From Equation 37, C_n^2 can then be calculated using C_T^2 by

$$C_n^2 = (79.2 \cdot 10^{-6} \frac{\bar{P}}{\bar{T}^2})^2 \cdot C_T^2, \quad (77)$$

where the overbar represents a mean averaging, P is the pressure [16]. The SATI/3A anemometers collect data at 200 Hz and output averaged data sets at 10 Hz. The 1-minute averaged data sets for 25 and 26 July are shown in Figure 17.

Figure 17 shows an interesting phenomenon that occurs following sunset. The 30 minute time span following sunset is a quiescent period during which atmospheric heating by the sun rapidly fades. During this time, the atmosphere settles into a horizontally layered structure. At the beginning of the quiescent period when the

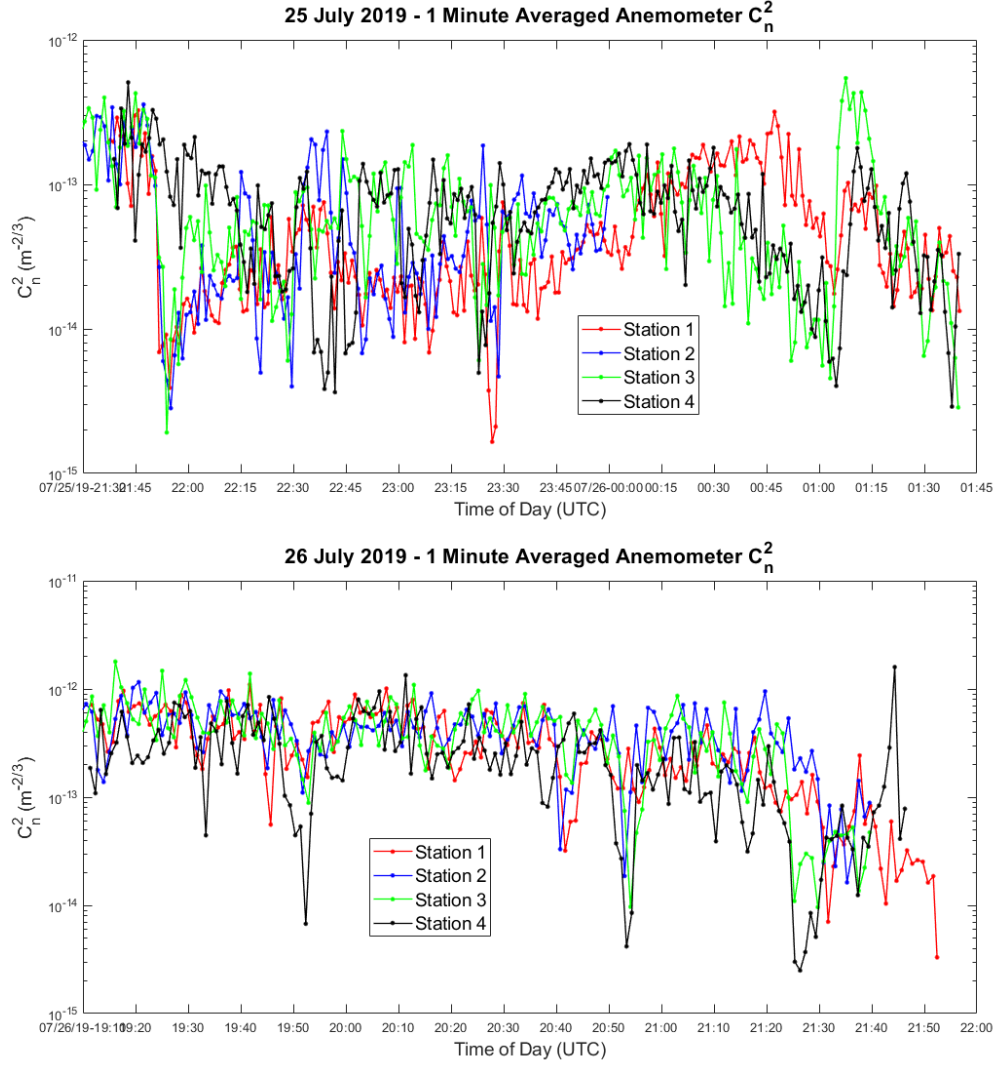


Figure 17. 1-minute averaged C_n^2 plots derived from sonic anemometer measurements taken during the early evening on the 25th and the late afternoon on the 26th. Station 1 is on the HTS side of the path and station 4 is on the source end. As observed, station 2 lost power around 00:00 UTC during collection on the 25th.

ground heating by the sun starts to weaken, the grass portions of the path cool faster than the concrete segments. The convective movement in the atmosphere throughout this period produces a counterintuitive rise in C_n^2 measurements as well as an increase in measurement noise. This can be observed in the 25 July subplot of Figure 17, where the anemometer stations over grass show a clear increase in C_n^2 following sunset at 0055 UTC. However, the functioning anemometer station over concrete did not see

this sharp C_n^2 increase but rather the slow decline one would expect. This effect can be explained by the temperature stratification over grass that is not present over the concrete, which gives rise to greater convective motion leading to an increase in C_T^2 and in turn, larger C_n^2 values measured by the anemometer stations.

The anemometer stations at both ends of the path also powered a Campbell Scientific NR-LITE2-L net radiometer to measure the difference between incoming versus outgoing (ground-reflected) solar radiation. For this work, the net radiometers were used to keep a record of cloud coverage. The radiometer plots are shown in Figure 18 with clear dips indicating clouds passing overhead. Station 1 on 26 July is consistently higher than station 4 throughout the day likely due to reflections from nearby surfaces that factor into net irradiance measurements. This did not affect results because the radiometer readings were only used to capture cloud coverage. The 25 July plot shows a deviation in measurements between the two stations following sunset at 0055 UTC. Negative net radiometer values indicate more outgoing irradiance relative to incoming. Past sunset, the radiometer located over concrete recorded greater outgoing radiation. This indicates the grass cools much more quickly following sunset.

Boundary Layer Scintillometer (BLS).

Scintillometers operate by sensing the intensity fluctuations of light (i.e. scintillation) caused by optical turbulence. By measuring the covariance of intensity fluctuations over the path, scintillometers can produce singular path-integrated values of C_n^2 and thus act as a reliable calibration tool in comparing the HTS against the constant turbulence case. The BLS generates a path-integrated value of C_n^2 by

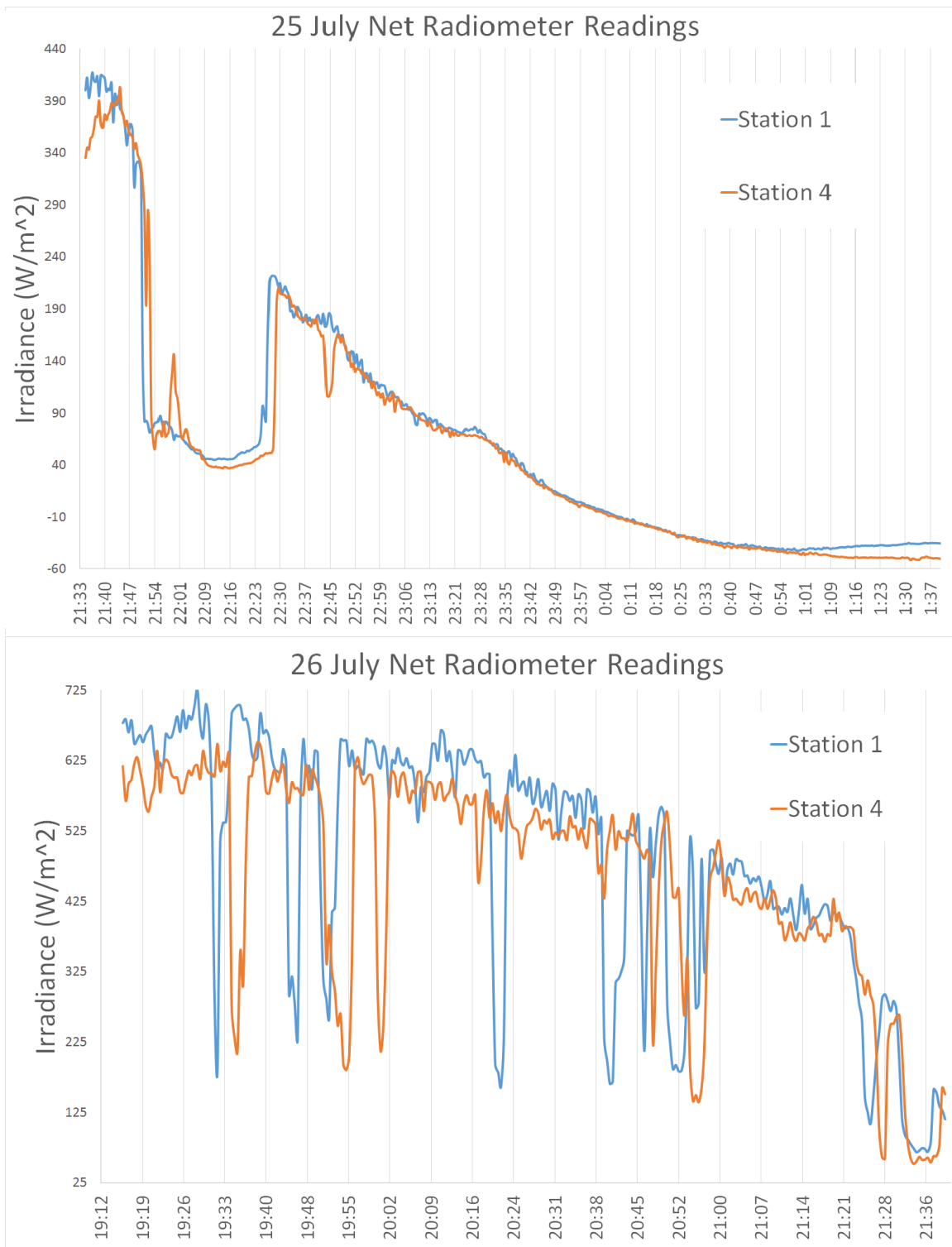


Figure 18. Net radiometer plots to display cloud coverage at times in UTC on 25 and 26 July. Station 1 is the anemometer tower closest to the HTS (100 m) and station 4 is on the opposite end of the path (400 m).

the log-amplitude variance, B_{11} , where

$$B_{11} = 4\pi^2 k^2 \int_0^\infty \kappa \Phi_n(\kappa) d\kappa \int_0^R dx \sin^2 \left(\frac{\kappa^2 x (R-x)}{2kR} \right) \left[2 \frac{J_1 \left(\frac{\kappa D_r x}{2R} \right)}{\frac{\kappa D_r x}{2R}} \right]^2 \left[2 \frac{J_1 \left(\frac{\kappa D_t (R-x)}{2R} \right)}{\frac{\kappa D_t (R-x)}{2R}} \right]^2, \quad (78)$$

where k is the optical wavenumber, κ is the spatial wavenumber, $\Phi_n(\kappa)$ is the three-dimensional refractive index spectrum, J_1 is a Bessel function of the first kind, D_r is the receiver diameter and D_t is the transmitter diameter. The path weighting function is center-weighted as shown in Figure 19.

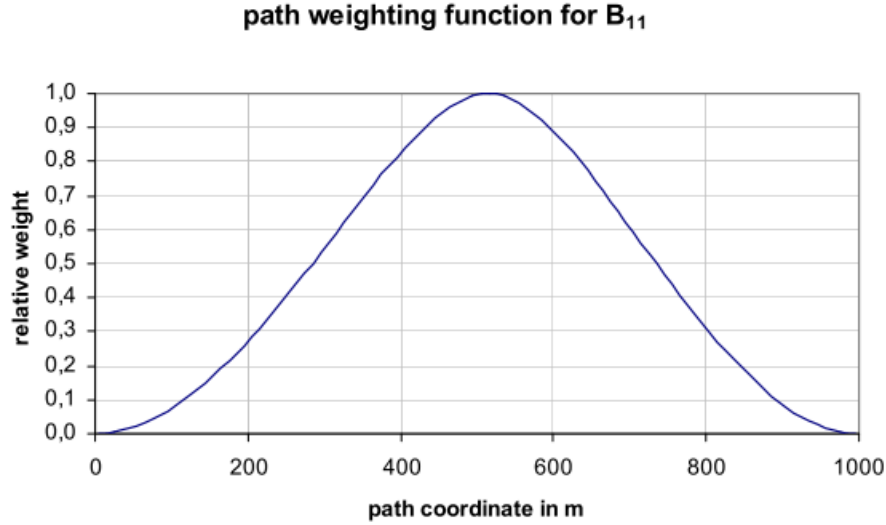


Figure 19. The path-weighting function used by the BLS to determine a singular C_n^2 estimate over the path from a point source [44]. The function is weighted heaviest in the center of the path.

The Scintec BLS900 was deployed along the path for measurements of C_n^2 as another method of validating the HTS estimates. The BLS transmitter contains 888 infrared (880 nm) LEDs [45] that are viewed by the receiver at the other end of the path (511m separation). Because 880 nm and 632.8 nm wavelengths are affected

differently by refractive index fluctuations, a conversion is applied to the BLS values to account for the difference thus making the BLS and HTS C_n^2 estimates comparable. For this experiment, the BLS transmitter was 1.3 m from the ground and the receiver, which was mounted in the remote sensing trailer, was 2 m from the ground. This height difference was accounted for in the calculation of C_n^2 from the BLS. The path reduction aperture was removed from the receiver, allowing it to correctly operate over the 511 m path [45]. The BLS produced a single averaged C_n^2 value over the path every minute during data collection displayed in Figure 20. This value can be multiplied by the impulse response matrix generated by HTS measurements to represent a profile under constant turbulence conditions.

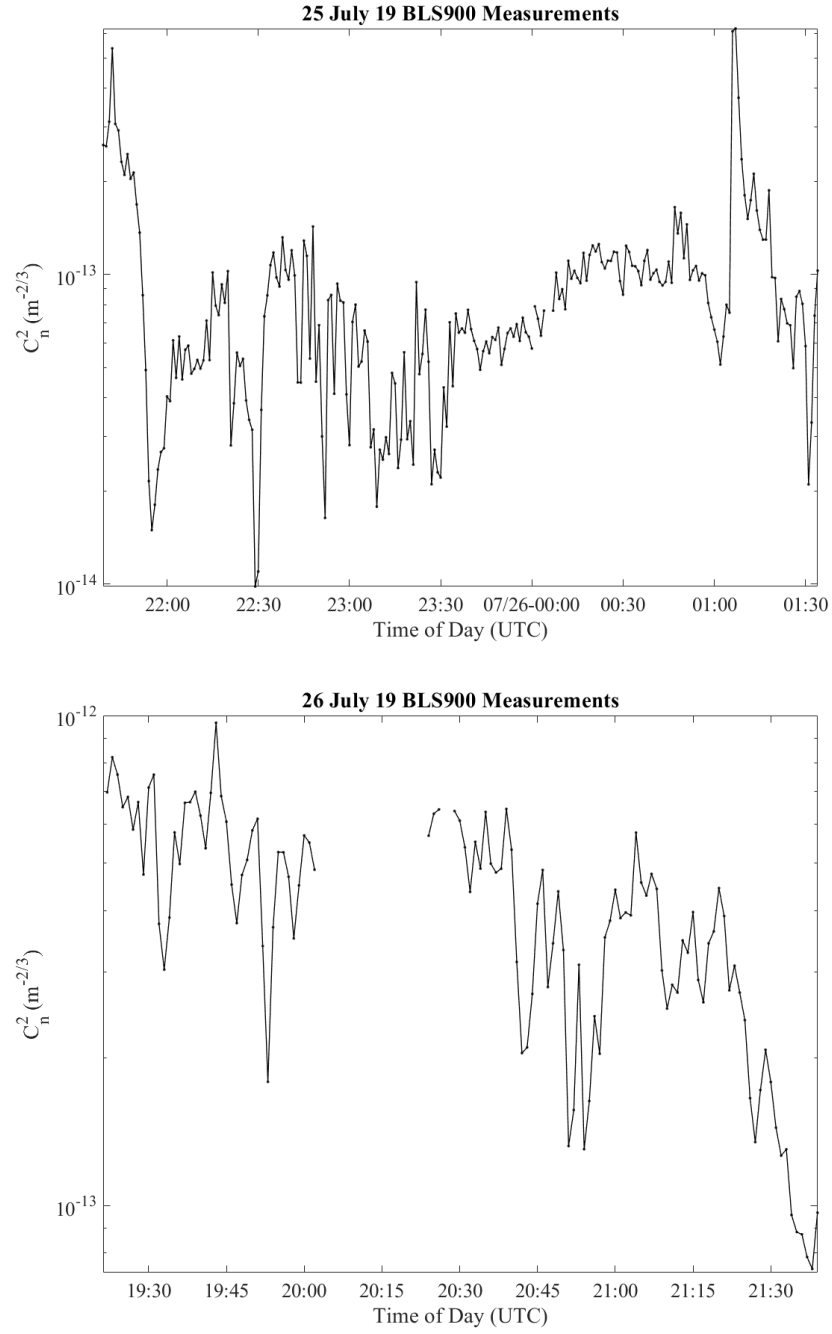


Figure 20. BLS center-weighted C_n^2 path measurements from 25 July and 26 July. No measurements were made from 2003-2023 UTC on 26 July likely because the path from the BLS transmitter to receiver was blocked.

3.3 Methodology

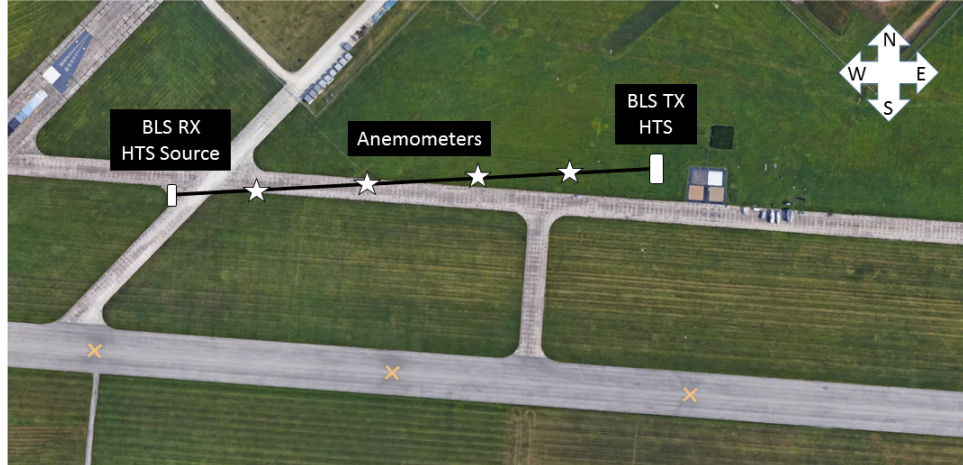


Figure 21. 511 m path oriented in the direction of the prevailing wind (west) with anemometers distributed across. The remote sensing trailer containing the BLS receiver and HeNe lasers is on the left. The HTS trailer containing the HTS and the BLS source is on the right.

The HTS profiled the 511 m path depicted in Figure 21 located on the taxiway of the National Museum of the US Air Force in Riverside, Ohio. The first half of the path is almost entirely grass and the second half is concrete. This inhomogeneous path was chosen to observe the difference of turbulence strength over the two types of ground. However, the concrete on the taxiway has greatly deteriorated, meaning it may not generate as much turbulence from surface heating as it would if it were properly maintained. This weakens the inhomogeneity from grass to concrete. Therefore, the difference observed between concrete and grass turbulence in this experiment is lessened but still observable in some profiles. Four sonic anemometers were mounted 2.64 m from the ground and placed at points along the path 100 m, 200 m, 300 m, and 400 m from the HTS. The anemometers height difference from the HTS sensing

path was corrected based on the $h^{-4/3}$ conversion factor. The averaging algorithm used by the anemometers when estimating C_T^2 contained issues that were corrected by multiplying by a factor of 1.89. The derivation to obtain this value is given in Appendix A. Previous experiments [46] have determined a potential correlation between the direction of the turbulence anisotropy and the wind direction relative to the path. For this reason, the path was chosen to face west into the direction of the prevailing wind such that wind will primarily push the turbulence structure along the path rather than transverse to the path. The anemometers at each end logged wind velocity and air temperature data using a Raspberry Pi microprocessor, while the center stations use Campbell Scientific CR6 dataloggers. The two HeNe laser beacons were located within the remote sensing trailer and separated by 11 cm. This 11 cm separation ensured the laser subimages were each focused into the center of their 13×13 pixel regions.

HTS data was captured on 25 July from 1744 to 2133 and on 26 July from 1615 to 1734 (all EST, UTC-4). Each individual set of data contains 100 frames of background data and 1,000 frames under laser illumination. The Phantom camera captures 600×800 pixel frames, which are later cropped to 572×572 pixels for processing. The camera was operated at $2 \mu\text{s}$ exposure to prevent over-saturation during periods of low turbulence and to capture the quickly varying temporal statistics.

The data from the HTS was first collected using National Instruments'® LabVIEW software and later processed in MATLAB®. LabVIEW logs each set of HTS data as a big endian file with two additional marker bits at the beginning of each file. These bits are removed when using MATLAB to read in the data. The mean of the 100 background frames was computed and subtracted from each of the 1,000 laser frames. A mask was then applied to each data frame in order to cover the subapertures receiving little to no light either due to the telescope aperture or the central

obscuration. The mask was applied in such a way that the first box in each row contains light from the laser on the right (from the perspective of the HTS looking into the remote sensing trailer). To make sure the spots on the CCD were ordered properly, two sets of data were captured with the laser beacons operating individually before each set of simultaneous operation. Then, by comparing spot locations, the two lasers could be distinguished. This ensures the tilt variances are calculated properly. Some sets of data, especially those taken during periods of fluctuating temperature, contained subaperture pairs that are blurred or cut off due to incorrect focusing. The telescope focus drifts due to thermal expansion and contraction of the HTS optics and must be corrected constantly. In these cases, the flawed subapertures were covered and therefore removed from calculations. This did not significantly affect the results for the individual data sets because of the large population of subapertures factoring into calculations.

Following the mask application, an auto-focusing algorithm is performed, which corrects for any shifting focus and moves each centroid to the center of its region. The auto-focus code first finds the center of each region not covered by the mask (i.e. regions where the mask has a value of 1). Then, it finds the location of the centroid within every cell in the mean frame, which is the average of all 1,000 frames. An 11×11 pixel box is then drawn around each centroid and moved to the center of its respective cell. If the turbulent conditions are weak enough, a 13×13 pixel box may be used instead. For more turbulent data sets, this method fails because the local tilts are large enough to move the spots outside of their respective 13×13 pixel region, which affects the mean image and hence subsequent focus correction.

20% of the maximum value within each cell is subtracted from each pixel in the cell in an attempt to remove the noise pedestal. A raw set of tilt variance measurements and the corresponding auto-focused data frame with the background subtracted are

shown in Figure 22.

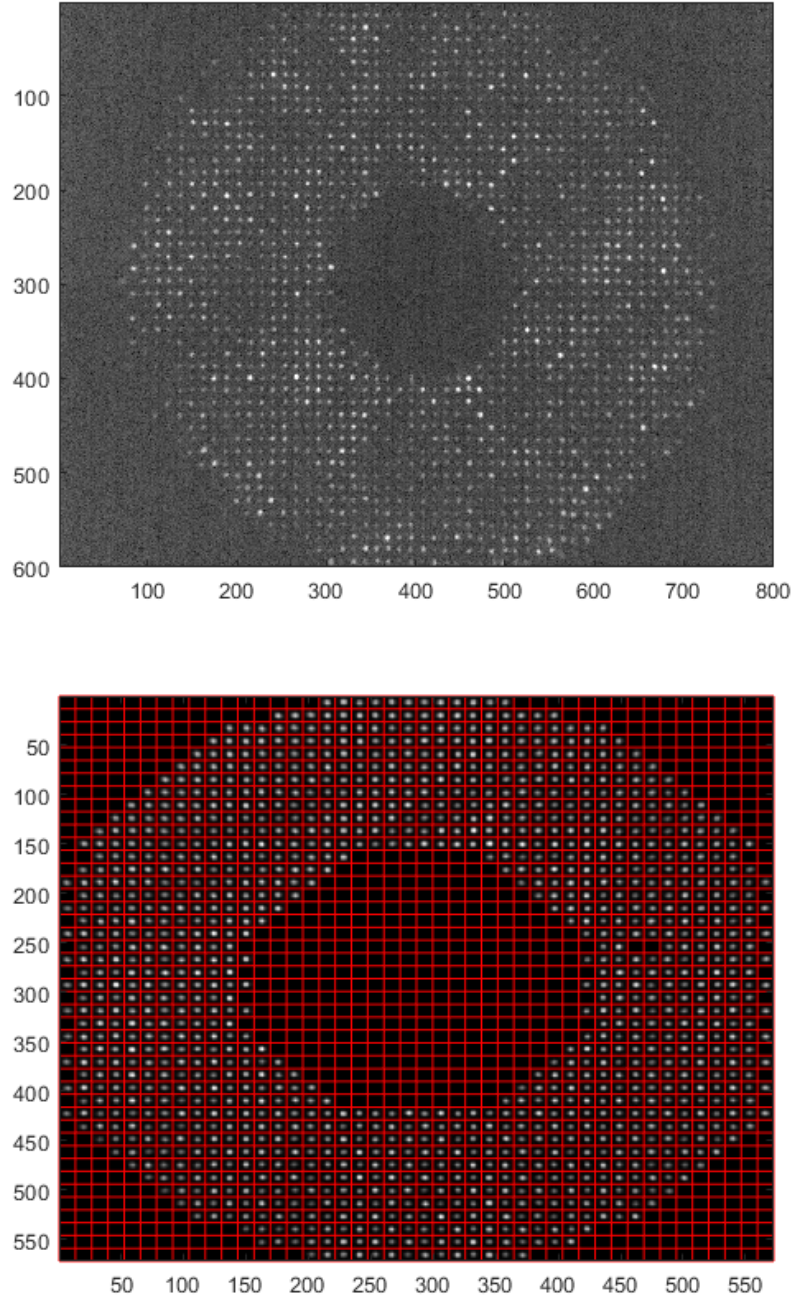


Figure 22. Example of a raw 600 x 800 HTS data frame against an averaged cropped frame with the correct mask applied, auto-focused, and the background subtracted. Additional flawed subapertures are also covered. 13 x 13 pixel red boxes are drawn around each spot to ensure the correct focusing.

At this point, the centroids of each spot for all 1,000 focus-corrected frames are calculated to track their movements over the period of data collection. This allows for the differential and non-crossing differential tilt variances to be determined. The Fried coherence length in the horizontal and vertical axes is also found from the centroid information. The mean variance over each subaperture in the longitudinal and transverse direction is first calculated. The components of r_0 are then

$$r_0^{L,T} = \frac{V_{L,T}}{K_{L,T}\lambda^2 D^{-1/3}}^{-3/5}, \quad (79)$$

where λ is the wavelength, $V_{L,T}$ is the set of tilt variances in the longitudinal and transverse direction, D is the subaperture diameter (1.15 cm), and

$$K_L = 0.364 \left(1 - 0.532 \cdot \left(\sqrt{2} \frac{150}{146} \right)^{-1/3} - 0.024 \left(\sqrt{2} \frac{150}{146} \right)^{-7/3} \right) \quad (80)$$

$$K_T = 0.364 \left(1 - 0.798 \cdot \left(\sqrt{2} \frac{150}{146} \right)^{-1/3} + 0.018 \left(\sqrt{2} \frac{150}{146} \right)^{-7/3} \right), \quad (81)$$

where 150 μm is the subaperture separation and 146 μm is the lenslet diameter and the $\sqrt{2}$ is from the 45° mask rotation. This produces four r_0 values in total: V_L , V_T , H_L , H_T , where L denotes longitudinal (parallel to separation axis), T denotes transverse (perpendicular to separation axis), V is vertical, and H is horizontal.

Through trial and error, a set of weighting functions was chosen specifically for the greatest diversity, range, and noise suppression possible. This set turned out to be all of the crossing weighting functions differenced by their nearest neighbor combined with the first five and final non-crossing weighting function. Differencing the crossing functions eliminates knowledge of the functions' magnitude. The addition of the non-crossing functions reintroduces the DC component. This combination produces an ideal delta-like influence function from 0 m to 350 m (before applying a pseudoinverse

threshold). Beyond 350 m, the weighting functions are very similar and hence the present technique fails to profile past this point. The differencing technique successfully reduced noise between neighboring subapertures. The weighting functions used to generate the profiles for this thesis are displayed in Figure 23.

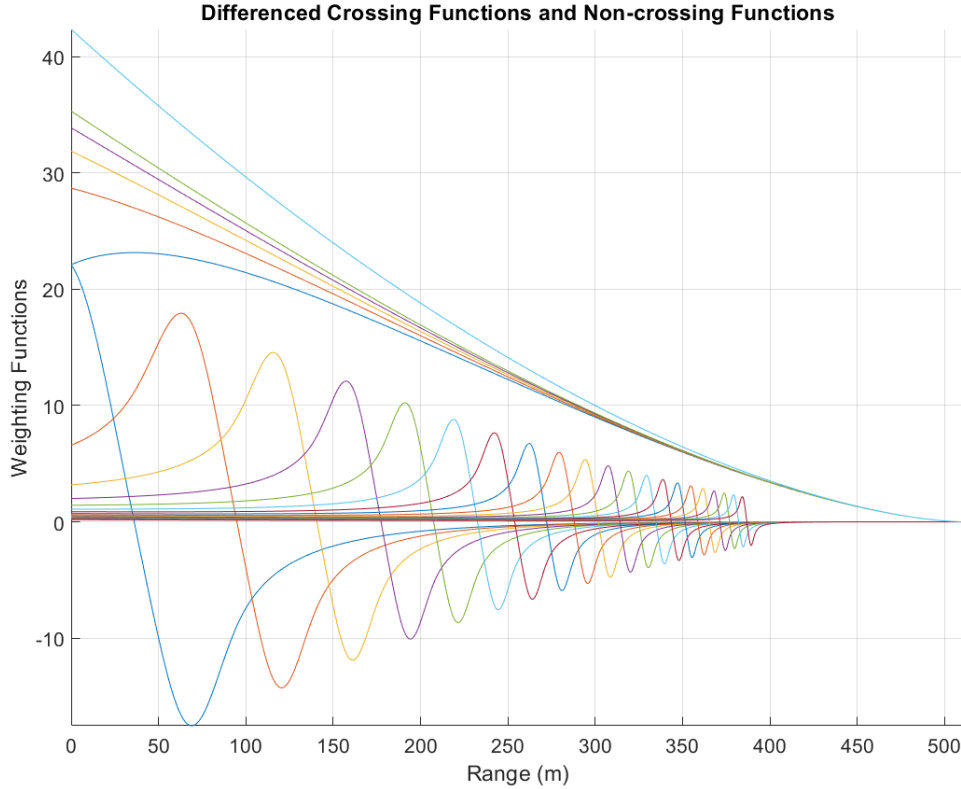


Figure 23. The combination of weighting functions used in data processing for this work. The differenced crossing weighting functions contain notches at varying points along the path whereas the non-crossing functions have notches behind the apertures (not shown).

Finally, the thresholded pseudoinverse of the weighting functions is multiplied to the set of tilt variances along with a factor of 2 (from the inverse of the step size) to give C_n^2 estimates along the path. C_n^2 values from the HTS, BLS, and anemometers are then plotted on a logarithmic axis against path distance, z . The non-linear optimizer is applied with constraints specific to each profile to minimize measurement error in the profile.

IV. Results

Experimental results are displayed and explained in this chapter. Each of the turbulence profiles presented contains four different sets of data: C_n^2 point measurements derived from the anemometer collections, the single BLS C_n^2 reconstructed with the influence function to represent a constant turbulence profile, the raw pseudoinverse profile from the HTS measurements, and the optimized HTS profile. The pseudoinverse threshold values determine the lower limit below which all singular values of \mathbf{M} are not inverted. To better quantify these values, they will be given in terms of the percentage

$$\alpha = \frac{\textit{Threshold}}{\textit{Largest Singular Value}} \times 100\%. \quad (82)$$

For the chosen combination of weighting functions, the largest singular value is 1,350. The optimizer effectively flattens the small-scale and non-physical C_n^2 fluctuations in each profile that arise from measurement noise. Various combinations of weighting functions were tested in order to find the set with the largest functional range and to minimize the noise statistics. The influence function produced by the chosen set of weighting functions is only reliable to 350 m at most. Therefore, none of the following profiles display reliable data past 350 m. r_0 estimates for each data set are also presented.

Each of the following profiles are presented in UTC (4 hours ahead of local time in the summer). The profiles are ordered chronologically, beginning at 2200 UTC on 25 July 2019 and ending at 2134 UTC on 26 July 2019. C_n^2 is plotted on a logarithmic axis so both large-scale and small-scale changes along the path are visible. Fluctuations in the reconstructed BLS profiles indicate the locations where fidelity in the profiles is lost.

Figures 24 and 25 were captured at 2200 and 2218 UTC, respectively. Despite being taken so closely in time, the two sets of data produced dissimilar results as expected due to the randomly varying statistics of turbulence. At 2200 UTC, the BLS measured a C_n^2 of $4.0\text{e-}14 \text{ m}^{-2/3}$, which is relatively low compared to other measurements. Weaker turbulence conditions led to less measurement noise, which allowed the pseudoinverse in this case to be performed with a threshold of 11 ($\alpha = 0.8\%$). At 2218 UTC, the BLS measurement of C_n^2 more than doubled from 2200 UTC at $9.3\text{e-}14 \text{ m}^{-2/3}$. Because of this, the threshold had to be raised to 31 ($\alpha = 2.3\%$) to beat the measurement noise and eliminate dropouts in the profile.

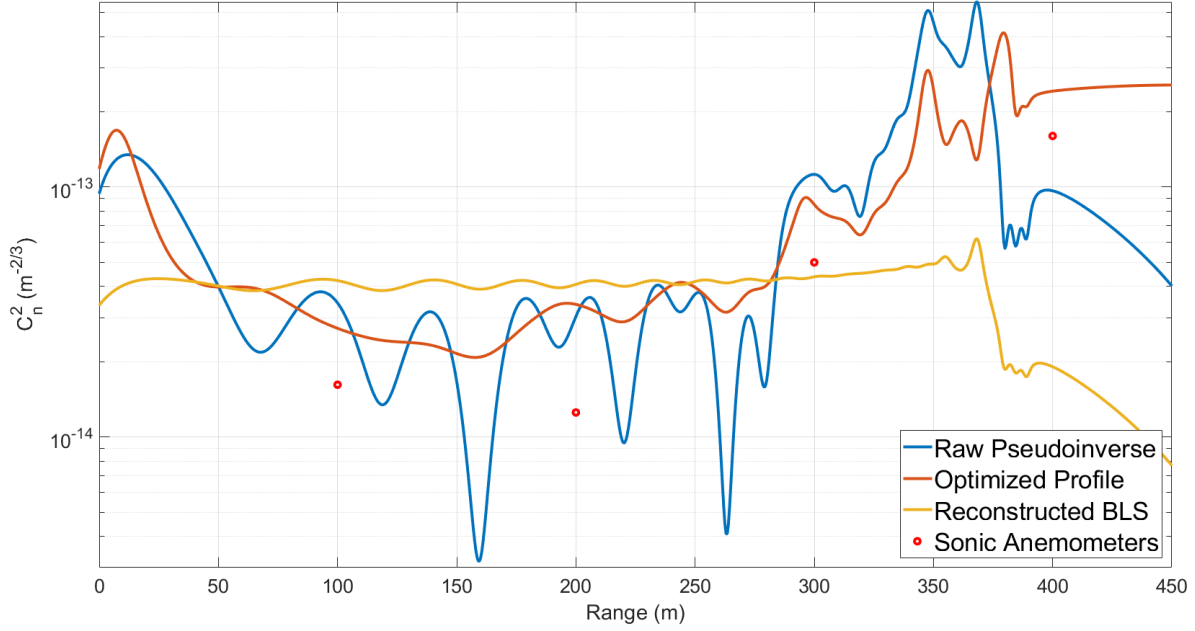


Figure 24. 25 July 2200 UTC turbulence profile with threshold of 11 ($\alpha = 0.8\%$) and BLS measured C_n^2 of $4.0\text{e-}14 \text{ m}^{-2/3}$.

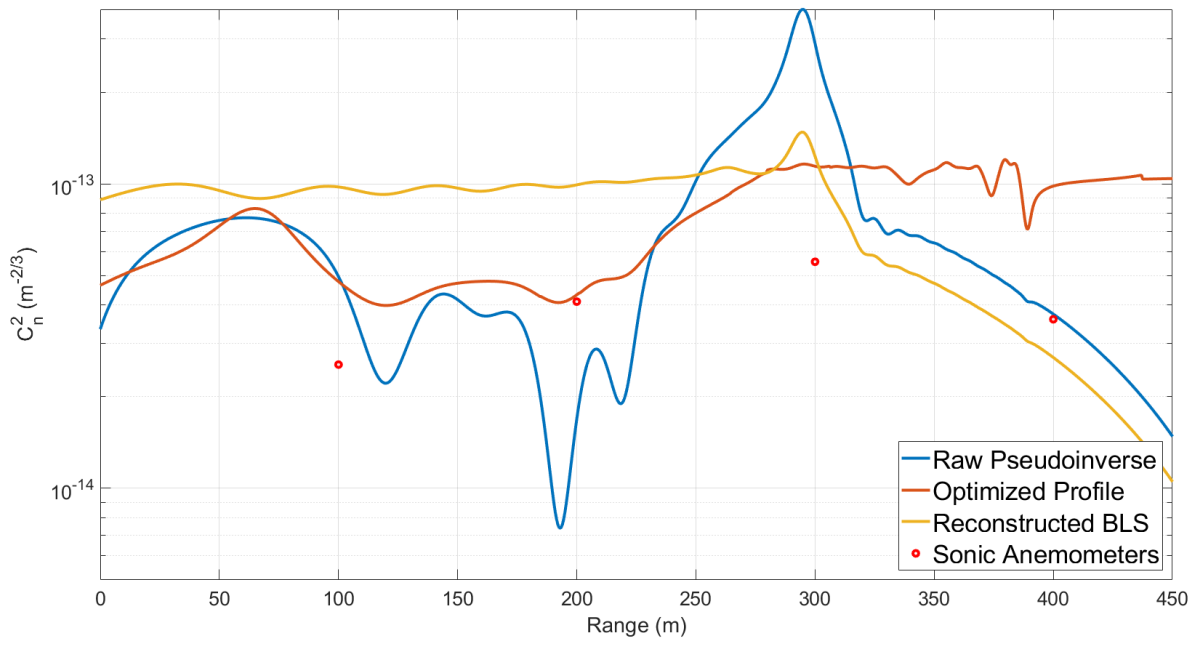


Figure 25. 25 July 2218 UTC turbulence profile with threshold of 31 ($\alpha = 2.3\%$) and BLS measured C_n^2 of $9.3\text{e-}14 \text{ m}^{-2/3}$.

The 2232 UTC data set from 25 July contained multiple blurred subapertures due to the drifting focus of the HTS optics. With these flawed subapertures removed, the optimized HTS profile matched the anemometers very well.

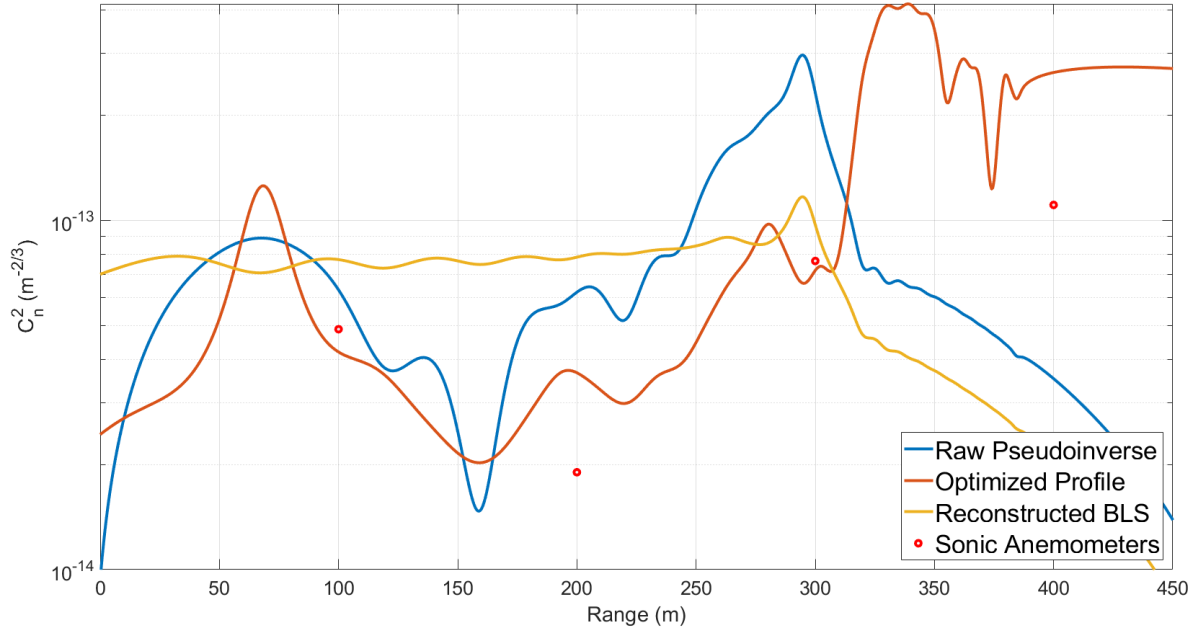


Figure 26. 25 July 2232 UTC turbulence profile with threshold of 26 ($\alpha = 1.9\%$) and BLS measured C_n^2 of $7.3\text{e-}14 \text{ m}^{-2/3}$.

The 2247 UTC data set in Figure 27 was captured during a period of strong turbulence. The BLS estimated C_n^2 values of $5.4\text{e-}14 \text{ m}^{-2/3}$ at 2247 UTC and $1.4\text{e-}13 \text{ m}^{-2/3}$ only a minute later indicating strong turbulence fluctuations at this time. This explains why the profile at this time still shows dropouts at a threshold of 31 ($\alpha = 2.3\%$).

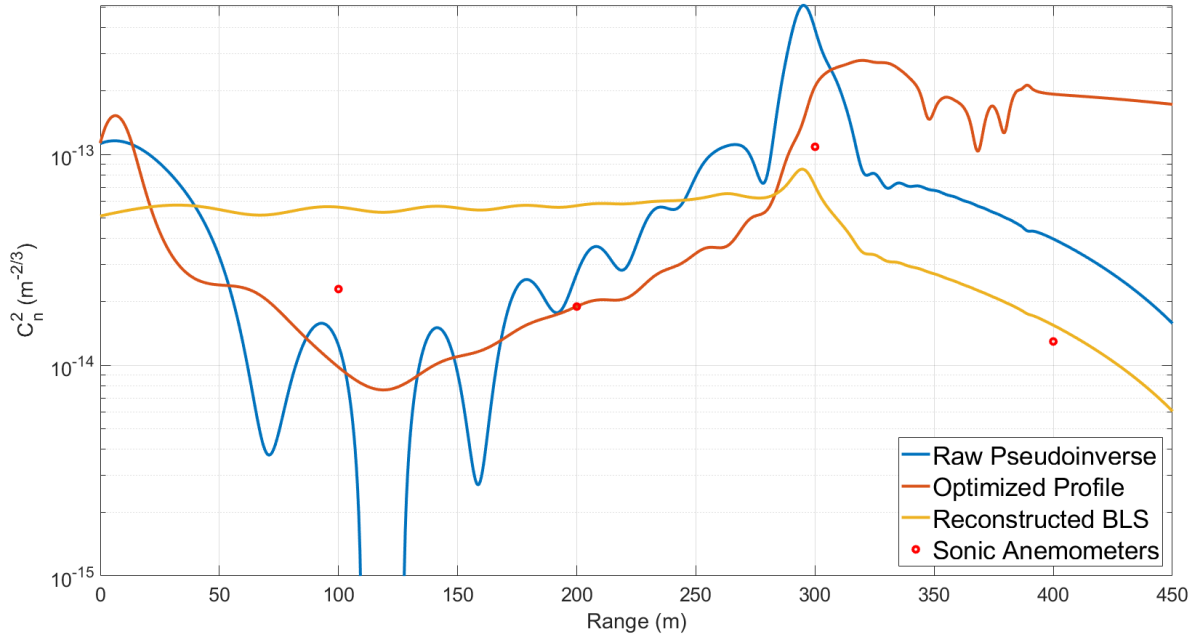


Figure 27. 25 July 2247 UTC turbulence profile with threshold of 31 ($\alpha = 2.3\%$) and BLS measured C_n^2 of $5.4\text{e-}14 \text{ m}^{-2/3}$.

Figure 28 was produced a large threshold value of 45 ($\alpha = 3.3\%$). This causes the influence function to fail faster than usual at 250 m. Even at such a large threshold, measurement noise during this data set is significant enough to produce negative values in the raw pseudoinverse near 75 m and 120 m.

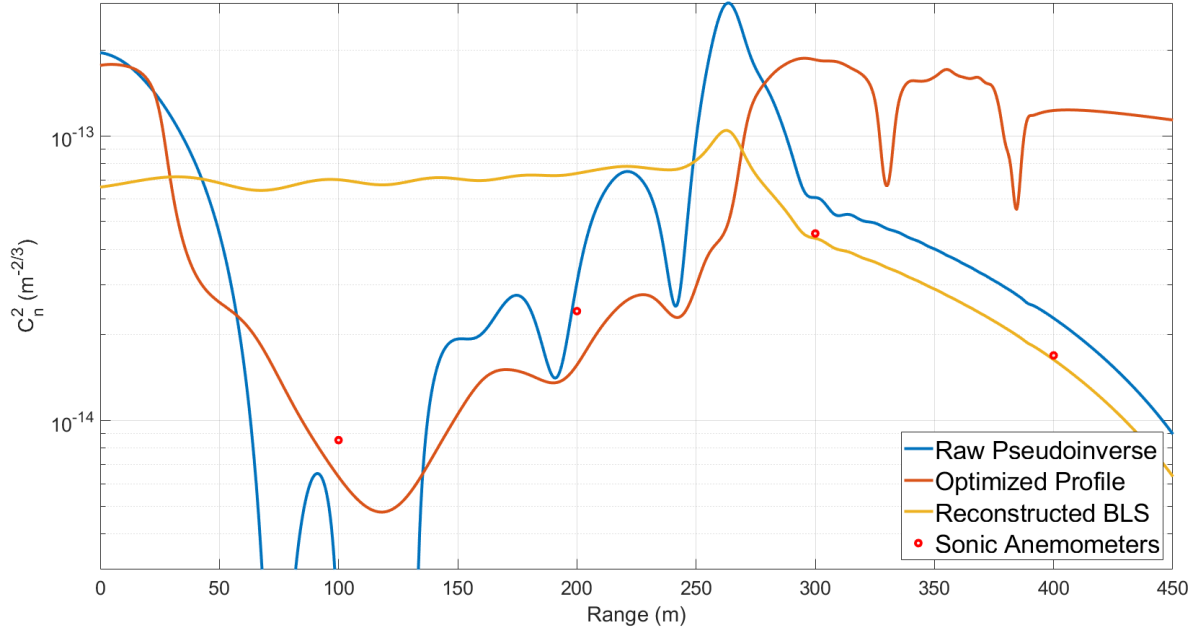


Figure 28. 25 July 2305 UTC turbulence profile with threshold of 45 ($\alpha = 3.3\%$) and BLS measured C_n^2 of $6.6\text{e-}14 \text{ m}^{-2/3}$.

A large threshold was also used in Figure 29 although dropouts are still present in the profile. As time approaches sunset, changes in the atmosphere contribute to additional measurement noise in the system. This effect is partly responsible for the increased dropouts in the 2320 UTC profile.

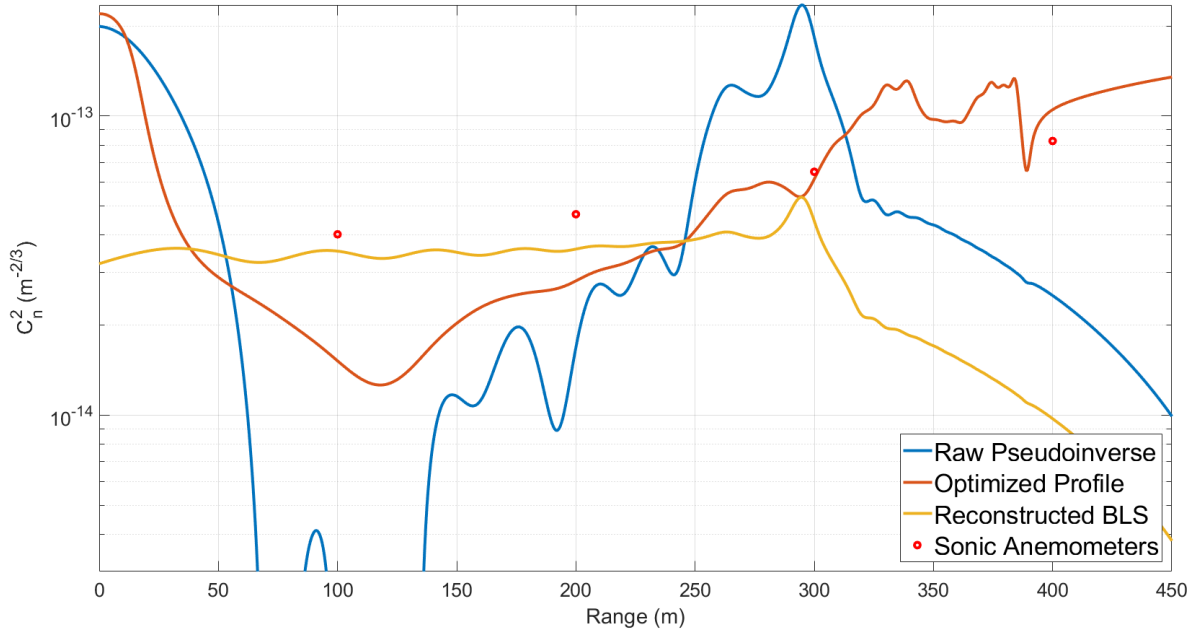


Figure 29. 25 July 2320 UTC turbulence profile with threshold of 31 ($\alpha = 2.3\%$) and BLS measured C_n^2 of $3.4\text{e-}14 \text{ m}^{-2/3}$.

Figure 30 shows an upward slope towards 300 m that does not agree with the anemometer at 300 m. This same trend is present in various other profiles and often disagrees with the anemometer measurements (e.g. Figures 25 and 33). This effect could be a result of measurement noise or the HTS may be seeing higher turbulence over the concrete portion of the path that the anemometers are missing.

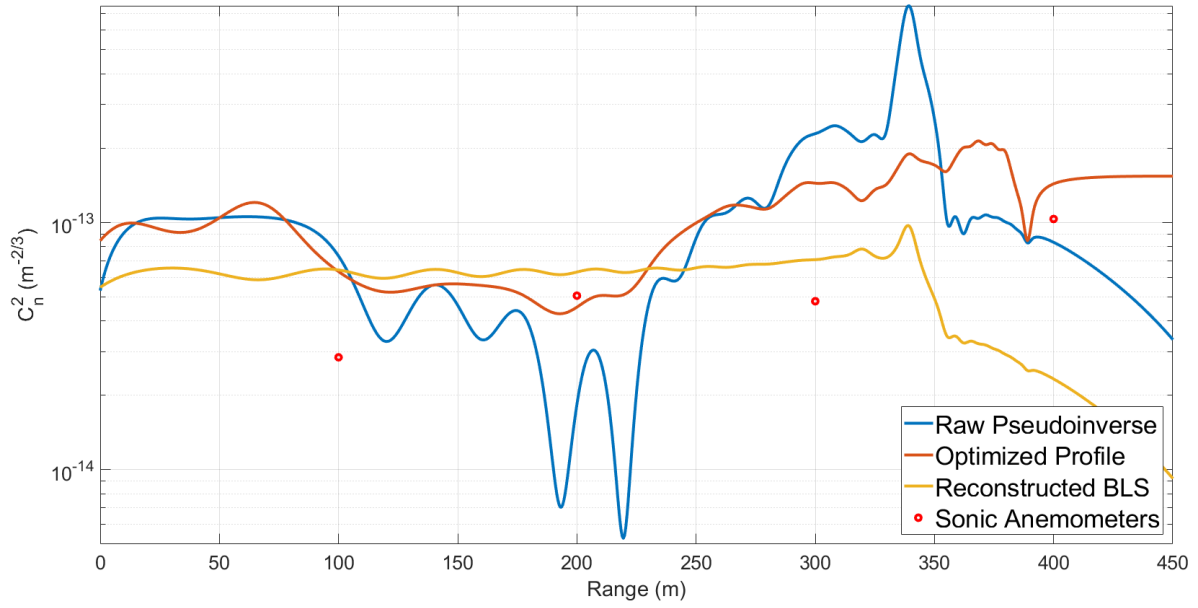


Figure 30. 25 July 2348 UTC turbulence profile with threshold of 18 ($\alpha = 1.3\%$) and BLS measured C_n^2 of $6.2\text{e-}14 \text{ m}^{-2/3}$.

Sunset on 25 July occurred at 0055 UTC (2055 local). The increase in turbulence strength and subsequent fall following sunset (due to the quiescent period) is observed in Figures 32 and 33, respectively. The anemometer station at 200 m lost power at 2359 UTC on 25 July and is therefore not shown in Figures 31, 32, and 33. The power was restored the next day for data collection.

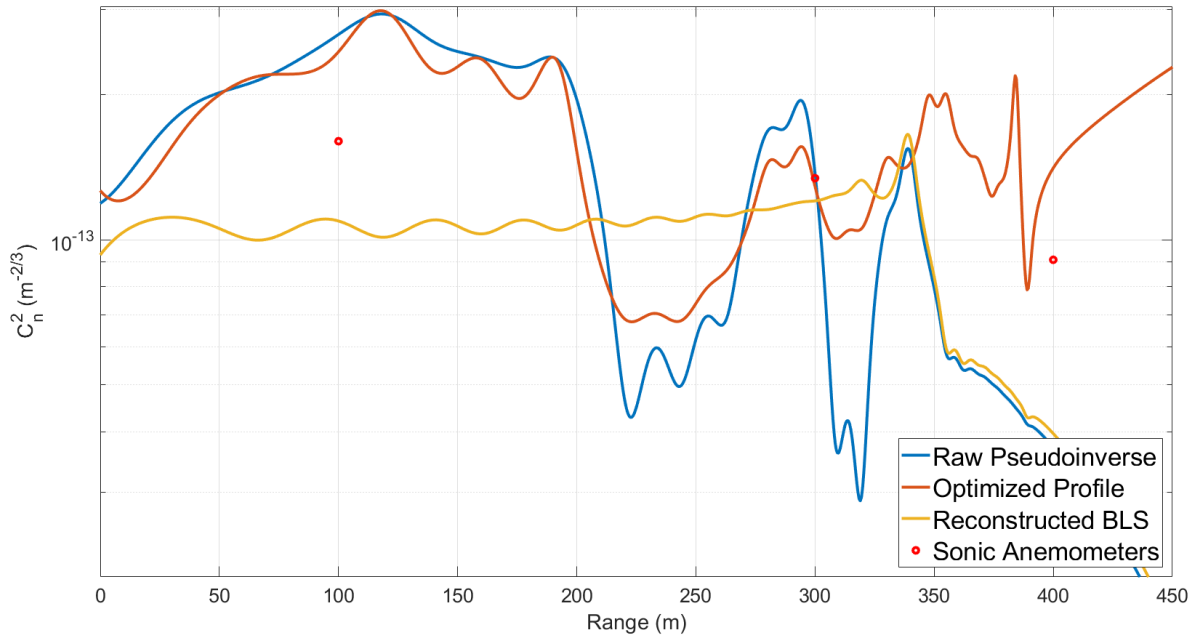


Figure 31. 25 July 0024 UTC turbulence profile with threshold of 18 ($\alpha = 1.3\%$) and BLS measured C_n^2 of $1.0\text{e-}13 \text{ m}^{-2/3}$.

A lower threshold was used in Figure 32 so the raw pseudoinverse would accurately profile the dip in C_n^2 at 300 m. The trade-off for this is the dropout that occurs near 290 m. The anemometers at this time recorded an order of magnitude difference in C_n^2 from 100 m to 300 m. This set of data was captured 8 minutes before sunset on 25 July. The difference in measurements can be attributed to the net radiometer readings in Figure 18, which shows a deviation in net irradiance following sunset.

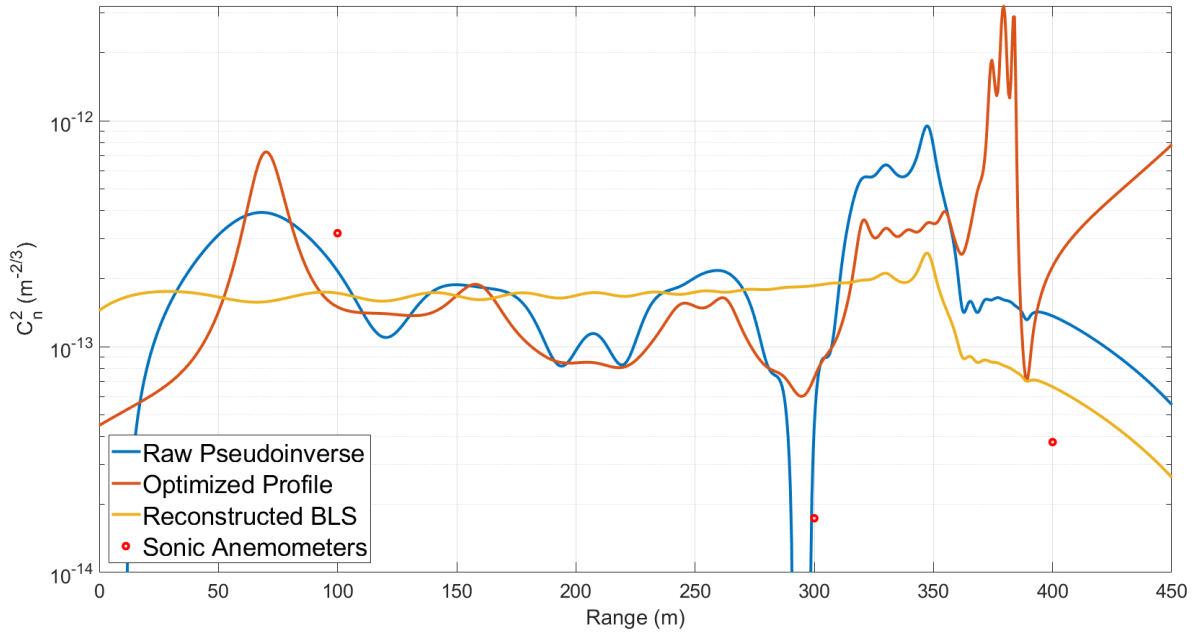


Figure 32. 25 July 0047 UTC turbulence profile with threshold of 15 ($\alpha = 1.1\%$) and BLS measured C_n^2 of $1.7\text{e-}13 \text{ m}^{-2/3}$.

Figure 33 was the first profile generated following sunset at 0055 UTC. At this time, the anemometers measured approximately constant turbulence over the path. The HTS estimate disagrees with the anemometers and shows an upward trend towards the end of the path. This trend and the C_n^2 dropout are likely due to the measurement noise produced as the atmosphere settles into layers following sunset.

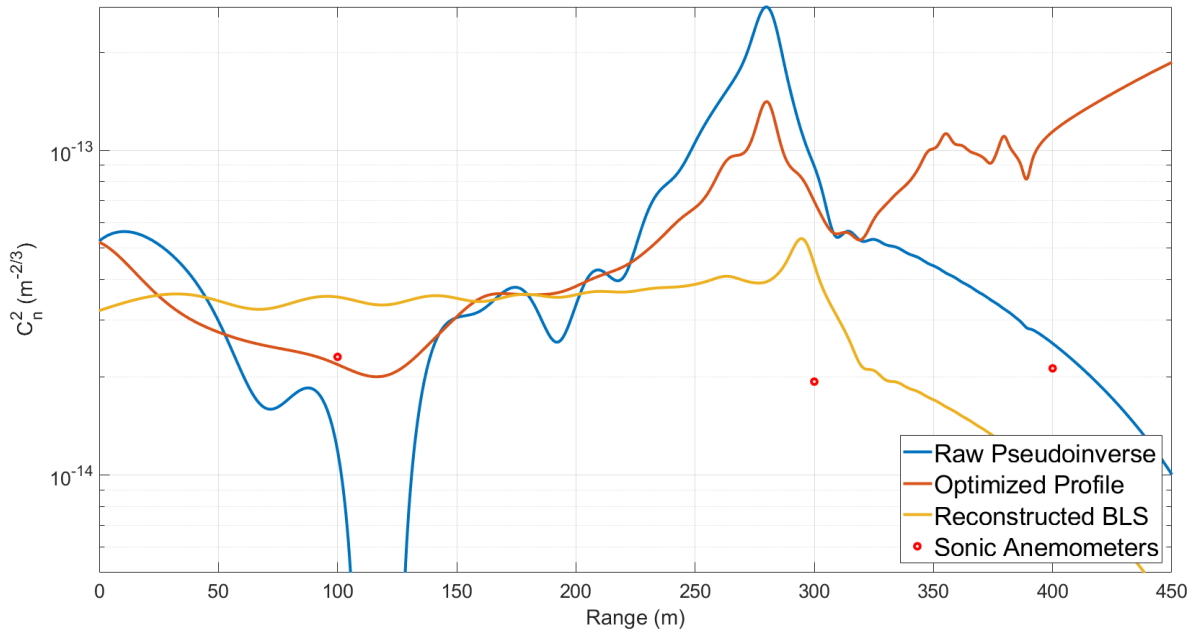


Figure 33. 25 July 0133 UTC turbulence profile with threshold of 31 ($\alpha = 2.3\%$) and BLS measured C_n^2 of $7.4\text{e-}14 \text{ m}^{-2/3}$.

The following data sets are all from 26 July. Many of the data sets from this day were either too defocused or too turbulent for data processing and are therefore not shown. The high turbulence of these sets caused the spots to move outside of their specified regions. At the moment, the HTS operating scheme and processing script cannot produce accurate profiles under strong turbulence conditions. This will be addressed in future work.

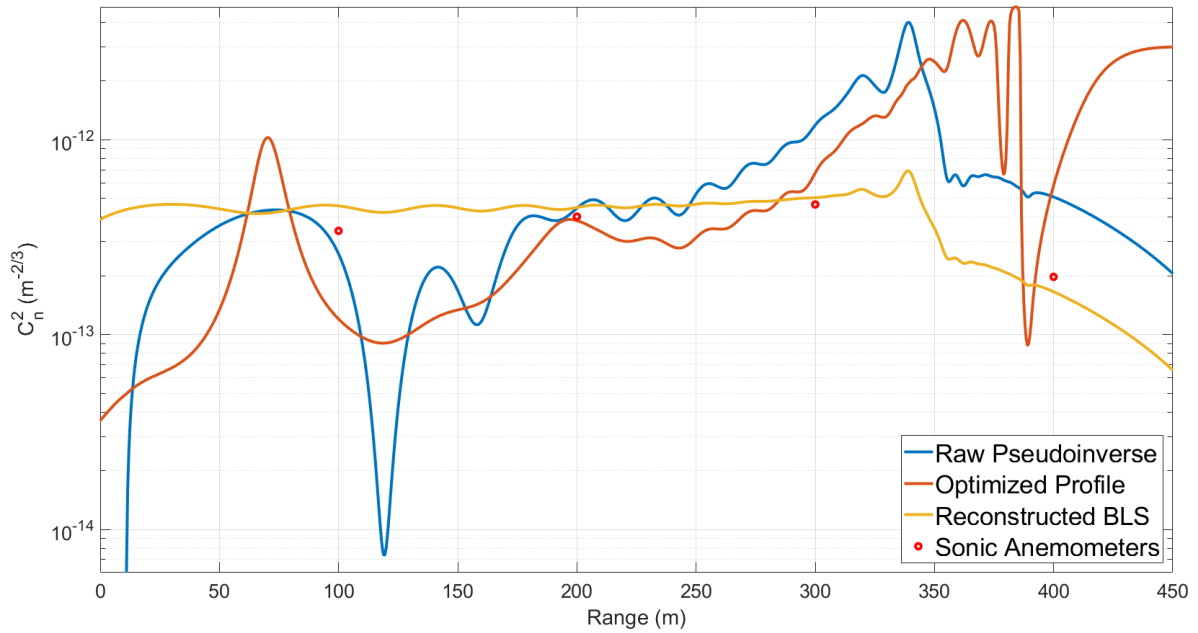


Figure 34. 26 July 2049 UTC turbulence profile with threshold of 31 ($\alpha = 2.3\%$) and BLS measured C_n^2 of $4.4\text{e-}13 \text{ m}^{-2/3}$.

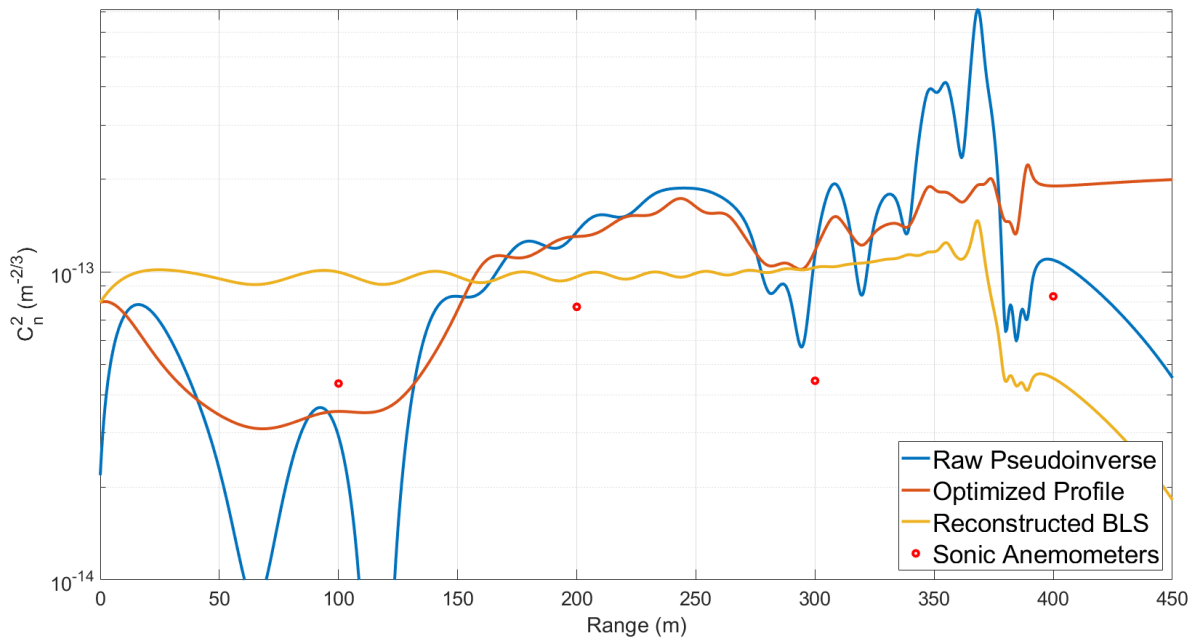


Figure 35. 26 July 2134 UTC turbulence profile with threshold of 11 ($\alpha = 0.8\%$) and BLS measured C_n^2 of $9.6\text{e-}14 \text{ m}^{-2/3}$.

4.1 Profiles Affected by Cloud Coverage

The two remaining profiles presented do not follow a common trend with the anemometer values and are displayed for the purpose of explaining the disagreement. The HTS data from 2120 UTC in Figure 36 did not correlate with the 1 minute averaged anemometer values because of the quickly shifting cloud coverage. The anemometers captured data during a period of overcast from a large cloud that was missed by the HTS. For this reason, 5-minute averaged anemometer values were added to Figure 36 in an attempt to minimize the effect of the overhead clouds.

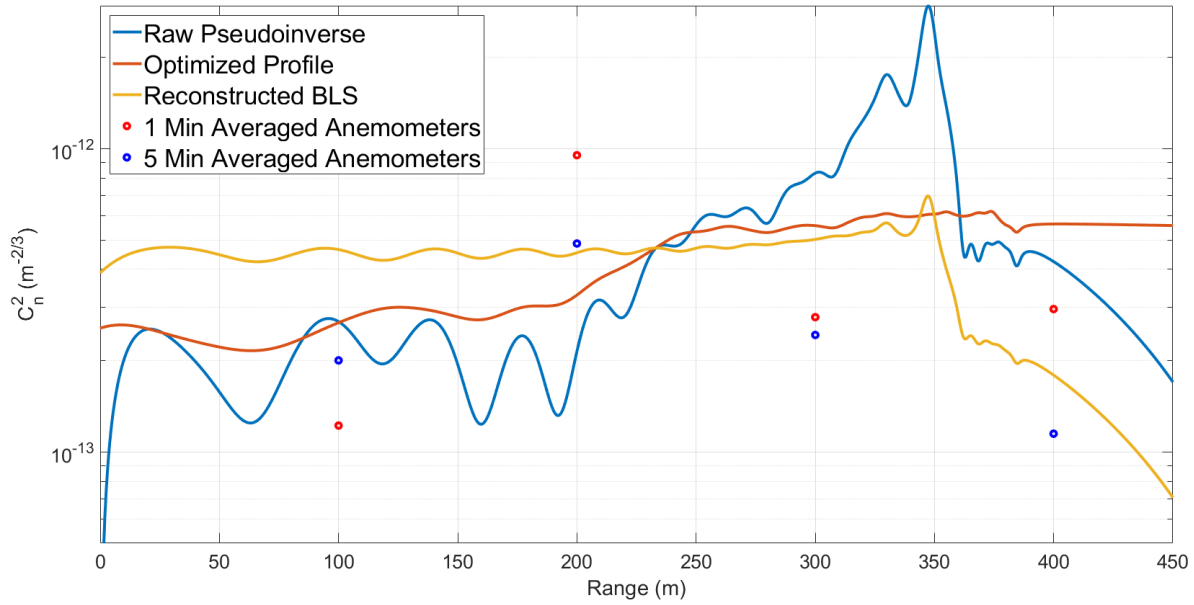


Figure 36. 26 July 2120 UTC turbulence profile with threshold of 15 ($\alpha = 1.1\%$) and BLS measured C_n^2 of $4.4\text{e-}13 \text{ m}^{-2/3}$.

Figure 37 shows a clear opposite trend between HTS and anemometer measurements. 26 July saw a sky full of large clouds, which is the explanation for the disagreement in this case. The anemometers averaged data over a 1 minute collection period while the HTS data captures only recorded a 10 second interval (1,000 frames at 100 fps). Figure 18 shows a cloud over anemometer station 4 (at the 400 m mark) at 2128 UTC. Over their longer capture period, the anemometers at 300 m and 400 m saw a dip in C_n^2 from the cloud that the HTS did not see.

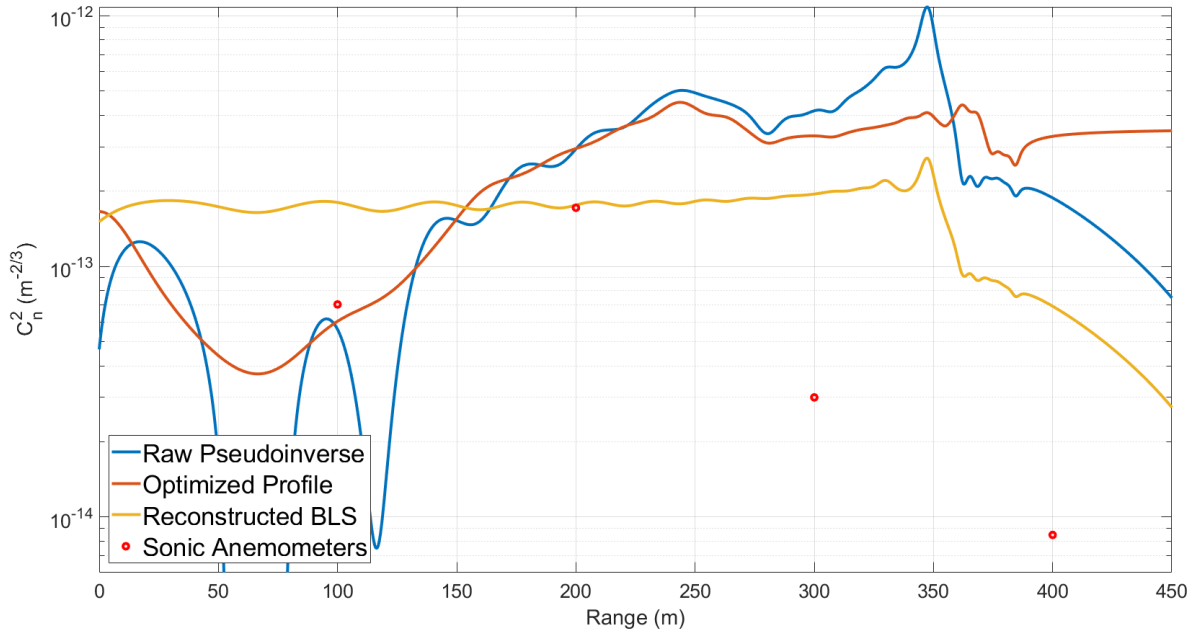


Figure 37. 26 July 2128 UTC turbulence profile with threshold of 15 ($\alpha = 1.1\%$) and BLS measured C_n^2 of $1.7\text{e-}13 \text{ m}^{-2/3}$.

4.2 Fried Parameter Estimates

An estimation of r_0 was also calculated from each data set. For each set, horizontal longitudinal and transverse as well as a vertical longitudinal and transverse r_0 components were calculated where longitudinal represents centroid motion parallel to the axis and transverse accounts for perpendicular centroid motions. Unequal longitudinal and transverse components suggest non-Kolmogorov turbulence. Dissimilar horizontal longitudinal and vertical longitudinal components (and transverse) also suggests anisotropy in the turbulence. The following table provides the derived r_0 values found by each set of tilt variances. The percent difference between the two axes is given as a measure of anisotropy.

Date/Time	BLS C_n^2 ($m^{-2/3}$)	r_0 (cm):	V_L	V_T	H_L	H_T	% Difference
25 Jul 2200	4.0413e-14		2.44	2.48	2.44	2.52	2.4
25 Jul 2218	9.2957e-14		2.52	2.67	2.44	2.74	8.3
25 Jul 2232	7.3331e-14		2.49	2.53	2.39	2.68	6.2
25 Jul 2247	5.3523e-14		2.65	2.71	2.75	2.69	2.2
25 Jul 2305	6.5973e-14		2.44	2.64	2.61	2.55	4.9
25 Jul 2320	3.3617e-14		2.61	2.73	2.65	2.77	4.4
25 Jul 2348	6.1513e-14		1.92	1.94	1.86	2.00	4.0
25 Jul 0024	1.0473e-13		1.35	1.42	1.30	1.45	7.6
25 Jul 0047	1.6519e-13		1.29	1.33	1.24	1.37	6.2
25 Jul 0133	7.3675e-14		3.75	4.31	3.90	4.33	11.5
26 Jul 2049	4.3788e-13		0.75	0.69	0.80	0.64	14.0
26 Jul 2120	4.4472e-13		0.88	0.72	0.86	0.75	15.5
26 Jul 2128	1.7216e-13		1.38	1.22	1.33	1.27	8.1
26 Jul 2134	9.5701e-14		2.10	2.12	2.01	2.20	4.8

Table 2. Vertical and horizontal components of r_0 relative to the measured C_n^2 value from the BLS. For the r_0 components: V represents vertical, H is horizontal, subscripts L and T are longitudinal and transverse, respectively.

As expected, the smallest r_0 values were estimated at the same time the BLS C_n^2 measurements were largest. The majority of the r_0 estimates show approximately isotropic turbulence. However, the estimates at 0133 UTC on 25 July (about 30

minutes after sunset) show stronger turbulence along the vertical axis likely due to the layering of the atmosphere at this time. The largest anisotropy estimations by percent differences are seen in the 2049 and 2120 UTC profiles on 26 July when the r_0 values are the smallest and following sunset at 0133 UTC on 25 July from the layering.

V. Conclusion

This analysis has shown that the atmospheric turbulence profiles generated from HTS measurements of differential tilt variances agree very well with measurements from two widely accepted C_n^2 estimation tools. This method of turbulence profiling seems to produce the best results between 2200-2300 UTC when the turbulence is moderate to weak. Data sets taken during strong turbulence and within the quiescent period made profiling more difficult but still possible. However, many data sets were unusable and therefore omitted either because of subimage misalignment that was unsalvageable through autofocusing or because the tilts were great enough to move spots outside of their allotted regions. Currently, the autofocusing algorithm is not able to distinguish between two separate centroids that move into the same cell. A more advanced algorithm with the ability to track each spot when outside of its allotted cell would allow for profiling of stronger turbulence. The r_0 estimates for each set of data are mostly isotropic and therefore align with the assumptions of Kolmogorov turbulence. However, this is not the case during the period directly following sunset, where the r_0 estimates suggest anisotropy. With further development and more experiments, HTS measurements will eventually provide a deeper understanding of the workings of surface layer atmospheric turbulence.

Operating a greater number of sonic anemometers in conjunction with the HTS would give further confidence to the profiles. Ideally, additional anemometer stations would be placed between 150 to 250 m along the path where the profile is the most accurate. The chosen set of weighting functions only provided enough data for accurate estimation out to 350 m on the path when pseudo-inverted with no threshold. Therefore, the HTS profile was never accurate at the 400 m anemometer station. This needs to be considered in future experiments of the same type.

The weighting functions used in this thesis were derived using a geometric optics

approximation method and therefore neglect certain diffractive effects. The beam spread from the laser sources was not considered in the calculations and its impact on the results has not yet been explored. Currently, the location at which two sensing paths cross is approximated as a point and thus the notches in the weighting function occur at singular locations. If beam spread effects were accounted for, the sensing paths would cross as a patch rather than a point. This would ultimately affect the shape of the weighting functions and subsequently the estimate of C_n^2 . This will be considered in future work.

The horizontal path considered during this thesis gives no indication of C_n^2 as a function of altitude. In future experiments, the laser sources could be stationed at a higher altitude (e.g. on a roof) while the HTS remains ground-based. Profiling over this path would then provide empirical information on how turbulence varies with height and how that dependence changes under varying turbulence conditions. This would also provide a better understanding of the atmospheric layering following sunset.

A major obstacle in this work is the inability to process strong turbulence and misaligned subapertures. Alignment correction can be handled by a more robust autofocusing algorithm. However, the problem of profiling stronger turbulence must be addressed outside of the processing script. Future experiments extending this work could potentially introduce laser beacons of multiple wavelengths or beacons that are temporally modulated. Two or more laser sources at different wavelengths (along with camera filters to distinguish the wavelengths) would allow spots from both sources to share cells. There are two potential advantages from this: either the subapertures can be widened to allow profiling of stronger turbulence by providing a greater dynamic range for spot motion, or the subapertures are kept the same size and data sets could measure centroids of two wavelengths when calculating statistics,

therefore increasing the accuracy of the profiles. Temporal modulation of two lasers would also make it possible for the two beams to share the same subapertures. It is necessary that the modulation frequency be faster than the concurrent Greenwood frequency in order for both lasers to see constant turbulence. If this condition is met, this method would provide a greater number of measurements for profile estimation.

This thesis presents a novel method for profiling the turbulence distribution over a path using two laser beacons and a Hartmann Turbulence Sensor. This method is phase-based and can therefore be applied over greater operational distances than irradiance-based techniques. The turbulence profiles produced by this method provide a greater understanding of surface layer turbulence. The phase information gained from the profiles generated in this work can be passed to a multi-conjugate adaptive optics system as a powerful tool to reverse the negative effects on electromagnetic waves following propagation through atmospheric turbulence. Ultimately, this work will aid in enhancing the lethality of long-range laser propagation and increasing the resolution of atmosphere-distorted imagery.

Table of Contents

Master Script to process data from the Hartmann Turbulence Sensor	1
Make Mask	2
Make Mask 2	2
Load Data	2
Cover bad subapertures with mask	2
Auto-Focus	3
Skip Autofocusing	4
Make Centroids	4
Make Centroids as Mask	6
Compute Differential Tilt Variances	7
Profiling Analysis	7
Sonic Anemometer Data	9
Pulls the Cn2 data from the anemometer plots	9
Pull Cn2 data from 5-minute averaged plots	10
Optimization Technique	10

Master Script to process data from the Hartmann Turbulence Sensor

```
clear; close; clc;

% Constants
wvl= 632.8e-9; % Laser wavelength
k = 2*pi/wvl; % Wavenumber
D = 1.15e-2; % Aperture size
L = 511; % Path length
w = 11e-2; % Laser Separation
s = sqrt(2)*1.15e-2*(150/146); % Aperture separation with 45 deg
rotation

% Run SLODAR Weighting

psi=0;
z=0:0.5:L;
wf=zeros(22,length(z));
for ii=0:21
    delt=(w+(ii*s))/L;
    wf(ii+1,:)=compute_slodar_weighting(D,ii*s,delt,psi,L,z);
end

% Run Non-Crossing Weighting

psi=0;
z=0:0.5:L;
wf1=zeros(21,length(z));
for ii=1:21
    delt=(w-(ii*s))/L;
```

```
wf1(ii,:)=compute_non_crossing_weighting(D,ii*s,delt,psi,L,z);  
end
```

Make Mask

```
[mask,maskvals] = mask1();  
close;
```

Make Mask 2

```
[mask,maskvals] = mask2();  
close;
```

Load Data

```
N = 1000; % Number of frames  
  
% Data  
[pix,config] = HTSf_readdata...  
    ('E:\Alex 2019-07 HTS Test\HTS Data\25 July\Run 00007.txt');  
  
% Background  
[bgpix, bgconfig] = HTSf_readdata...  
    ('E:\Alex 2019-07 HTS Test\HTS Data\25 July\Run 00004.txt');  
  
% Crop the frames  
spix = pix(18:589, 115:686, :);  
bg=bgpix(18:589,115:686,:);  
  
bgpixoff = mean(bg,3); % Background mean  
bgpixoff = repmat(bgpixoff,[1 1 N]);  
spix=single(spix)-bgpixoff; % Subtract background from each frame  
  
spix = rot90(spix,2); % Flip image to correct after HTS imaging  
  
mspix=mean(spix,3); % Mean frame  
  
figure();  
imagesc(mask.*mspix);colormap('gray');  
hold on;  
for i = 1:13:560  
    for j=1:13:560  
        rectangle('Position',[i-0.5 j-0.5 13 13],'Edgecolor','r');  
    end  
end  
axis square;  
grid on;
```

Cover bad subapertures with mask

Used to cover aberrated or misaligned subapertures by setting the mask to 0 at their location

```

mask_new = mask;
steps = 1:13:size(mask_new)-12;

% mask_new(234:247,455:481) = 0;

% mask_new(247:260,468:494) = 0;
mask_new(247:260,455:481) = 0;
% mask_new(247:260,442:468) = 0;

%Remove first column
% for x = 12:2:34
%     mask_new(x*13:(x+1)*13,1:26) = 0;
% end

% mask_new(1:14,:) = 0; % Remove first row
% mask_new(end-13:end,:) = 0; % Remove final row

% Set values of mask to 0 after portions of mask have been removed
for i = steps
    for j = steps
        if mask_new(i,j) == 1
            maskvals(floor(i/13)+1,floor(j/13)+1) = 1;
        else maskvals(floor(i/13)+1,floor(j/13)+1) = 0;
        end
    end
end

figure();
imagesc(mask_new.*mspix);colormap('gray');
hold on;
for i = 1:13:560
    for j=1:13:560
        rectangle('Position',[i-0.5 j-0.5 13 13],'Edgecolor','r');
    end
end
axis square;
grid on;

```

Auto-Focus

```

centers_x = zeros(length(steps), length(steps));
centers_y = zeros(length(steps), length(steps));

% Finds the center of each box where the mask has a value
for i = steps
    for j = steps
        if mask_new(i,j) == 1
            centers_y(floor(i/13)+1,floor(j/13)+1) = i+6;
            centers_x(floor(i/13)+1,floor(j/13)+1) = j+6;
        end
    end
end
end

```

```

centroid_x = zeros(44,44);
centroid_y = zeros(44,44);
xx = -6.5:1:5.5;
[xx, yy] = meshgrid(xx);
row = 1;

% Find centroids by looking for maximum intensity of each subaperture
% within the mean frame
for i = steps
    col = 1;
    for j = steps
        temp = mspix(i:i+12,j:j+12); % Consider a single
subaperture
        temp_max = max(max(temp)); % Find the max intensity value
        temp = temp-0.99*temp_max;
        temp(temp < 0) = 0;
        cent_x_sum = sum(sum(temp.*xx));
        cent_y_sum = sum(sum(temp.*yy));
        pix_sum = sum(sum(temp)); % Total intensity in each box
        centroid_x(row,col) = cent_x_sum./pix_sum;
        centroid_y(row,col) = cent_y_sum./pix_sum;
        col = col+1;
    end
    row = row+1;
end

% Gets rid of values underneath the mask
centroid_x = centroid_x.*maskvals;
centroid_y = centroid_y.*maskvals;

% New subaperture centers based on calculated centroids
xpr = round(centers_x + centroid_x);
ypr = round(centers_y + centroid_y);

```

Skip Autofocusing

```

xpr = centers_x;
ypr = centers_y;

```

Make Centroids

```

clc;

count = 0;
centroid_x= zeros(sum(sum(maskvals)),N);
centroid_y= zeros(sum(sum(maskvals)),N);

% Pixel count for drawing boxes around centroids as 9x9, 11x11, or
13x13
boxwidth = 11; % 9, 11, or 13

% Centroids for each frame based on absolute centers from autofocusing
for i = 1:44

```

```

for j = 1:44

    if boxwidth == 9
        xx = -4:1:4;
    elseif boxwidth == 11
        xx = -5:1:5;
    elseif boxwidth == 13
        xx = -6:1:6;
    end

    [xx yy]=meshgrid(xx);
    xx=repmat(xx,[1 1 N]);
    yy=repmat(yy,[1 1 N]);

    if maskvals(i,j) ~= 0 % Check that mask has a value

        count = count + 1;

        if boxwidth == 9
            temp = spix(ypr(i,j)-4:ypr(i,j)+4,...
                xpr(i,j)-4:xpr(i,j)+4, :);
        elseif boxwidth == 11
            temp = spix(ypr(i,j)-5:ypr(i,j)+5,...
                xpr(i,j)-5:xpr(i,j)+5, :);
        elseif boxwidth == 13
            temp = spix(ypr(i,j)-6:ypr(i,j)+6,...
                xpr(i,j)-6:xpr(i,j)+6, :);
        end

        temp_max=max(max(temp,[],1),[],2);

        if boxwidth == 9
            temp_max=repmat(temp_max,[9 9 1]);
        elseif boxwidth == 11
            temp_max=repmat(temp_max,[11 11 1]);
        elseif boxwidth == 13
            temp_max=repmat(temp_max,[13 13 1]);
        end

        temp=temp-0.2*temp_max; % Attempt to remove noise pedestal
        temp(temp<0)=0;
        cent_x_sum=sum(sum(temp.*xx,1),2);
        cent_y_sum=sum(sum(temp.*yy,1),2);
        pix_sum=sum(sum(temp,1),2);

        centroid_x(count,:)=cent_x_sum./pix_sum;
        centroid_y(count,:)=cent_y_sum./pix_sum;

    end
end

spixnew = zeros(572,572,N);

```

```

% Create the new autofocused frames
for i = 1:44
    for j = 1:44
        if maskvals(i,j) ~= 0
            if boxwidth == 9
                spixnew((i-1)*13+3:(i-1)*13+11,...
                    (j-1)*13+3:(j-1)*13+11,:)=...
                    spix(ypr(i,j)-4:ypr(i,j)+4,
xpr(i,j)-4:xpr(i,j)+4, :);
            elseif boxwidth == 11
                spixnew((i-1)*13+2:(i-1)*13+12,...
                    (j-1)*13+2:(j-1)*13+12,:)=...
                    spix(ypr(i,j)-5:ypr(i,j)+5,
xpr(i,j)-5:xpr(i,j)+5, :);
            elseif boxwidth == 13
                spixnew((i-1)*13+1:(i-1)*13+13,...
                    (j-1)*13+1:(j-1)*13+13,:)=...
                    spix(ypr(i,j)-6:ypr(i,j)+6,
xpr(i,j)-6:xpr(i,j)+6, :);
            end
        end
    end
end

meanpix = mean(spixnew,3);

% Show the new autofocused image
figure();
imagesc(mask_new.*meanpix); colormap('gray');
hold on

% Draw grid
for i = steps
    for j = steps
        rectangle('Position',[i-0.5 j-0.5 13 13],'Edgecolor','r');
    end
end
hold off

```

Make Centroids as Mask

```

centroid_total_x=zeros(sum(sum(maskvals)),1000);
centroid_total_y=zeros(sum(sum(maskvals)),1000);

centroid_total_x(:,1:1000)=centroid_x;
centroid_total_y(:,1:1000)=centroid_y;

clear centroid_x centroid_y;

for i=1:200:1000
    for j=1:sum(sum(maskvals))
        temp_x=centroid_total_x(j,i:i+199);
    end
end

```

```

temp_y=centroid_total_y(j,i:i+199);

% Correct for drift after every 200 frames
centroid_total_x(j,i:i+199)=centroid_total_x(j,i:i+199)-...
    mean(temp_x(isnan(temp_x)==false));
centroid_total_y(j,i:i+199)=centroid_total_y(j,i:i+199)-...
    mean(temp_y(isnan(temp_y)==false));
end
end
cent_x=zeros(44,44,1000);
cent_y=zeros(44,44,1000);
count=0;
for i=1:44
    for j=1:44
        if maskvals(i,j)==true
            count=count+1;
            cent_x(i,j,:)=centroid_total_x(count,:);
            cent_y(i,j,:)=centroid_total_y(count,:);
        end
    end
end
cent_x=cent_x*(wvl/(3*D));
cent_y=cent_y*(wvl/(3*D));

```

Compute Differential Tilt Variances

```

count=1;
tilt_var=zeros(22,1);
for sep=1:2:43
    tilt_var(count)=compute_differential_variances...
        (cent_x,cent_y,sep,maskvals);
    count=count+1;
end

% Compute Non-Crossing Differential Tilt Variances

count=1;
tilt_var_noncross=zeros(21,1);
for sep=1:2:41

    tilt_var_noncross(count)=compute_differential_variances_noncross...
        (cent_x,cent_y,sep,maskvals);
    count=count+1;
end

```

Profiling Analysis

```

load('F:\HTS Script\weighting_function.mat','wf');
wf(wf<0) = 0;
load('F:\HTS Script\weighting_function_noncrossing.mat','wf1');
wf1(wf1<0) = 0;

clear wf2 tilt_var_2

```

```

wf2 = wf;
tilt_var2 = tilt_var;

% Removes the largest separation function if first column is removed
% wf2 = wf(1:end-1,:);
% tilt_var2 = tilt_var(1:end-1);

% Differencing technique to reduce noise assuming noise statistics are
% constant between measurements
wf2=diff(wf2,1,1);
tilt_var2=diff(tilt_var2);

% Add non-cross weighting functions
wf2 = [wf2;wf1(1:5,:);wf1(21,:)];
tilt_var2 = [tilt_var2;tilt_var_noncross(1:5);tilt_var_noncross(21)];

% Calculate Fried parameters
[vr0_l, vr0_t] = calculate_r0('v',cent_x,cent_y,maskvals);
[hr0_l, hr0_t] = calculate_r0('h',cent_x,cent_y,maskvals);
fprintf('      V r0 L      V r0 T      H r0 L      H r0 T \n');
disp([vr0_l, vr0_t, hr0_l, hr0_t]);
r0_mean = (vr0_l+vr0_t+hr0_l+hr0_t)/4;

% Tilt due to a point source
tilt_pt = 0.3636*wvl^2*D^(-1/3)*r0_mean^(-5/3);

% r0 Weighting function
z = 0:0.5:L;
wf_r0 = 0.3636*wvl^2*D^(-1/3)*0.423*(k^2)*((1-z/L).^(5/3));
% wf2 = [wf2;wf_r0];
% tilt_var2 = [tilt_var2;tilt_pt];

thres = 11; % Set pseudoinverse threshold
C = 2*pinv(wf2,thres)*tilt_var2; % Cn2 profile
aa = pinv(wf2,thres)*wf2; % Influence function

% Plot the weighting functions
figure();
hold on
plot(z,wf2) % Crossing and Noncrossing functions
title('HTS Weighting Functions')
xlabel('Range (m)')
ylabel('Weighting Functions')
grid on;
hold off

figure();
semilogy(z,C);
hold on;
C1=9.5701e-14*ones(1023,1); % From BLS
C2=aa*C1; % Constant turbulence representation
semilogy(z,C2);
axis tight;

```

```

grid on;

% Plot 1-minute anemometer values for comparison
plot(100, station1y(index1), 'ro')
plot(200, station2y(index2), 'ro')
plot(300, station3y(index3), 'ro')
plot(400, station4y(index4), 'ro')
% 5-minute averaged anemometer values
plot(100, station1y_5(index1_5), 'bo')
plot(200, station2y_5(index2_5), 'bo')
plot(300, station3y_5(index3_5), 'bo')
plot(400, station4y_5(index4_5), 'bo')

figure();
% Influence function, turbulence at one particular location influence
by
% turbulence at other locations, should ideally be delta function
for i=1:1023
    plot(z,aa(i,:));
    drawnow;
    axis tight;
end
grid on;
end

```

Sonic Anemometer Data

Loads anemometer plots from a processed figure of Cn2

```

% 1 minute average
fig1 = load('E:\Alex 2019-07 HTS Test\Sonic Data Summer 2019\July\Used
\Night of 25th\25July_1minAvg_Cn2.fig','-mat');
% fig1 = load('E:\Alex 2019-07 HTS Test\Sonic Data Summer 2019\July
\Used\Afternoon of 26th\26July_1minAvg_Cn2.fig','-mat');

% 5 minute average
fig5 = load('E:\Alex 2019-07 HTS Test\Sonic Data Summer 2019\July\Used
\Night of 25th\25JulyCn2_Corrected.fig','-mat');
% fig5 = load('E:\Alex 2019-07 HTS Test\Sonic Data Summer 2019\July
\Used\Afternoon of 26th\26JulyCn2_Corrected.fig','-mat');

```

Pulls the Cn2 data from the anemometer plots

```

station1x = fig1.hgS_070000.children(1).children(1).properties.XData;
station1y = fig1.hgS_070000.children(1).children(1).properties.YData;
station2x = fig1.hgS_070000.children(1).children(2).properties.XData;
station2y = fig1.hgS_070000.children(1).children(2).properties.YData;
station3x = fig1.hgS_070000.children(1).children(3).properties.XData;
station3y = fig1.hgS_070000.children(1).children(3).properties.YData;
station4x = fig1.hgS_070000.children(1).children(4).properties.XData;
station4y = fig1.hgS_070000.children(1).children(4).properties.YData;

% Convert time and date into serial
datetime = datenum(2019, 7, 26, 21, 34, 0); % Y, M, D, H, Mn, S

```

```

% Find closest value on y axis
timevect1 = repmat(datetime, [1 length(station1x)]);
timevect2 = repmat(datetime, [1 length(station2x)]);
timevect3 = repmat(datetime, [1 length(station3x)]);
timevect4 = repmat(datetime, [1 length(station4x)]);
 [~, index1] = min(abs(station1x - timevect1));
 [~, index2] = min(abs(station2x - timevect2));
 [~, index3] = min(abs(station3x - timevect3));
 [~, index4] = min(abs(station4x - timevect4));

```

Pull Cn2 data from 5-minute averaged plots

```

station1x_5 =
    fig5.hgS_070000.children(2).children(1).properties.XData;
station1y_5 =
    fig5.hgS_070000.children(2).children(1).properties.YData;
station2x_5 =
    fig5.hgS_070000.children(2).children(2).properties.XData;
station2y_5 =
    fig5.hgS_070000.children(2).children(2).properties.YData;
station3x_5 =
    fig5.hgS_070000.children(2).children(3).properties.XData;
station3y_5 =
    fig5.hgS_070000.children(2).children(3).properties.YData;
station4x_5 =
    fig5.hgS_070000.children(2).children(4).properties.XData;
station4y_5 =
    fig5.hgS_070000.children(2).children(4).properties.YData;

% Find closest value on y axis
timevect1_5 = repmat(datetime, [1 length(station1x_5)]);
timevect2_5 = repmat(datetime, [1 length(station2x_5)]);
timevect3_5 = repmat(datetime, [1 length(station3x_5)]);
timevect4_5 = repmat(datetime, [1 length(station4x_5)]);
 [~, index1_5] = min(abs(station1x_5 - timevect1_5));
 [~, index2_5] = min(abs(station2x_5 - timevect2_5));
 [~, index3_5] = min(abs(station3x_5 - timevect3_5));
 [~, index4_5] = min(abs(station4x_5 - timevect4_5));

```

Optimization Technique

Attempts to minimize an objective function to reduce measurement noise and dropouts in the Cn2 profile

```

% Initial guess passed into fmincon
C=2*pinv(wf2, thres)*tilt_var2;
C=abs(C*(1e10)); % Multiply by 1e10 to beat machine noise
C(C<=1.01e-4)=1.01e-4; % Floor % > 1b
% C(C>=2.99e-2)=2.99e-2; % Ceiling

tilt_var1=tilt_var2*(1e10);
w_r0=0.423*(k^2)*0.5*((1-z/L).^(5/3)); % Step size 0.5 = delta_z

% Lower and upper bounds

```

```

lb=ones(1023,1)*1e-4;
ub=4e-3*ones(1023,1);

fun=@(X)sum((0.5*wf2*X(:)-tilt_var1).^2); % Objective function X = Cn2
options = optimoptions(@fmincon,'MaxIterations',100000,...
    'MaxFunctionEvaluations',300000,'Display','iter',...
    'StepTolerance',1e-5 , 'ConstraintTolerance',1e-16);

% Optimize without r0 constraint
[X,fval,exitflag,output]=fmincon(fun,C,[],[],[],[],lb,ub,[],options);

% Optimize with r0 constraint
% Hard coded, initial guess must be smaller than r0 estimates
[X,fval,exitflag,output]=fmincon(fun,C,w_r0,0.01^(-5/3)*(1e10),...
    [],[],lb,ub,[],options);

C2=2*pinv(wf2, thres)*tilt_var2; % Raw profile for comparison

figure();
semilogy(z,C2);
hold on;
semilogy(z,X/1e10); % Optimized profile
semilogy(z, aa*C1); % BLS measurement profile
grid on;

% Plot anemometer values at their position
plot(100, stationonly(index1), 'ro')
plot(200, station2y(index2), 'ro')
plot(300, station3y(index3), 'ro')
plot(400, station4y(index4), 'ro')
plot(100, stationonly_5(index1_5), 'bo') % 5-min averaged
plot(200, station2y_5(index2_5), 'bo')
plot(300, station3y_5(index3_5), 'bo')
plot(400, station4y_5(index4_5), 'bo')

```

Published with MATLAB® R2017b

```
function i= compute_slodar_weighting(D,s,delt,psi,L,z)
% Generates the weighting function for the crossing sensing path
% geometry.

i=zeros(1,length(z));
for count=1:length(z)

    f1=@(beta,u)((u.*acos(u)-u.^2.*(3-2*(u.^2)).*sqrt(1-
u.^2)).*((u.*(1-z(count))/L)).^(5/3)-0.5*((u.*(1-z(count))/L)).^2+((s-
delt*z(count))/D).^2+...
    2*u.*(1-z(count))/L.*((s-delt*z(count))/D).*cos(psi
+beta)).^(5/6)-0.5*((u.*(1-z(count))/L)).^2+((s-delt*z(count))/
D).^2-...
    2*u.*(1-z(count))/L.*((s-delt*z(count))/D).*cos(psi
+beta)).^(5/6)));

i(count)=-32*8*2.91*((1/pi).^2)*(D.^(-1/3))*integral2(f1,0,2*pi,0,1);
end
end
```

Published with MATLAB® R2017b

```
function i= compute_non_crossing_weighting(D,s,delt,psi,L,z)
% Generates weighting functions for the non-crossing geometry.

i=zeros(1,length(z));
for count=1:length(z)

    f1=@(beta,u)((u.*acos(u)-u.^2.*(3-2*(u.^2)).*sqrt(1-
u.^2)).*((u.*(1-z(count))/L)).^(5/3)-0.5*((u.*(1-z(count))/L)).^2+((s
+delt*z(count))/D).^2+...
    2*u.*(1-z(count))/L.*((s+delt*z(count))/D).*cos(psi
+beta)).^(5/6)-0.5*((u.*(1-z(count))/L)).^2+((s+delt*z(count))/
D).^2-...
    2*u.*(1-z(count))/L.*((s+delt*z(count))/D).*cos(psi
+beta)).^(5/6)));

i(count)=-32*8*2.91*((1/pi).^2)*(D.^(-1/3))*integral2(f1,0,2*pi,0,1);
end
end
```

Published with MATLAB® R2017b

```

function [Data,config] = HTSf_readdata(filename)
% Reads in data from the HTS binary files and formats the data as a
% matrix that can be viewed using imagesc().

% open the txt file associated with the provided data file
fid = fopen([filename(1:end-4), '.txt']);
dtx = fscanf(fid, '%s');
fclose(fid);

% collect experiment information from data txt file
config.run = str2double(dtx(strfind(dtx,'RunNumber:')+...
    length('RunNumber:') : strfind(dtx,'RecordDate/Time:')-1));
config.timestamp = dtx(strfind(dtx,'RecordDate/Time:')+...
    length('RecordDate/Time:') : strfind(dtx,'DataFormat:')-1);
config.format = dtx(strfind(dtx,'DataFormat:')+...
    length('DataFormat:') : strfind(dtx,'Imagesize:')-1);
ImgSz = dtx(strfind(dtx,'Imagesize:')+...
    length('Imagesize:') : strfind(dtx,'CameraExposure(Microsec:')-1));
config.ImgSz = [str2double(ImgSz(strfind(ImgSz, 'x')+1:end)), ...
    str2double(ImgSz(1:strfind(ImgSz, 'x')-1))];
config.nframes.FBkgd = str2double(dtx(strfind(dtx,...
    'FastBackgroundFramesCollected:')+...
    length('FastBackgroundFramesCollected:') : ...
    strfind(dtx,'FastDataFramesCollected:')-1));
config.nframes.FData = str2double(dtx(strfind(dtx,...
    'FastDataFramesCollected:')+length('FastDataFramesCollected:') : ...
    strfind(dtx,'SlowBackgroundFramesCollected:')-1));
config.nframes.SBkgd = str2double(dtx(strfind(dtx,...
    'SlowBackgroundFramesCollected:')+...
    length('SlowBackgroundFramesCollected:') : ...
    strfind(dtx,'SlowDataFramesCollected:')-1));
config.nframes.SData = str2double(dtx(strfind(dtx,...
    'SlowDataFramesCollected:')+length('SlowDataFramesCollected:') : ...
    strfind(dtx,'PropagationDistance:')-1));
config.frate.FBkgd =
    str2double(dtx(strfind(dtx,'FastBackgroundFPS:')+...

    length('FastBackgroundFPS:') : strfind(dtx,'FastDataCollectFPS:')-1));
config.frate.FData =
    str2double(dtx(strfind(dtx,'FastDataCollectFPS:')+...

    length('FastDataCollectFPS:') : strfind(dtx,'SlowBackgroundFPS:')-1));
config.frate.SBkgd =
    str2double(dtx(strfind(dtx,'SlowBackgroundFPS:')+...

    length('SlowBackgroundFPS:') : strfind(dtx,'SlowDataCollectFPS:')-1));
config.frate.SData =
    str2double(dtx(strfind(dtx,'SlowDataCollectFPS:')+...
        length('SlowDataCollectFPS:') : ...
        strfind(dtx,'FastBackgroundFramesCollected:')-1));

```

```

config.Exp =
    str2double(dtx(strfind(dtx, 'CameraExposure(Microsec):')+...

    length('CameraExposure(Microsec):'):strfind(dtx, 'ImageBitDepth:')-1));

config.depth = str2double(dtx(strfind(dtx, 'BitDepth:')+...
    length('BitDepth:'):strfind(dtx, 'Ry:')-1));
config.yi = str2double(dtx(strfind(dtx, 'Ry:')+...
    length('Ry:'):strfind(dtx, 'Rx:')-1));
config.xi = str2double(dtx(strfind(dtx, 'Rx:')+...
    length('Rx:'):strfind(dtx, 'FastBackgroundStart:')-1));
config.timing.FBstart = dtx(strfind(dtx, 'FastBackgroundStart:')+...

    length('FastBackgroundStart:'):strfind(dtx, 'FastDataCollectStart:')-1);
config.timing.FDstart = dtx(strfind(dtx, 'FastDataCollectStart:')+...

    length('FastDataCollectStart:'):strfind(dtx, 'SlowBackgroundStart:')-1);
config.timing.SBstart = dtx(strfind(dtx, 'SlowBackgroundStart:')+...

    length('SlowBackgroundStart:'):strfind(dtx, 'SlowDataCollectStart:')-1);
config.timing.SDstart = dtx(strfind(dtx, 'SlowDataCollectStart:')+...

    length('SlowDataCollectStart:'):strfind(dtx, 'DownloadFinished:')-1);

config.propdist =
    str2double(dtx(strfind(dtx, 'PropagationDistance:')+...
        length('PropagationDistance:'):end));

dtagrp = ' Fast Data Collect.bin';

% load data collect
datafile = strrep(filename, '.txt', dtagrp);
Nfr = config.nframes.FData;
Data = zeros(config.ImgSz(1),config.ImgSz(2),Nfr);
temp = zeros(config.ImgSz(2),config.ImgSz(1));

fid = fopen(datafile);
for n = 1:Nfr

    % labview places 2 bits as a marker at the
    % front of each frame in the binary file
    fread(fid, [2 1], 'uint16', 'b');

    temp(:) = fread(fid, [config.ImgSz(2)
    config.ImgSz(1)], 'uint16', 'b');
    Data(:, :, n) = temp;
end
fclose(fid);

```

Published with MATLAB® R2017b

```
function
    var_tot=compute_differential_variances(cent_x,cent_y,d,mask_subap)
% Computes the tilt variances for the crossing weighting functions
% using the centroid motion information. Returns the calculated
% differential variance value.

var_tot=0;
count=0;
for i=1:44
    j=1;
    while j+d<=44
        if (mask_subap(i,j)==true)&&(mask_subap(i,j+d)==true)
            dx=cent_x(i,j,:)-cent_x(i,j+d,:);
            dy=cent_y(i,j,:)-cent_y(i,j+d,:);
            var_tot=var_tot+...
                var(dx(isnan(dx)==false))+var(dy(isnan(dy)==false));
            count=count+1;
            j=j+2;
        elseif (mask_subap(i,j)==true)&&(mask_subap(i,j+d)==false)
            j=j+2;
        else
            j=j+1;
        end
    end
end
var_tot=var_tot/count;
end
```

Published with MATLAB® R2017b

```
function
    var_tot=compute_differential_variances_noncross(cent_x,cent_y,d,
    mask_subap)
% Computes the tilt variances for the non-crossing weighting functions
% using the centroid motion information. Returns the calculated
% differential variance value.

var_tot=0;
count=0;
for i=1:44
    j=1;
    while j+d+1<=44
        if (mask_subap(i,j)==true)&&(mask_subap(i,j+d+1)==true)
            dx=cent_x(i,j+1,:)-cent_x(i,j+d+1,:);
            dy=cent_y(i,j+1,:)-cent_y(i,j+d+1,:);
            var_tot=var_tot+...
                var(dx(isnan(dx)==false))+var(dy(isnan(dy)==false));
            count=count+1;
            j=j+2;
        elseif (mask_subap(i,j)==true)&&(mask_subap(i,j+d+1)==false)
            j=j+2;
        else
            j=j+1;
        end
    end
end
var_tot=var_tot/count;
end
```

Published with MATLAB® R2017b

Appendix A. Anemometer Structure Function Averaging Issues

The sonic anemometers are set to average and output temperature measurements over 100 ms intervals. The structure function assumed by the anemometer when calculating C_T^2 is

$$D(r) \equiv \langle (T(r_1) - T(r_2))^2 \rangle = C_T^2 r^{2/3}, \quad (83)$$

where $T(r_1)$ and $T(r_2)$ are the temperature at two locations with separation r . Taylor's frozen flow hypothesis states the advection of a turbulence field past a fixed point can be approximated by the mean flow of the field. When the relative intensity of the turbulence is small, Taylor's hypothesis gives $r = v\Delta t$, where v is the mean wind speed and Δt is the time interval. This allows C_T^2 to be computed directly from the structure function by

$$C_T^2 = \langle (T(r_1) - T(r_2))^2 \rangle (v \cdot 100ms)^{-2/3}. \quad (84)$$

However, this methodology has been found to underestimate C_T^2 .

From Equation 83,

$$\iint D(x - y) dx dy = \left\langle \iint (T(x)^2 - 2T(x)T(y) + T(y)^2) dx dy \right\rangle, \quad (85)$$

where x and y are two separate points in time. Assuming a collection time t and a temporal separation δ gives the relation

$$\begin{aligned} & \frac{1}{t^2} \left\langle \left[\int_0^t (T(x) - T(x + \delta)) dx \right]^2 \right\rangle \\ &= \frac{1}{t^2} \left\langle \left(\int_0^t (T(x) - T(x + \delta)) dx \right) \left(\int_0^t (T(y) - T(y + \delta)) dy \right) \right\rangle \\ &= \frac{1}{t^2} \left\langle \left(\int_0^t \int_0^t (T(x)T(y) - T(x + \delta)T(y) - T(x)T(y + \delta) + T(x + \delta)T(y + \delta)) dx dy \right) \right\rangle \end{aligned} \quad (86)$$

It is then possible to manipulate this integral by adding zero in the form of

$$0 = T(x)^2 - T(x)^2 + T(y)^2 - T(y)^2 + T(x+\delta)^2 - T(x+\delta)^2 + T(y+\delta)^2 - T(y+\delta)^2 \quad (87)$$

to obtain

$$\begin{aligned} \frac{1}{2t^2} \left\langle \int_0^t \int_0^t (& -T(x)^2 + 2T(x)T(y) - T(y)^2 \right. \\ & + T(x+\delta)^2 - 2T(x+\delta)T(y) + T(y)^2 \\ & + T(x)^2 - 2T(x)T(y+\delta) + T(y+\delta)^2 \\ & \left. - T(x+\delta)^2 + 2T(x+\delta)T(y+\delta) - T(y+\delta)^2) dx dy \right\rangle \end{aligned} \quad (88)$$

or alternatively,

$$\begin{aligned} &= \frac{1}{2t^2} \int_0^t \int_0^t -D(x-y) + D(x+\delta-y) + D(x-y+\delta) - D(x+\delta-y-\delta) dx dy \\ &= \frac{1}{t^2} \int_0^t \int_0^t (D(x-y+\delta) - D(x-y)) dx dy \end{aligned} \quad (89)$$

Assuming $t = 10s$ and $\delta = 10s$, Equation 89 gives

$$\frac{1}{100} \int_0^{10} \int_0^{10} (D(x-y+10) - D(x-y)) dx dy = 9 \left(\frac{2}{5} \right)^{1/3} - \frac{9}{10^{1/3}} \approx 2.45. \quad (90)$$

In the averaging, the anemometers simply assume

$$D(r) = C_T^2 r^{2/3} = 10^{2/3} \approx 4.64 \quad (91)$$

given $C_T^2 = 1 \text{ m}^{-2/3}$ and $r = 10m$. Therefore, the anemometers are underestimating the true structure function value by a factor of 1.89. This correction is applied within the anemometer processing script.

Bibliography

1. David C Mann, Robert H Dueck, and Brian Monacelli. Hartmann Turbulence Sensor Operation. (May), 2010.
2. Santasri R. Bose-Pillai, Jack E. McCrae, Christopher A. Rice, Steven T. Fiorino, Matthew D. Wilson, and Andrew L. Back. Profiling of atmospheric turbulence along a path using two beacons and a Hartmann turbulence sensor. page 10, 2018.
3. Santasri R. Bose-Pillai, Jack E. McCrae, Christopher A. Rice, Ryan A. Wood, Connor E. Murphy, and Steven T. Fiorino. Estimation of atmospheric turbulence using differential motion of extended features in time-lapse imagery. *Optical Engineering*, 57(10):1, 2018.
4. R.K. Tyson. *Principles of Adaptive Optics*. CRC Press, 2015.
5. A. Tokovinin, J. Vernin, A. Ziad, and M. Chun. Optical Turbulence Profiles at Mauna Kea Measured by MASS and SCIDAR. *Publications of the Astronomical Society of the Pacific*, 117(830):395–400, 2005.
6. Michael Goodwin, Charles Jenkins, and Andrew Lambert. Improved detection of atmospheric turbulence with SLODAR. *Optics Express*, 15(22), 2007.
7. Retrieval of structure functions of air temperature and refractive index from large eddy simulations of the atmospheric boundary layer. *Laser Communication and Propagation through the Atmosphere and Oceans II*, 8874(September 2013):887408, 2013.
8. Christopher R. Neyman and Bruce E. Stribling. <title>Scintillation detection and ranging (SCIDAR) at the Air Force Maui Optical Station</title>. *Prop-*

- agation and Imaging through the Atmosphere III*, 3763(October 1999):259–267, 1999.
9. Remy Avila, Jean Vernin, and Elena Masciadri. Whole atmospheric-turbulence profiling with generalized scidar. 1997.
 10. Alex Mahalov and Austin Mcdaniel. Long-range propagation through inhomogeneous turbulent atmosphere : analysis beyond phase screens. 2019.
 11. E. Hecht. *Optics*. Pearson education. Addison-Wesley, 2002.
 12. Larry C. Andrews and Ronald L. Phillips. Laser beam propagation through random media. 2005.
 13. Osborne Reynolds. An experimental investigation of the circumstances which determine whether the motion of water in parallel channels shall be direct or sinuous and of the law of resistance in parallel channels. *Society, The Royal Transactions, Philosophical Society, Royal*, 174(1883):935–982, 1883.
 14. U. Frisch and A.N. Kolmogorov. *Turbulence: The Legacy of A. N. Kolmogorov*. Cambridge University Press, 1995.
 15. Michael C. Roggemann and Byron M. Welsh. Imaging through turbulence. 1996.
 16. Lydia Yatcheva, Rui Barros, Max Segel, Detlev Sprung, Erik Sucher, Christian Eisele, and Szymon Gladysz. Ultimate turbulence experiment: simultaneous measurements of C_n^2 near the ground using six devices and eight methods . *Optics in Atmospheric Propagation and Adaptive Systems XVIII*, 9641(October 2015):964105, 2015.
 17. Lewis F. Richardson. Atmospheric Diffusion Shown on a Distance-Neighbor Graph. *Royal Society of London*, pages 709–737, 1926.

18. Robert R. Beland. In Frederick G. Smith, editor, *Atmospheric Propagation of Radiation*, volume 2, chapter Propagation through Atmospheric Optical Turbulence, page 333. 1993.
19. David L. Fried. Optical Heterodyne Detection of an Atmospherically Distorted Signal Wave Front. *Proceedings of the IEEE*, 55(1):57–67, 1967.
20. Terry J. Brennan, David C. Zimmerman, and Robert H Dueck. A Hartmann Turbulence Sensor (HTS) for Estimating the Strength of Turbulence and Inner Scale along an Optical Propagation Path, 2010.
21. R.K. Tyson. *Introduction to Adaptive Optics*. SPIE tutorial texts. Society of Photo Optical, 2000.
22. A. N. Kolmogorov. The Local Structure of Turbulence in Incompressible Viscous Fluid for Very Large Reynolds Numbers. *Proceedings of the Royal Society A: Mathematical, Physical and Engineering Sciences*, 434(1890):9–13, 1991.
23. D. Sprung, E. Sucher, A. Ramkilowan, and D. J. Griffith. Investigation of optical turbulence in the atmospheric surface layer using scintillometer measurements along a slant path and comparison to ultrasonic anemometer measurements. *Remote Sensing of Clouds and the Atmosphere XIX; and Optics in Atmospheric Propagation and Adaptive Systems XVII*, 9242, 2014.
24. Robert H. Kraichnan. On Kolmogorov ’ s inertial-range theories. 62, 1974.
25. Focusing on a Turbulent Layer: Principle of the Generalized SCIDAR. *Publications of the Astronomical Society of the Pacific*, 110(743):86–91, 1998.
26. F. Roddier. V the effects of atmospheric turbulence in optical astronomy. volume 19 of *Progress in Optics*, pages 281 – 376. Elsevier, 1981.

27. R. W. Wilson. SLODAR: Measuring optical turbulence altitude with a Shack-Hartmann wavefront sensor. *Monthly Notices of the Royal Astronomical Society*, 337:103–108, 2002.
28. M. Sarazin and F. Roddier. The ESO differential image motion monitor. 227(1), Jan 1990.
29. T. Butterley, R. W. Wilson, and M. Sarazin. Determination of the profile of atmospheric optical turbulence strength from SLODAR data. *Monthly Notices of the Royal Astronomical Society*, 369(2):835–845, 2006.
30. Jacques M. Beckers. Adaptive Optics for Astronomy: Principles, Performance, and Applications. 31:13–62, Jan 1993.
31. Kim A Winick and D Marquis. Stellar Scintillation Technique for the Measurement of Tilt Anisoplanatism. 5(11), 1988.
32. Darryl P. Greenwood. Bandwidth specification for adaptive optics systems *. 67(March 1977):390–393, 1976.
33. Joseph Shamir, Devon G. Crowe, and James W. Beletic. Improved compensation of atmospheric turbulence effects by multiple adaptive mirror systems. *Applied Optics*, 32(24), 1993.
34. Dustin C. Johnston and Byron M. Welsh. Analysis of multiconjugate adaptive optics. *Journal of the Optical Society of America A*, 11(1):394, 1994.
35. M Tallon, R Foy, and J Vernin. Wide field adaptive optics using an array of laser guide stars. *SPIE Milestone Series MS*, 93, 1994.

36. Thierry Fusco, Jean-Marc Conan, Gérard Rousset, Laurent Marc Mugnier, and Vincent Michau. Optimal wave-front reconstruction strategies for multiconjugate adaptive optics. *Journal of the Optical Society of America A*, 18(10), 2001.
37. David L Fried. Differential angle of arrival: Theory, evaluation, and measurement feasibility. 2013:781–786, 1985.
38. David L Fried. Varieties of Isoplanatism. *Organic Light-Emitting Materials and Devices V*, 4464:281, 2003.
39. K. Tyson, Robert and Benjamin W. Frazier. *Field Guide to Adaptive Optics*. SPIE Press, 2004.
40. Jack E. McCrae, Santasri R. Bose-Pillai, Matthew G. Current, Kevin P. Lee, and Steven T. Fiorino. Measurements of anisotropy in optical turbulence. *IEEE Aerospace Conference Proceedings*, 2017.
41. Technical Description of a Sonic Anemometer/Thermometer(SATI Series).
42. Applied Technologies. Operator’s Manual for a Three Axis Sonic Anemometer/Thermometer.
43. D. S. Rohmistrov, A. Ya Bogushevich, and I. A. Botygin. Methods and algorithms for statistical processing of instantaneous meteorological parameters from ultrasonic measurements. *IOP Conference Series: Earth and Environmental Science*, 48, 2016.
44. Scintec. BLS900 Hardware Manual, 2009.
45. BLS900 Large Aperture Scintillometer - Dual-Disk Design, 2017.
46. Jack E. McCrae, Santasri Bose-Pillai, Matt Current, Kevin Lee, and Steven Fiorino. Analysis of Turbulence Anisotropy with a Hartmann Sensor. 2017.

REPORT DOCUMENTATION PAGE					<i>Form Approved</i> OMB No. 0704-0188	
The public reporting burden for this collection of information is estimated to average 1 hour per response, including the time for reviewing instructions, searching existing data sources, gathering and maintaining the data needed, and completing and reviewing the collection of information. Send comments regarding this burden estimate or any other aspect of this collection of information, including suggestions for reducing this burden to Department of Defense, Washington Headquarters Services, Directorate for Information Operations and Reports (0704-0188), 1215 Jefferson Davis Highway, Suite 1204, Arlington, VA 22202-4302. Respondents should be aware that notwithstanding any other provision of law, no person shall be subject to any penalty for failing to comply with a collection of information if it does not display a currently valid OMB control number. PLEASE DO NOT RETURN YOUR FORM TO THE ABOVE ADDRESS.						
1. REPORT DATE (DD-MM-YYYY)		2. REPORT TYPE		3. DATES COVERED (From — To)		
26-03-2020		Master's Thesis		Sept 2018 — Mar 2020		
4. TITLE AND SUBTITLE				5a. CONTRACT NUMBER		
Validation of HTS Optical Turbulence Profiling via Sonic Anemometry				5b. GRANT NUMBER		
				5c. PROGRAM ELEMENT NUMBER		
6. AUTHOR(S)				5d. PROJECT NUMBER		
Boeckenstedt, Alexander S., 2d Lt				5e. TASK NUMBER		
				5f. WORK UNIT NUMBER		
7. PERFORMING ORGANIZATION NAME(S) AND ADDRESS(ES)				8. PERFORMING ORGANIZATION REPORT NUMBER		
Air Force Institute of Technology Graduate School of Engineering and Management (AFIT/EN) 2950 Hobson Way WPAFB OH 45433-7765				AFIT-ENP-MS-20-M-082		
9. SPONSORING / MONITORING AGENCY NAME(S) AND ADDRESS(ES)				10. SPONSOR/MONITOR'S ACRONYM(S)		
Dr. Lawrence Grimes DE-JTO Director 801 University Blvd. SE, Suite 209 Albuquerque, NM 87106				DE-JTO		
				11. SPONSOR/MONITOR'S REPORT NUMBER(S)		
12. DISTRIBUTION / AVAILABILITY STATEMENT						
Approved for Public Release; Distribution unlimited.						
13. SUPPLEMENTARY NOTES						
This work is declared a work of the U.S. Government and is not subject to copyright protection in the United States.						
14. ABSTRACT						
<p>Previous turbulence measurements along a near-ground, 500 m, horizontal path using two helium-neon laser beacons and a Hartmann Turbulence Sensor (HTS) yielded profiles of C_n^2 by measuring local aberrated wavefront tilts. The HTS C_n^2 estimates were consistent with integrated turbulence values collected along the same path by a BLS900 scintillometer. Further validation of the HTS profiling method is necessary to produce accurate optical turbulence profiles for wavefront correction and to eventually gain an improved understanding of turbulence in the lower atmosphere and its variation as a function of altitude. In order to add confidence to the HTS dual-beacon profiling method, a collection of sonic anemometers was added along the path to collect point measurements of C_T^2, which were used to derive values of C_n^2. Propagation over a non-homogeneous path (i.e. part grass and part concrete) ensured the turbulence profile along the path is more varied. C_n^2 profiles in this work derived from HTS data captured on 25 and 26 July 2019 agreed strongly with the collocated anemometer and BLS measurements.</p>						
15. SUBJECT TERMS						
Optical Turbulence, Hartmann Turbulence Sensor, Adaptive Optics, Wavefront Sensing						
16. SECURITY CLASSIFICATION OF:			17. LIMITATION OF ABSTRACT		18. NUMBER OF PAGES	
a. REPORT	b. ABSTRACT	c. THIS PAGE	UU		102	
U	U	U			19a. NAME OF RESPONSIBLE PERSON Dr. Jack E. McCrae, AFIT/ENP	
			19b. TELEPHONE NUMBER (include area code) (312)785-8989 x4739 jack.mccrae@afit.edu			